

## A Multi-wavelength, Multi-epoch Monitoring Campaign of Accretion Variability in T Tauri Stars from the ODYSSEUS Survey. III. Optical Spectra

JOHN WENDEBORN,<sup>1</sup> CATHERINE C. ESPAILLAT,<sup>1</sup> THANAWUTH THANATHIBODEE,<sup>1</sup> CONNOR E. ROBINSON,<sup>2</sup> CALEY V. PITTMAN,<sup>1</sup> NURIA CALVET,<sup>3</sup> JAMES MUZEROLLE,<sup>4</sup> FREDRICK M. WALTER,<sup>5</sup> JOCHEN EISLÖFFEL,<sup>6</sup> ELEONORA FIORELLINO,<sup>7</sup> CARLO F. MANARA,<sup>8</sup> ÁGNES KÓSPÁL,<sup>9,10,11</sup> PÉTER ÁBRAHÁM,<sup>9,12,13</sup> RIK CLAES,<sup>14</sup> ELISABETTA RIGLIACO,<sup>15</sup> LAURA VENUTI,<sup>16</sup> JUSTYN CAMPBELL-WHITE,<sup>17</sup> PAULINE MCGINNIS,<sup>18,19</sup> MANUELE GANGI,<sup>18,19</sup> KARINA MAUCO,<sup>14</sup> FILIPE GAMEIRO,<sup>20,21</sup> ANTONIO FRASCA,<sup>22</sup> AND ZHEN GUO<sup>23</sup>

<sup>1</sup>*Institute for Astrophysical Research, Department of Astronomy, Boston University, 725 Commonwealth Avenue, Boston, MA 02215, USA*

<sup>2</sup>*Department of Physics & Astronomy, Amherst College, C025 Science Center 25 East Drive, Amherst, MA 01002, USA*

<sup>3</sup>*Department of Astronomy, University of Michigan, 1085 South University Avenue, Ann Arbor, MI 48109, USA*

<sup>4</sup>*Space Telescope Science Institute, 3700 San Martin Drive, Baltimore, MD 21218, USA*

<sup>5</sup>*Department of Physics and Astronomy, Stony Brook University, Stony Brook NY 11794-3800, USA*

<sup>6</sup>*Thüringer Landessternwarte, Sternwarte 5, D-07778 Tautenburg, Germany*

<sup>7</sup>*INAF – Osservatorio Astronomico di Capodimonte, via Moiariello 16, 80131 Napoli, Italy*

<sup>8</sup>*European Southern Observatory, Karl-Schwarzschild-Strasse 2, 85748 Garching bei München, Germany*

<sup>9</sup>*Konkoly Observatory, HUN-REN Research Centre for Astronomy and Earth Sciences, CSFK, MTA Centre of Excellence, Konkoly-Thege Miklós út 15-17*

<sup>10</sup>*Institute of Physics and Astronomy, ELTE Eötvös Loránd University, Pázmány Péter sétány 1/A, 1117 Budapest, Hungary*

<sup>11</sup>*Max Planck Institute for Astronomy, Königstuhl 17, 69117 Heidelberg, Germany*

<sup>12</sup>*ELTE Eötvös Loránd University, Institute of Physics, Pázmány Péter sétány 1/A, 1117 Budapest, Hungary*

<sup>13</sup>*University of Vienna, Dept. of Astrophysics, Türkenschanzstr. 17, 1180, Vienna, Austria*

<sup>14</sup>*European Southern Observatory, Karl-Schwarzschild-Strasse 2, 85748 Garching bei München, Germany*

<sup>15</sup>*INAF/Osservatorio Astronomico di Padova, Vicolo dell'osservatorio 5, 35122 Padova, Italy*

<sup>16</sup>*SETI Institute, 339 Bernardo Avenue, Suite 200, Mountain View, CA94043, USA*

<sup>17</sup>*SUPA, School of Science and Engineering, University of Dundee, Nethergate, Dundee dd1 4hn, UK*

<sup>18</sup>*ASI, Italian Space Agency, Via del Politecnico snc, 00133 Rome, Italy*

<sup>19</sup>*INAF–Osservatorio Astronomico di Roma, Via Frascati 33, 00078 Monte Porzio Catone, Italy*

<sup>20</sup>*Instituto de Astrofísica e Ciências do Espaço, Universidade do Porto, CAUP, Rua das Estrelas, PT4150-762 Porto, Portugal*

<sup>21</sup>*Departamento de Física e Astronomia, Faculdade de Ciências, Universidade do Porto, Rua do Campo Alegre 687, PT4169-007 Porto, Portugal*

<sup>22</sup>*INAF – Osservatorio Astrofisico di Catania, via S. Sofia 78, 95123 Catania, Italy*

<sup>23</sup>*Instituto de Física y Astronomía, Universidad de Valparaíso, ave. Gran Bretaña, 1111, Casilla 5030, Valparaíso, Chile*

### ABSTRACT

Classical T Tauri Stars (CTTSs) are highly variable stars that possess gas- and dust-rich disks from which planets form. Much of their variability is driven by mass accretion from the surrounding disk, a process that is still not entirely understood. A multi-epoch optical spectral monitoring campaign of four CTTSs (TW Hya, RU Lup, BP Tau, and GM Aur) was conducted along with contemporaneous *HST* UV spectra and ground-based photometry in an effort to determine accretion characteristics and gauge variability in this sample. Using an accretion flow model, we find that the magnetospheric truncation radius varies between 2.5–5  $R_{\star}$  across all of our observations. There is also significant variability in all emission lines studied, particularly  $H\alpha$ ,  $H\beta$ , and  $H\gamma$ . Using previously established relationships between line luminosity and accretion, we find that, on average, most lines reproduce accretion rates consistent with accretion shock modeling of *HST* spectra to within 0.5 dex. Looking at individual contemporaneous observations, however, these relationships are less accurate, suggesting

<sup>1</sup> Based on observations collected at the European Southern Observatory under ESO programme 106.20Z8.

that variability trends differ from the trends of the population and that these empirical relationships should be used with caution in studies of variability.

## 1. INTRODUCTION

Mass accretion in young, pre-main sequence stars known as Classical T Tauri Stars (CTTSs) sets the stage for future evolution of the system (see Williams & Cieza 2011; Hartmann et al. 2016; Fischer et al. 2023; Manara et al. 2023; Miotello et al. 2023). Yet, despite its importance, a comprehensive understanding of this process remains elusive. In particular, measuring the mass accretion rate ( $\dot{M}$ ) is complicated by many factors, not least of which is the observational tracer used.

One such observational tracer is the UV-optical continuum emission that is in excess of the underlying photospheric+chromospheric emission. This excess, produced by the energetic shocks of infalling, accreting material (Hartmann et al. 2016), is one of the most direct tracers of accretion and can be modeled to get estimates of the overall accretion rates. These models vary from a simple hydrogen slab model, assuming the excess emission originates from a hot slab of hydrogen on the stellar surface (e.g. Manara et al. 2013; Alcalá et al. 2017; Manara et al. 2021), to a multi-column shock model, assuming the accretion originates from flows of varying densities (e.g. Calvet & Gullbring 1998; Muzerolle et al. 1998a; Robinson & Espaillat 2019). In Wendeborn et al. (2024a, hereafter Paper I), we model multi-epoch *HST* observations of four CTTSs (TW Hya, RU Lup, BP Tau, and GM Aur) from the ULLYSES (UV Legacy Library of Young Stars as Essential Standards, Roman-Duval et al. 2020) survey using a multi-column shock model and find significant variability (factor of  $\sim 2$ – $5$  within several days) in each target, with slightly elevated accretion rates as compared to previous studies, also shown by Pittman et al. (2022). We find that generally the connection between accretion rates and UV line luminosities is not significant.

Photometry provides an opportunity to probe accretion with higher cadence than spectroscopy can typically provide. Excess *u*-band luminosity has long been associated with accretion in CTTSs (Gullbring et al. 1998; Robinson & Espaillat 2019). In Wendeborn et al. (2024b, hereafter Paper II), we find strong global relationships between accretion luminosity and excess *uBgVriz* luminosity, though these connections break down for some bands/targets. Additionally, light curve characteristics (time lags, periodicities) can be used to infer characteristics about the accretion such as the shape/distribution of the hotspot (Espaillat et al. 2021; Herbert et al. 2023; Wendeborn et al. 2024b), hotspot latitude (Siwak et al. 2014, 2018), and struc-

tural changes in the flow (Blinova et al. 2016; Venuti et al. 2017; Sicilia-Aguilar et al. 2020; Zsidi et al. 2022).

Emission lines in optical and NIR spectra provide another opportunity to estimate accretion rates by more directly probing the accretion flows themselves. Empirical relationships between line strength and accretion have been established using large samples of CTTS and (often) simultaneous estimates of accretion rates and line luminosities (Muzerolle et al. 1998b; Natta et al. 2004; Herczeg & Hillenbrand 2008; Ingleby et al. 2013; Alcalá et al. 2014, 2017). While the connections between  $L_{\text{acc}}$  and  $L_{\text{Line}}$  are strong, their use in estimating individual CTTS accretion rates introduces significant uncertainty and scatter (e.g., Fiorellino et al. 2021; Bouvier et al. 2023; Herczeg et al. 2023; Nelissen et al. 2023). Alternatively, Muzerolle et al. (2001); Espaillat et al. (2008); Alencar et al. (2012); Thanathibodee et al. (2019, 2023) use magnetospheric accretion flow models to model the emission profiles of the hydrogen Balmer series.

Here we employ both accretion flow modeling and empirical  $L_{\text{acc}}$ - $L_{\text{Line}}$  relationships to estimate and better understand the accretion in a monitoring campaign of four CTTSs: TW Hya, RU Lup, BP Tau, and GM Aur by the ULLYSES and PENELLOPE (Manara et al. 2021) surveys, using contemporaneous data from the ODYSSEUS (Outflows and Disks Around Young Stars: Synergies for the Exploration of ULLYSES Spectra, Espaillat et al. 2022) collaboration. See Paper I (Table 1, Section 2) for details on these targets. Here we present our optical observations and data in Section 2. In Section 3, we describe the accretion flow model and the results of modeling the monitoring data. Next, in Section 4, we discuss these results in more detail and connect them to the results of our shock modeling (Paper I) and photometry (Paper II). We present our final conclusions and summarize in Section 5.

## 2. OBSERVATIONS AND DATA REDUCTION

Multi-wavelength, multi-epoch observations of the CTTSs TW Hya, RU Lup, BP Tau, and GM Aur were carried out in 2021 (Epoch 1/E1) and 2022 (Epoch 2/E2). More background information on the individual objects can be found in Paper I. Here, we present the results of our optical spectral monitoring. Contemporaneous *HST* UV spectra are presented in Paper I while contemporaneous UV-NIR photometry is presented in Paper II.

The contemporaneous optical spectra presented here were obtained on a variety of instruments, including SMARTS/CHIRON, VLT/ESPRESSO, VLT/XSHOOTER, VLT/UVES, Haute-Provence/SOPHIE, and Tautenburg/TCES. Details of these observations can be found below and in Table 1. All spectra have been corrected for radial velocity: TW Hya,  $12.3 \text{ km s}^{-1}$  (Soubiran et al. 2018); RU Lup,  $3.3 \text{ km s}^{-1}$  (Frasca et al. 2017); BP Tau,  $16.6 \text{ km s}^{-1}$  (Jönsson et al. 2020); GM Aur  $15.2 \text{ km s}^{-1}$  (Nguyen et al. 2012). All spectra have also been dereddened using the extinction values listed in Table 1 of Paper I and the reddening law of Whittet et al. (2004) assuming  $R_V=3.1$  and constant extinction  $A_V$ .

In Paper II we show that variable extinction does not contribute significantly to the variability of our targets. To test if the variability was due to local dust, we compared the observed color slopes (for  $u-g$ ,  $B-g$ ,  $g-V$ ,  $g-r$ ,  $g-i$ , and  $g-z$  versus  $g$ ) to that predicted by a local population of dust grains. We consider a range of grain sizes, from  $0.1\text{--}10 \mu\text{m}$ , including both silicate and graphite grains. We found that no population of dust grains can reproduce the photometric color slopes we see in any object. Further, variable extinction is typically associated with dipper-like events from disk warps/inhomogeneities, which our light curves do not exhibit. The light curves used for these analyses cover a wider time span than our optical spectra, showing that variable extinction should not be significant during our optical monitoring.

### 2.1. CHIRON

High-resolution ( $R\sim 80,000$ ) optical spectra of all 4 targets were obtained with the CHIRON (Tokovinin et al. 2013) spectrograph on the Small and Medium Aperture Research Telescope System (SMARTS) 1.5m telescope. These spectra cover wavelengths of about  $4100\text{--}8800 \text{ \AA}$  and have been reduced using a custom reduction pipeline with improved treatment of background emission and bright emission lines<sup>1</sup>.

They were obtained contemporaneously with *HST* spectra (see Paper I) and photometry (see Paper II) in both E1 and E2, though the number of observations and cadence vary by target/epoch. TW Hya and RU Lup were monitored with roughly nightly cadence in both E1 and E2. BP Tau was observed twice in E1, and both BP Tau and GM Aur were monitored with roughly

nightly cadence in E2. More details on the timing of these observations can be found in Table 1.

### 2.2. ESPRESSO, X-SHOOTER, and UVES

Several other optical spectra were obtained using the Echelle Spectrograph for Rocky Exoplanets and Stable Spectrographic Observations (ESPRESSO, Pepe et al. 2021), X-Shooter (Vernet et al. 2011), and UV-visual Echelle Spectrograph (UVES, Dekker et al. 2000) instruments on the Very Large Telescope (VLT) alongside the *HST* observations for all 4 targets in one or both epochs. Based on observations collected at the European Southern Observatory under ESO programmes 106.20Z8.001, 106.20Z8.002, 106.20Z8.003, 106.20Z8.004, 106.20Z8.005, 106.20Z8.006, 106.20Z8.007, 106.20Z8.011 as part of the PENELLOPE Large VLT Program (Manara et al. 2021). Details of these observations can be found in Table 1.

Our ESPRESSO spectra cover  $3800\text{--}7900 \text{ \AA}$  at high resolution ( $R\sim 140,000$ ). X-Shooter spectra are obtained using 3 arms (UV, visible, NIR) covering  $2989\text{--}5560$ ,  $5337\text{--}10200$ , and  $9940\text{--}24790 \text{ \AA}$ , respectively. Spectral resolution varies by arm: 5,400, 18,400, and 11,600 for the UV, visible and NIR arms. UVES spectra are obtained using two arms (UV, Visible) covering  $3282\text{--}4563$  and  $4726\text{--}6835 \text{ \AA}$  with spectral resolutions of 71,000 and 87,400, respectively. Details regarding the reduction of these spectra can be found in Manara et al. (2021) and the data can be downloaded from the PENELLOPE Zenodo website<sup>2</sup> and the ESO Archive.

### 2.3. SOPHIE

We also utilize observations from Observatoire de Haute-Provence using the Spectrographe pour l’Observation des Phénomènes des Intérieurs stellaires et des Exoplanètes (SOPHIE) for GM Aur. GM Aur was observed with SOPHIE 15 times roughly nightly between  $\text{MJD}=59499\sim 59517$ . These spectra cover  $3870\text{--}6940 \text{ \AA}$  at a resolution of about 40,000. See Bouvier et al. (2023) (who first published these spectra) for details of the data reduction and processing.

### 2.4. TCES

GM Aur was monitored with the Tautenburg Coudé Echelle Spectrograph (TCES) on the 2-m Alfred Jensch telescope at Thüringer Landessternwarte Tautenburg. All 17 observations were obtained with a  $2''$  wide slit, providing a spectral resolution of  $R\sim 67,000$  from about  $4660\text{--}7350 \text{ \AA}$ . The data reduction was done

<sup>1</sup> [https://www.astro.sunysb.edu/fwalter/SMARTS/CHIRON/ch\\_reduce.pdf](https://www.astro.sunysb.edu/fwalter/SMARTS/CHIRON/ch_reduce.pdf)

<sup>2</sup> <https://zenodo.org/communities/odysseus/>

**Table 1.** Optical Spectral Observations

Object	Epoch	Instrument	MJD	Date	# of Observations	Int. Time <sup>†</sup> [s]
			[Begin/End]	[Begin/End]		
TW Hya	1	CHIRON <sup>a</sup>	59241.3/59314.2	2021-01-27/2021-04-10	26	600
		ESPRESSO <sup>b</sup>	59280.3/59313.2	2021-03-07/2021-04-09	4	720
		XSHOOTER <sup>c</sup>	59307.0/59310.2	2021-04-03/2021-04-06	2	140, 50, 40*
TW Hya	2	CHIRON <sup>a</sup>	59653.1/59698.1	2022-03-15/2022-04-29	42	600
		UVES <sup>d</sup>	59667.0/59669.0	2022-03-29/2022-03-31	2	340, 340*
RU Lup	1	CHIRON <sup>a</sup>	59264.4/59453.0	2021-02-19/2021-08-27	20	1800
		ESPRESSO <sup>b</sup>	59449.0/59458.1	2021-08-23/2021-09-01	2	600
		XSHOOTER <sup>c</sup>	59436.1/59448.1	2021-08-10/2021-08-22	2	140, 50, 30*
RU Lup	2	CHIRON <sup>a</sup>	59676.2/59817.0	2022-04-07/2022-08-26	27	1800
		ESPRESSO <sup>b</sup>	59801.0/59814.0	2022-08-10/2022-08-23	5	600
BP Tau	1	CHIRON <sup>a</sup>	59467.4/59470.4	2021-09-10/2021-09-13	2	1200
		ESPRESSO <sup>b</sup>	59459.4-59464.4	2021-09-02/2021-09-07	2	1000
		XSHOOTER <sup>c</sup>	59448.4-59460.4	2021-08-22/2021-09-03	3	150, 100, 50*
BP Tau	2	CHIRON <sup>a</sup>	59845.4-59953.1	2022-09-23/2023-01-09	42	1200
		ESPRESSO <sup>b</sup>	59928.1-59936.1	2022-12-15/2022-12-23	5	1000
		XSHOOTER <sup>c</sup>	59928.1-59931.2	2022-12-15/2022-12-18	2	150, 100, 50*
GM Aur	1	ESPRESSO <sup>b</sup>	59509.2-59556.2	2021-10-22/2021-12-08	5	1200
		XSHOOTER <sup>c</sup>	59504.3-59556.2	2021-10-17/2021-12-08	2	390, 300, 100*
		SOPHIE <sup>e</sup>	59499.0-59516.0	2021-10-12/2021-10-29	15	3600
		TCES <sup>f</sup>	59503.0-59559.9	2021-10-16/2021-12-11	17	3600
GM Aur	2	CHIRON <sup>a</sup>	59910.2-59931.1	2022-11-27/2022-12-18	18	1200
		ESPRESSO <sup>b</sup>	59910.2-59916.1	2022-11-27/2022-12-03	2	1200

<sup>a</sup>CHIRON: Spectral coverage = 4100 – 8000 Å, R~ 80,000

<sup>b</sup>ESPRESSO: Spectral coverage = 3800 – 7900 Å, R~ 140,000

<sup>c</sup>XSHOOTER: Spectral coverage = 3000 – 24800 Å, R~ 5,400 – 11,600

<sup>d</sup>UVES: Spectral coverage = 3800 – 6800 Å, R~ 71,000 – 87,400

<sup>e</sup>SOPHIE: Spectral coverage = 3900 – 6900 Å, R~ 40,000

<sup>f</sup>TCES: Spectral coverage = 4660 – 7350 Å, R~ 67,000

<sup>†</sup>Exact integration times may vary within and between epochs

\*Integration times differ between spectral arms

using the Tautenburg Spectroscopy Pipeline –  $\tau$ -spline (Sabotta et al. 2019). This includes the usual steps of bias-subtraction, flat-fielding, removal of cosmic rays, scattered light subtraction, extraction, wavelength calibration, and normalization. The pipeline uses standard

IRAF<sup>3</sup> and PYRAF<sup>4</sup> routines and the Cosmic Ray code by Malte Tewes<sup>5</sup> based on the method by van Dokkum (2001).

<sup>3</sup> IRAF is distributed by the National Optical Astronomy Observatories, which are operated by the Association of Universities for Research in Astronomy, Inc., under cooperative agreement with the National Science Foundation.

<sup>4</sup> PYRAF is a product of the Space Telescope Science Institute, which is operated by AURA for NASA

<sup>5</sup> <https://github.com/grzeimann/Panacea/blob/master/cosmics.py>



### 2.5. Flux Calibration

In order to properly compare line fluxes at different epochs and to utilize empirical relationships such as those from Alcalá et al. (2017), we need flux-calibrated spectra. To this end, we flux calibrate our spectra by using contemporaneous photometry (see Paper II). For each observation, we find all photometry contemporaneous within 6 hours. Then, for each filter (X) we calculate an average photometric flux ( $F_{Phot,X}$ ) where photometry obtained closer in time to the spectrum is weighted more, as  $\frac{1}{\Delta t + 0.1}$ , where  $\Delta t$  is the time difference (in days) between the spectrum and photometry point. Then for each  $F_{Phot,X}$ , we calculate a scaling factor  $s_X = F_{Phot,X}/F_{Spec,X}$  and scale the entire spectrum by the average  $s_X$  for all filters with at least one contemporaneous photometry point. In total, we are able to flux-calibrate 236 of 269 spectra. This includes the XSHOOTER spectra which have already been flux-calibrated, though perform additional calibration for consistency. It is important to note that the final line fluxes are sensitive to the assumed extinction,  $A_V$ , which here is assumed to be constant throughout all observations for each target.

## 3. ANALYSIS AND RESULTS

In the following sections we analyze and model the optical spectra presented in Section 2. We first present fluxes for several optical emission lines, focusing on the Balmer lines,  $H\alpha$ ,  $H\beta$ ,  $H\gamma$ , and  $H\delta$ , plus seven other He lines. We also briefly discuss our measurements of optical veiling. Finally, we present the accretion flow model and its fit to the  $H\alpha$ ,  $H\beta$ , and  $H\gamma$  lines.

### 3.1. Optical Lines

We focus here on 11 emission lines (see details in Table 2), all of which have previously been correlated with accretion (Alcalá et al. 2017). To extract the line, we estimate the continuum as a 3rd degree polynomial fit to a region of  $\pm 200$  Å, ignoring the central line region of width described in Table 2. We calculate the line flux as the total integrated flux under the continuum-subtracted spectrum. Due to some uncertainty in both the flux calibration and determination of the continuum, we add an additional 10% uncertainty in quadrature to the fluxes for all lines except  $H\alpha$  and  $H\beta$ , where their continuum is more well-defined. Calculated fluxes are listed in Appendix A (Tables 9–12), while fluxes versus time for the Balmer lines ( $H\alpha$ ,  $H\beta$ ,  $H\gamma$ , and  $H\delta$ ) are shown in Figure 2. Profiles for the three brightest Balmer lines,  $H\alpha$ ,  $H\beta$ , and  $H\gamma$  are shown in Figure 1, with observations from E1 in red and E2 in blue.

**Table 2.** Optical emission lines

Line	$\lambda_0$ [Å]	Width [Å/ km s <sup>-1</sup> ]
$H\alpha$	6562.79	30 / 1370.41
$H\beta$	4861.29	15 / 925.03
$H\gamma$	4340.47	10 / 690.69
$H\delta$	4101.7	8 / 584.71
He 14387	4387.9	3 / 204.97
He 14471	4471.5	3 / 201.13
He 14713	4713.1	1.5 / 95.41
He 15015	5015.7	5 / 298.85
He 15875	5875.6	3.5 / 178.58
He 16678	6678.2	3 / 134.67
He 17065	7065.2	3 / 127.30

Fluxes versus time for the remaining lines are shown in Figures 9–10 in Appendix B.

#### 3.1.1. Balmer Lines

Here we focus on  $H\alpha$ ,  $H\beta$ ,  $H\gamma$ , and  $H\delta$  (though we do not discuss  $H\delta$ ). These are the brightest lines in our study and are known to closely trace the accretion flows (Muzerolle et al. 2001; Bouvier et al. 2023). In some cases they also trace outflows/winds, which manifest as absorption features and can complicate the line shape (Dupree et al. 2014; Bouvier et al. 2023). Variability in the emission strength is indicative of changes in the accretion flow geometry and/or rate, while changes in the absorption features are largely indicative of changes in the wind and are often stochastic.

TW Hya’s emission lines are characterized by bright, asymmetric profiles (Figure 1, top row). The asymmetry is primarily due to strong, blue-shifted absorption from  $-100$  to  $-50$  km s<sup>-1</sup>. This absorption reaches below the continuum in  $H\beta$  and  $H\gamma$  and is strongest in E2. There is also a narrow, low-velocity red-shifted emission component present in some observations in E2. Peak-to-peak,  $H\alpha$ ,  $H\beta$ , and  $H\gamma$  fluxes vary by factors of 2.5, 4.1, and 3.4, respectively.

As seen in our shock modeling and photometry from Papers I and II, RU Lup’s emission lines (Figure 1, second row) are brightest in E1 and reach their lowest point during our *HST* monitoring in E2.  $H\alpha$  and  $H\beta$  are largely symmetric in both epochs, though some blue-shifted absorption appears stronger in E2.  $H\gamma$  is largely asymmetric, with stronger emission on its red side. Additionally, the red and blue wings in  $H\gamma$  are different from one another and from the other targets: the blue wing appears slightly shallower than the other targets

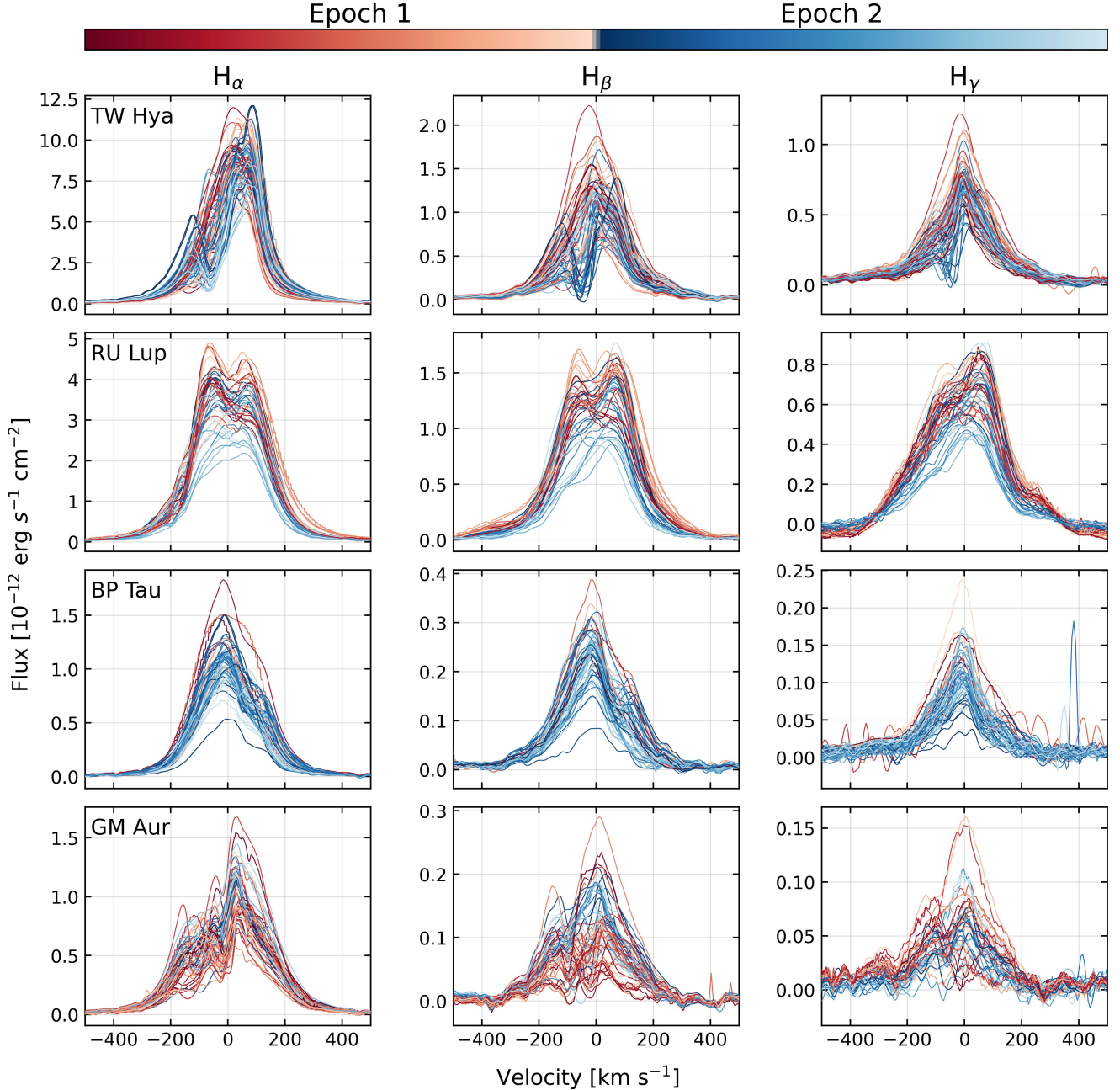


**Figure 1.** Continuum-subtracted line profiles for  $H\alpha$ ,  $H\beta$ , and  $H\gamma$  (left to right) for TW Hya, RU Lup, BP Tau, and GM Aur (top to bottom). Red lines are spectra from E1, while blue lines are spectra from E2. Darker lines denote spectra obtained earlier in their respective epoch. Spectra have been smoothed using a Savitzky-Golay filter for clarity.

while the red wing drops steeply below  $\sim 200 \text{ km s}^{-1}$ , but slowly afterwards. Peak-to-peak,  $H\alpha$ ,  $H\beta$ , and  $H\gamma$  fluxes vary by factors of 2.4, 3.1, and 2.8, respectively.

BP Tau (Figure 1, third row) exhibits the most consistent line shapes in our sample, varying primarily in intensity. All three lines show red-shifted absorption with symmetric red/blue wings and little to no obvious blue-shifted absorption. The red absorption appears to be fairly broad and/or weak, as BP Tau does not

show strong, sharp absorption features like TW Hya and GM Aur. Peak-to-peak,  $H\alpha$ ,  $H\beta$ , and  $H\gamma$  fluxes vary by factors of 3.8, 5.1, and 6.7, respectively.

The Balmer lines in GM Aur (Figure 1, last row) show the strongest variability and most complex morphology. The shape of  $H\alpha$  is dominated by strong, variable blue-shifted absorption from  $-200$  to  $-50 \text{ km s}^{-1}$  in both E1 and E2.  $H\beta$  and  $H\gamma$  also show very strong absorption in both epochs, but it is much more pronounced in E1.

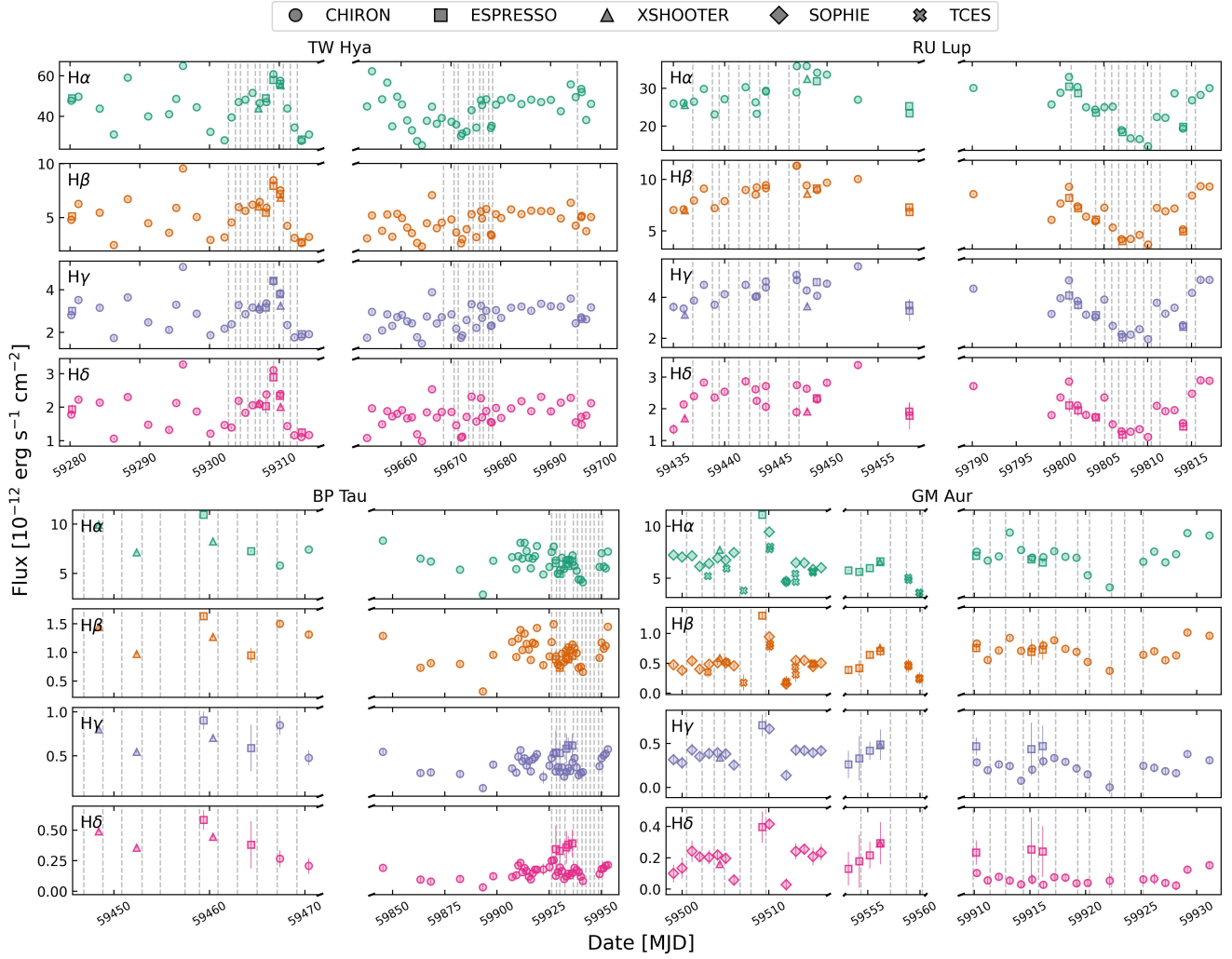


**Figure 2.** Flux versus time for  $H\alpha$ ,  $H\beta$ ,  $H\gamma$ , and  $H\delta$  (top to bottom) for TW Hya (top left), RU Lup (top right), BP Tau (bottom left) and GM Aur (bottom right). Marker shape denotes the instrument used, with CHIRON, ESPRESSO, XSHOOTER, SOPHIE, and TCES as circles, squares, triangles, diamonds, and crosses, respectively. Line flux is in units of  $10^{-12}$  erg/s/cm<sup>2</sup>. Dashed grey lines are times of the *HST* observations from Paper I. Note that some observations that are far removed in time are not included here. Note the broken axis for GM Aur, E1.

While the red wing in  $H\gamma$  is never unambiguously in absorption, it does appear to be more depressed than the other lines/targets, suggestive of matter inflow. Peak-to-peak,  $H\alpha$ ,  $H\beta$ , and  $H\gamma$  fluxes vary by factors of 3.1, 8.5, 201.4, respectively. The dramatic variability in  $H\gamma$  is due to a particularly low observation where  $H\gamma$  is largely washed out by noise. Ignoring this observation, the peak-to-peak variability in  $H\gamma$  is 9.0.

While we cannot rule out the possibility that extinction plays some role in the different variability amplitudes of the Balmer lines, it is unlikely to be the primary cause. It is more likely that these differences originate in the accretion flows and outflows. The absorption features (from outflows) can be quite strong, but are stochastic and not directly correlated with ac-

cretion. Additionally, each Balmer line has a different sensitivity to the flow’s temperature and optical depth (Muzerolle et al. 2001), leading to different variability between each line since they probe different parts of the accretion flow. Previous accretion shock modeling shows that the accretion occurs along columns of different radial density profiles (e.g. Ingleby et al. 2013; Robinson & Espaillat 2019; Espaillat et al. 2021; Pittman et al. 2022). Material of different densities has different contributions to the Balmer lines and so the accretion rates derived from these lines may be different from one another or from that of the total flow, as measured by the accretion shock model.

### 3.1.2. Non-Balmer Lines

Beyond the three bright Balmer lines described above, we also focus on 7 additional He lines present in most of our optical spectra. These are listed in Table 2. In general, these lines exhibit similar variability when compared to the Balmer lines, though with additional scatter. In GM Aur, some of these lines are not detected, resulting in near- or sub-zero fluxes.

Alcalá et al. (2017) simultaneously and self-consistently estimate the accretion luminosities and line luminosities of 92 YSOs and derive relationships between these parameters. For every line they study, they find strong correlations, suggesting a connection between optical line luminosity and accretion luminosity. We use these same relationships to estimate mean accretion luminosities in our sample. These results are shown in Figure 3.

Besides  $H\delta$ , the Balmer lines, which tend to be bright and robustly detected in all observations, provide the most consistent  $L_{\text{acc}}$  as compared to our shock modeling from Paper I. On average,  $H\alpha$ ,  $H\beta$ , and  $H\gamma$  are consistent to within 0.5 dex (a factor of  $\sim 3$ ), with  $H\alpha$  typically being closest. That said, there is little consistency as to whether an epoch with higher median accretion also sees brighter median emission lines; only in RU Lup are the lines dimmer in conjunction with the lower accretion rate in Epoch 2. Some He lines (in particular He I<sub>4471</sub>, He I<sub>5875</sub>, and He I<sub>7065</sub>) are generally equally as consistent as the Balmer lines. The other lines can deviate by up 1.5 dex (a factor of  $\sim 30$ ) with large uncertainties. Like the Balmer lines, fluxes of the He lines, and therefore their use with the Alcalá et al. (2017) relationships, are sensitive to the adopted value of extinction.

### 3.2. Optical Veiling

The strong continuum emission produced by the accretion process at optical wavelengths can be comparable to the underlying photospheric emission. This can act to “fill-in” absorption lines in a process called *veiling*. Estimating the veiling is important not only for the accretion shock model (see Paper I), but is closely tied to accretion (e.g. Ingleby et al. 2013; Sousa et al. 2023; Herczeg et al. 2023; Nelissen et al. 2023). These veiling measurements, along with contemporaneous  $V$ -band photometry from Paper II, are used to scale WTTS spectra as accurate photospheric templates in Paper I.

We estimate veiling in our optical spectra following the basic method of Hartigan et al. (1989). First, after convolving our de-reddened (assuming constant  $A_V$ , see Paper I) target and template spectra to a uniform wavelength grid, we split them into 75 Å intervals, removing intervals with missing data or that overlap with bright emission lines like  $H\alpha$  and  $H\beta$ . Then for each

interval, we perform continuum normalization by fitting a 3rd degree polynomial to non-outlying points. After continuum normalization, we align the target and template spectra using cross-correlation. Next, we add some fraction of the template continuum (a flat, featureless spectrum) to the target spectrum and calculate the Root Mean Square Error (RMSE) between the target and template spectra. The added continuum varies between 0–300% of the template continuum level. The fractional veiling in each 75 Å bin is the added continuum that minimizes the dispersion between the target and template spectra, divided by the template continuum level. Finally, we fit a 3rd degree polynomial to all the fractional veilings, and  $r_V$  is the value of this fitted curve at  $\lambda=5500$  Å. We apply a Monte Carlo approach to this procedure, repeating the veiling calculation 500 times on a noise-added spectrum. This acts to minimize noise and outliers. We do not consider rotational broadening in our calculation of  $r_V$ , as some others do (e.g., Frasca et al. 2016; Manara et al. 2020). However, tests with rotational broadening showed  $r_{VS}$  about 0.1 larger, in turn resulting in accretion rates about 2.1%, 6.3%, and 2.9% higher for TW Hya, BP Tau, and GM Aur, respectively, which does not significantly impact any of the results reported here.

Veiling estimates for TW Hya, BP Tau, and GM Aur are shown in Figure 4 and Appendix A (Tables 5–8). Note that because of an abundance of emission lines in its optical spectra (due to its high accretion rate), we are unable to determine  $r_V$  for RU Lup.  $r_V$  in TW Hya varies between 0.12–1.83, with generally higher values in E2. BP Tau is typically more strongly veiled than TW Hya, with  $r_V$  between 0.40–1.87. GM Aur is the least veiled in our sample, with  $r_V$  typically between 0.16–0.84.

### 3.3. Accretion Flow Modeling

We utilize the accretion flow models of Hartmann et al. (1994) and Muzerolle et al. (1998a, 2001). These models assume an axisymmetric accretion flow from the surrounding gas disk. This flow follows along the magnetic field structure, which is assumed to be dipolar and aligned with the stellar rotation axis. The flow is parameterized by the disk truncation radius ( $R_{in}$ ), the width of the flow ( $W_r$ ), the mass accretion rate ( $\dot{M}$ ), the maximum temperature of the flow ( $T_{max}$ ) and the viewing inclination angle ( $i$ ). After preliminary tests using a large, coarse grid for  $H\alpha$ , we create a smaller, finer grid of models for each target, with ranges of parameters shown in Table 3. In nearly all cases of fitting  $H\alpha$ , the resulting parameters are far from the parameter bounds. Only in a few cases for TW Hya, BP Tau, and GM Aur does our



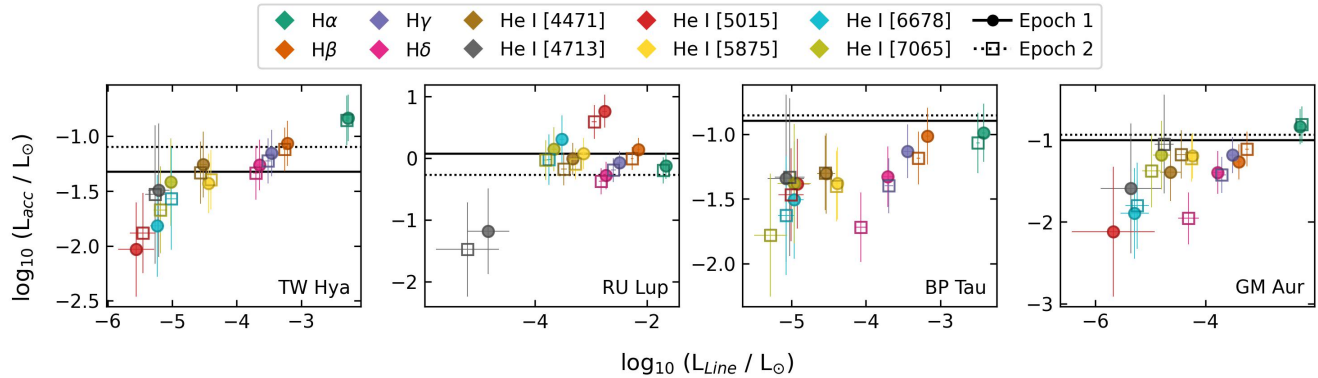


**Figure 3.** Median line luminosities converted to accretion luminosities using the empirical relationships of Alcalá et al. (2017). Filled circles denote  $L_{\text{acc}}$  from Epoch 1, while open squares denote Epoch 2. Lines are the median  $L_{\text{acc}}$  from the shock modeling from Paper I, where the solid/dotted lines are E1/E2. Marker colors denote different lines; see the legend.

fitting suggest that the flow width,  $W_r$ , is smaller than the lower bound of our grid, typically  $0.1 R_*$ .  $H\beta$  and  $H\gamma$  also prefer  $W_r$  below the lower bound of our grid. We do not expand our grid to smaller  $W_r$  than  $0.1 R_*$ , as even  $0.1 R_*$  is smaller than expected from 3D MHD modeling (e.g., Zhu et al. 2023). Additionally, such thin accretion flows would map to correspondingly small filling factors (Muzerolle et al. 2001), but our shock modeling from Paper I reveals modest filling factors up to 40%.

To ensure consistent wavelength calibration for each fitted profile, we perform further wavelength calibration for  $H\alpha$ ,  $H\beta$ , and  $H\gamma$ . We select  $\sim 100 \text{ \AA}$ -wide regions to the left and right of the line center, making sure not to include the extended wings. We then performed cross-correlation on these regions against a template BT-SETTL (Allard 2014) photosphere model spectrum and applied the highest-power wavelength shift to the observed line spectrum. We found that the intrinsic wavelength calibration is generally consistent to within  $0.3 \text{ \AA}$  for our CHIRON, X-Shooter, UVES, and TCES spectra, but was often off by up to  $2 \text{ \AA}$  for our ESPRESSO spectra. Here we use all observations, as the flow model does not require flux-calibrated spectra.

When performing the flow model fitting, because of the complex line shapes, generally due to blue-shifted absorption which the model does not account for, we exclude several regions in the spectra from fitting. For  $H\alpha$ , this is  $-100$  to  $0 \text{ km s}^{-1}$  for TW Hya,  $-100$  to  $+50 \text{ km s}^{-1}$  for RU Lup, no mask for BP Tau, and  $-200$  to  $+50 \text{ km s}^{-1}$  for GM Aur. For  $H\beta$  and  $H\gamma$ , we only mask between  $\pm 50 \text{ km s}^{-1}$  for RU Lup. In some cases, spurious emission/absorption features can appear within our fitted regions that deviate significantly from any fitted model, which can affect the final fit, but in general these

masked regions contained persistent features that could not be fitted by any model.

Aside from these masked regions, we fit our grid of models between  $\pm 500 \text{ km s}^{-1}$ , roughly consistent with the free-fall velocity of each target. For each line, we then fit our grid of models and select the 500 best-fitting models according to the Mean Absolute Percent Error (MAPE) between the model and the observed spectrum. Using these 500 best-fit models, we then calculate weighted averages for the output parameters, where the weights are the inverse MAPE values for each model. Uncertainties are taken as the weighted standard deviation of those models. Example fits for well-fitting observation for each target are shown in Figure 5, while fits for poorly-fit observations are shown in Figure 8 in Appendix A.

In principle, all lines could be fit simultaneously for each observation, but we elect to fit each line separately in order to gauge how the model responds to the variability in each line. The accretion rates from  $H\alpha$  exhibited the closest agreement to the accretion rates derived from shock modeling in Paper I. To that end, the results of our modeling for just  $H\alpha$  are shown in Figure 6, while Table 4 shows the median values of our flow modeling for each object and line. Tables 5–8 show the results for all  $H\alpha$  observations.

### 3.3.1. Modeling Results for TW Hya

The median accretion rates estimated by the flow model for TW Hya are  $0.4/0.5 \times 10^{-8} M_{\odot} \text{ yr}^{-1}$ ,  $0.5/0.6 \times 10^{-8} M_{\odot} \text{ yr}^{-1}$ , and  $0.6/0.6 \times 10^{-8} M_{\odot} \text{ yr}^{-1}$  in E1/E2 for  $H\alpha$ ,  $H\beta$ , and  $H\gamma$ , respectively. The median accretion rates from the shock model (see Paper I) are  $0.22/0.37 \times 10^{-8} M_{\odot} \text{ yr}^{-1}$  for E1/E2.  $H\beta$  and  $H\gamma$  pro-



**Table 3.** Accretion Flow Model Grid Parameters

Object	$R_{in}$ [ $R_{\odot}$ ]	$W_r$ [ $R_{\odot}$ ]	$\dot{M}$ [ $1 \times 10^{-8} M_{\odot} \text{ yr}^{-1}$ ]	$T_{max}$ [K]	Incl. [ $^{\circ}$ ]
TW Hya	1.5–6.0 (0.3)	0.1–1.9 (0.3)	0.01–0.7 (0.03)	7500–10700 (400)	3–30 (3)
RU Lup	1.4–6.2 (0.3)	0.2–2.4 (0.2)	2.25–20.0 (0.75)	6000–10800 (300)	5–45 (5)
BP Tau	1.5–6.0 (0.3)	0.1–2.2 (0.3)	0.2–6.0 (0.025)	7000–9800 (400)	25–57 (4)
GM Aur	1.2–6.0 (0.4)	0.1–2.1 (0.2)	0.1–0.98 (0.04), 1.0–5.5 (0.4)	7500–11000 (400)	35–67 (4)

NOTE—Hyphenated numbers denote the range of each parameter, while parenthesis denote step size.

**Table 4.** Median flow model results

Object	Line	Epoch	$\dot{M}$ [ $1 \times 10^{-8} M_{\odot} \text{ yr}^{-1}$ ]	$R_{in}$ [ $R_{\star}$ ]	$W_r$ [ $R_{\star}$ ]	$T_{max}$ [K]	Incl. [ $^{\circ}$ ]	MAPE
TW Hya	H $\alpha$	1	0.37 (0.05)	3.84 (0.55)	0.34 (0.16)	9173 (398)	16.6 (1.1)	0.14 (0.03)
		2	0.49 (0.07)	3.58 (0.45)	0.33 (0.09)	9450 (239)	16.7 (0.8)	0.15 (0.03)
TW Hya	H $\beta$	1	0.53 (0.03)	2.00 (0.27)	0.19 (0.11)	9751 (98)	16.2 (0.9)	0.13 (0.03)
		2	0.55 (0.03)	1.70 (0.17)	0.12 (0.04)	9803 (119)	16.1 (0.7)	0.18 (0.06)
TW Hya	H $\gamma$	1	0.59 (0.02)	1.77 (0.12)	0.11 (0.01)	9923 (89)	16.9 (0.8)	0.19 (0.02)
		2	0.58 (0.03)	1.68 (0.12)	0.11 (0.01)	9843 (150)	17.3 (0.6)	0.22 (0.04)
RU Lup	H $\alpha$	1	7.98 (0.15)	3.43 (0.29)	0.72 (0.07)	7476 (75)	20.4 (0.2)	0.15 (0.02)
		2	8.06 (0.11)	3.61 (0.18)	0.71 (0.05)	7441 (62)	20.6 (0.1)	0.16 (0.01)
RU Lup	H $\beta$	1	7.63 (0.86)	3.30 (0.35)	0.90 (0.24)	8734 (217)	20.5 (0.3)	0.11 (0.01)
		2	8.38 (0.87)	3.57 (0.33)	1.14 (0.33)	8420 (93)	21.4 (0.4)	0.14 (0.02)
RU Lup	H $\gamma$	1	8.25 (0.93)	2.83 (0.36)	1.10 (0.27)	9394 (228)	21.0 (0.3)	0.19 (0.03)
		2	10.03 (1.49)	3.90 (0.72)	1.29 (0.39)	8761 (184)	21.5 (0.4)	0.16 (0.04)
BP Tau	H $\alpha$	1	2.01 (0.15)	3.57 (0.16)	0.70 (0.26)	8212 (146)	43.7 (1.2)	0.13 (0.01)
		2	2.22 (0.14)	3.01 (0.25)	0.65 (0.22)	8127 (146)	43.7 (1.5)	0.11 (0.02)
BP Tau	H $\beta$	1	4.07 (0.44)	2.42 (0.14)	1.03 (0.30)	9080 (189)	42.0 (2.6)	0.08 (0.02)
		2	4.31 (0.36)	2.19 (0.19)	1.06 (0.32)	9240 (229)	41.9 (2.0)	0.09 (0.02)
BP Tau	H $\gamma$	1	4.46 (0.77)	2.57 (0.30)	0.82 (0.41)	9166 (443)	45.4 (2.1)	0.19 (0.12)
		2	4.62 (0.51)	2.29 (0.28)	0.76 (0.28)	9287 (387)	43.3 (2.3)	0.14 (0.02)
GM Aur	H $\alpha$	1	1.04 (0.26)	3.11 (0.33)	0.30 (0.17)	9781 (186)	52.7 (2.4)	0.13 (0.01)
		2	1.01 (0.15)	3.01 (0.15)	0.30 (0.07)	9753 (157)	53.1 (2.4)	0.12 (0.01)
GM Aur	H $\beta$	1	2.23 (1.18)	1.90 (0.21)	0.30 (0.20)	9604 (521)	53.7 (1.8)	0.13 (0.03)
		2	2.85 (0.67)	2.12 (0.24)	0.53 (0.20)	9853 (266)	54.5 (1.5)	0.11 (0.04)
GM Aur	H $\gamma$	1	3.56 (0.59)	2.00 (0.42)	0.43 (0.22)	10159 (151)	54.9 (2.7)	0.17 (0.03)
		2	2.45 (1.08)	2.37 (0.56)	0.44 (0.21)	9838 (359)	54.2 (3.4)	0.17 (0.04)

NOTE—Values are the median value for the given parameter in E1/E2. Values in parentheses are the standard deviation of the given parameter in E1/E2.

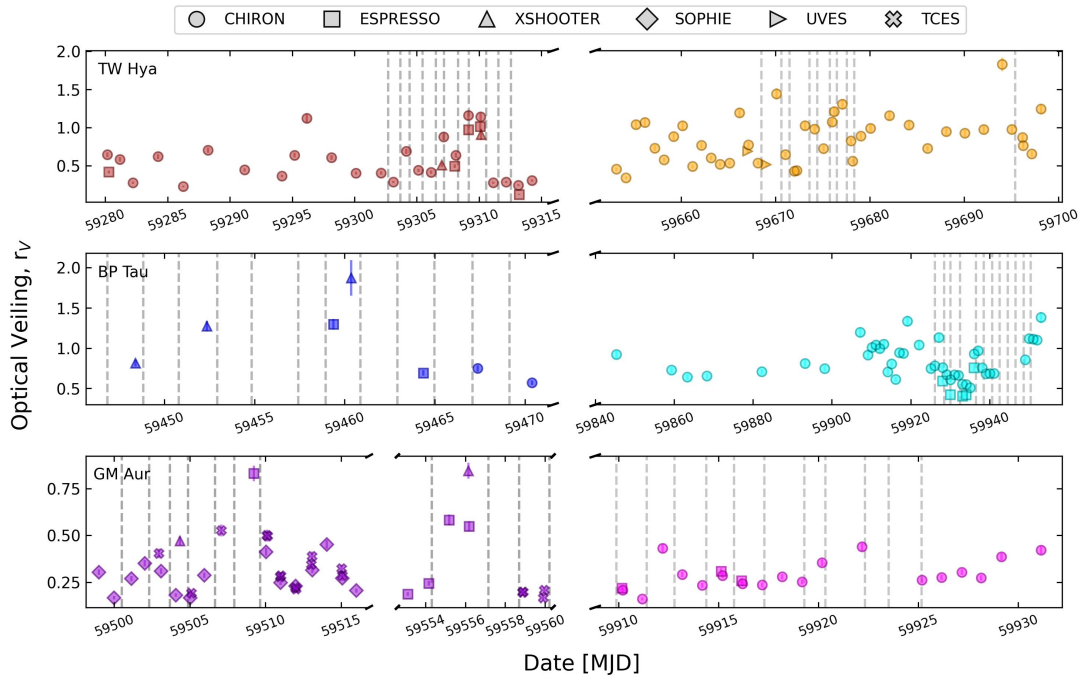


**Figure 4.** Optical veiling ( $r_V$ ) estimates for TW Hya (red/orange, top row), BP Tau (blue/cyan, middle row), and GM Aur (purple/pink, bottom row). We do not estimate  $r_V$  for RU Lup due to the abundance of strong emission lines.

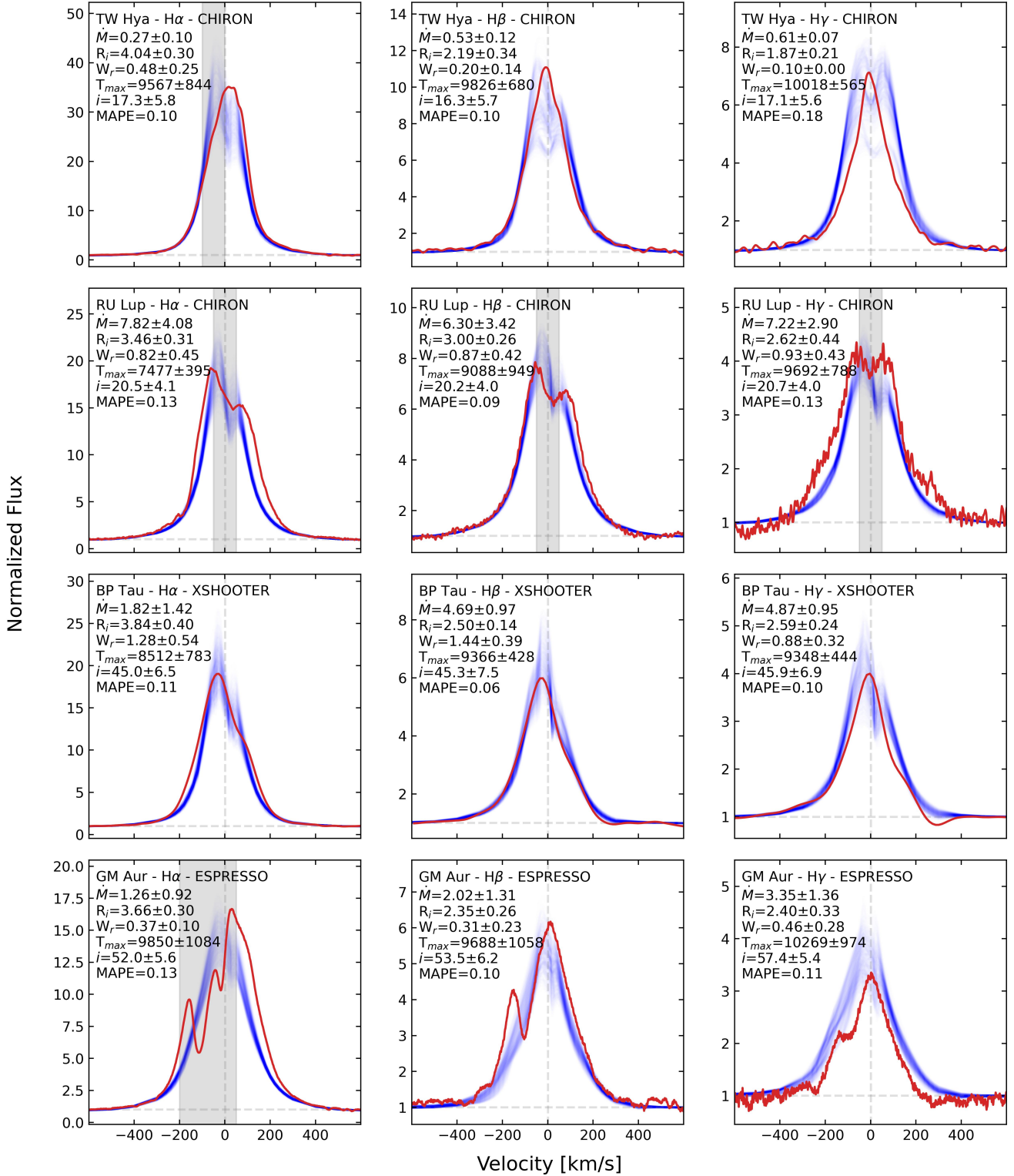


**Figure 5.** Examples of flow model fits for the best-fit observation for each target. Top to bottom: TW Hya, RU Lup, BP Tau, GM Aur. Left to right: H $\alpha$ , H $\beta$ , H $\gamma$ . Solid red line is observed spectrum. Blue lines are 500 best-fit models. Grey regions denote regions not fit by the flow model. Examples of the worst-fit observations can be found in Figure 8.

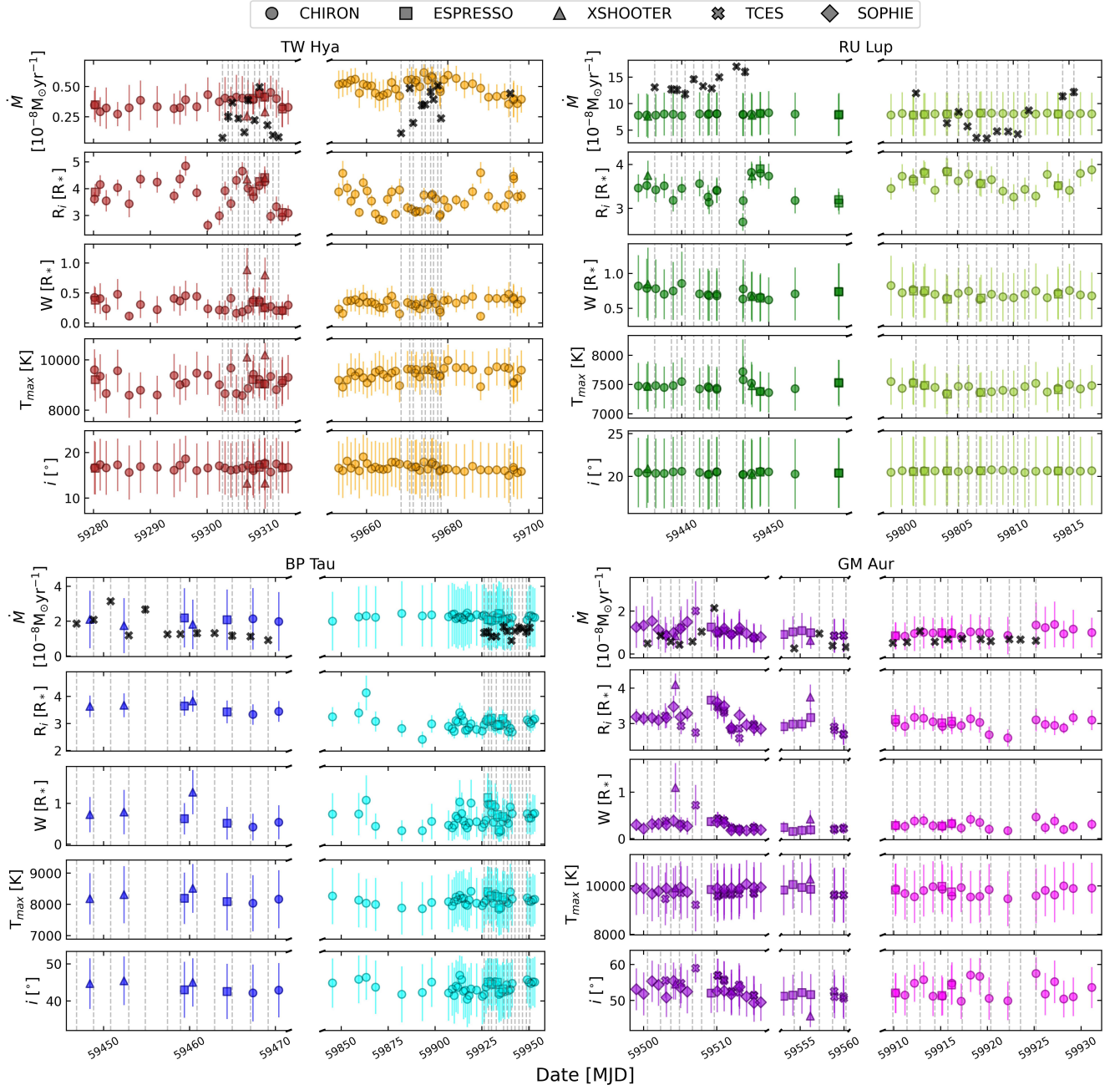


**Figure 6.**  $H\alpha$  flow model results for TW Hya (top left), RU Lup (top right), BP Tau (bottom left), and GM Aur (bottom right). For each target, left/right are E1/E2 while top to bottom are  $\dot{M}$ ,  $R_{in}$ ,  $W$ ,  $T_{max}$ , and  $i$ . Marker shape refers to the instrument (see legend). Black crosses in top row of each panel are accretion rates from shock modeling from Paper I.

duce accretion rates at or near the upper boundaries set by our grid.

H $\alpha$  most closely recovers the shock model accretion rates in E1, while H $\beta$  does in E2 (though H $\beta$  is highly inconsistent with  $\dot{M}$  derived in Paper I in E1). In general, though, all 3 lines recover the median accretion rate consistent to within about a factor of 2 in both epochs. The variability in  $\dot{M}$  is lower in the flow models, with a standard deviation between all H $\alpha$  observations of  $0.06 \times 10^{-8} M_{\odot} \text{ yr}^{-1}$  for the flow model compared to  $\sim 0.13 \times 10^{-8} M_{\odot} \text{ yr}^{-1}$  for the shock model.

$R_{in}$  is comparably low for both H $\beta$  and H $\gamma$  ( $\sim 1.5$ – $2.8 R_{\star}$ ), but is higher for H $\alpha$  ( $2.6$ – $4.8 R_{\star}$ ). For all three lines,  $R_{in}$  is lower in E2.  $W_r$  is very low in H $\beta$  and H $\gamma$ , in most cases preferring the lower bound of our grid ( $0.1 R_{\star}$ ), but for H $\alpha$  the median is  $0.33 R_{\star}$ .  $T_{max}$  and  $i$  are lowest for H $\alpha$  and highest for H $\gamma$ .

The flow model appears to fit H $\alpha$  and H $\gamma$  equally well (average MAPEs are 0.14 and 0.16) in E1 and for some of the later visits in E2, but the earlier visits in E2 with particularly strong blue-shifted emission are poorly fit. Thus, observations between MJD=59653~59680 should be considered carefully.

### 3.3.2. Modeling Results for RU Lup

The median accretion rates estimated by the flow model for RU Lup are  $8.0/8.1 \times 10^{-8} M_{\odot} \text{ yr}^{-1}$ ,  $7.6/8.4 \times 10^{-8} M_{\odot} \text{ yr}^{-1}$ , and  $8.2/10.0 \times 10^{-8} M_{\odot} \text{ yr}^{-1}$  in E1/E2 for H $\alpha$ , H $\beta$ , and H $\gamma$ , respectively. The median accretion rates from the shock model (see Paper I) are  $13.2/6.1 \times 10^{-8} M_{\odot} \text{ yr}^{-1}$  for E1/E2. The standard deviation of the accretion rates for all observations (reflective of the accretion variability) is about  $1 \times 10^{-8} M_{\odot} \text{ yr}^{-1}$ , lower than the  $\sim 2 \times 10^{-8} M_{\odot} \text{ yr}^{-1}$  for the shock model. Thus, the flow model is unable to recover the accretion rate specific to either epoch, but does recover accretion rates within about a factor of 2. It also does not recover the variability in the accretion rate, producing much less variability overall.

For  $R_{in}$ , we find  $3.4/3.6 R_{\star}$ ,  $3.3/3.6 R_{\star}$ , and  $2.8/3.9 R_{\star}$  in E1/E2 for H $\alpha$ , H $\beta$ , and H $\gamma$ . Overall, this is lower than the typically assumed  $5 R_{\star}$ , but like TW Hya, H $\beta$  and H $\gamma$  yield lower values.  $W_r$  is about 0.7, 1.0, and 1.2 for H $\alpha$ , H $\beta$ , and H $\gamma$ , with little difference between epochs. The flow appears to be cooler than TW Hya, but shows the same behavior where temperature increases towards H $\gamma$ . For all three lines, we find inclinations between  $20$ – $23^{\circ}$ , slightly higher than the assumed inclination of RU Lup  $18.8^{\circ}$ .

Overall, H $\beta$  is fit better than either H $\alpha$  or H $\gamma$ , with median MAPE values of 0.12 for H $\beta$ , but 0.16 and 0.18 for H $\alpha$  and H $\gamma$  across all observations. In all cases,

though, the flow model underestimates the blue-shifted emission and is unable to recover the broad blue wing.

### 3.3.3. Modeling Results for BP Tau

The median accretion rates estimated by the flow model for BP Tau are  $2.0/2.2 \times 10^{-8} M_{\odot} \text{ yr}^{-1}$ ,  $4.1/4.3 \times 10^{-8} M_{\odot} \text{ yr}^{-1}$ , and  $4.5/4.6 \times 10^{-8} M_{\odot} \text{ yr}^{-1}$  in E1/E2 for H $\alpha$ , H $\beta$ , and H $\gamma$ , respectively. The median accretion rates from the shock model (see Paper I) are  $1.3/1.4 \times 10^{-8} M_{\odot} \text{ yr}^{-1}$  for E1/E2. Unlike TW Hya and RU Lup, the flow model over-predicts the accretion rate for all 3 lines in both epochs, though again H $\alpha$  is the closest. With the exception of E1 (whose variability may be skewed by 2 high visits), the variability predicted by the flow model is higher than that of the shock model. In either case, both models suggest the accretion variability in BP Tau is the lowest in our sample.

The truncation radius,  $R_{in}$ , is similar to that of RU Lup:  $2.7$ – $4.1$  in H $\alpha$  and  $\sim 1.6$ – $2.9$  in H $\beta$  and H $\gamma$ , again smaller than  $5 R_{\star}$ . The flow width,  $W_r$ , is comparable across the three lines, from  $0.3$ – $1.5 R_{\star}$ . The flow temperature,  $T_{max}$ , is coolest in H $\alpha$  ( $\sim 8120$  K) and similar in H $\beta$  and H $\gamma$  ( $\sim 9200$  K), higher than H $\alpha$ . The inclinations predicted by all lines vary between  $41^{\circ}$ – $45^{\circ}$ , higher than the true inclination of BP Tau of  $\sim 38^{\circ}$ .

The flow model fits H $\alpha$  well, but like the other targets, is not as broad as the observations. Like H $\alpha$ , the blue-shifted wing in H $\beta$  is narrower in the model. Additionally, the red wing is often poorly fit, as there is often enhanced emission near  $100 \text{ km s}^{-1}$ , though when this emission feature is absent, the red wing is fit well. The flow model also predicts red-shifted absorption that is absent in the data. For H $\gamma$ , the blue wing and central peak are often underestimated by the model, though this may be due to poor continuum subtraction. Like H $\beta$ , the model predicts red-shifted absorption that is absent in the data.

### 3.3.4. Modeling Results for GM Aur

The median accretion rates estimated by the flow model for GM Aur are  $1.04/1.01 \times 10^{-8} M_{\odot} \text{ yr}^{-1}$ ,  $2.2/2.9 \times 10^{-8} M_{\odot} \text{ yr}^{-1}$ ,  $3.6/2.4 \times 10^{-8} M_{\odot} \text{ yr}^{-1}$  in E1/E2 for H $\alpha$ , H $\beta$ , and H $\gamma$ , respectively. The median accretion rates from the shock model (see Paper I) are  $0.58/0.67 \times 10^{-8} M_{\odot} \text{ yr}^{-1}$  for E1/E2.

For  $R_{in}$ , we find  $3.1/3.0 R_{\star}$ ,  $1.9/2.1 R_{\star}$ , and  $2.0/2.4 R_{\star}$  in E1/E2 for H $\alpha$ , H $\beta$ , and H $\gamma$ . For  $W_r$  we find  $0.3/0.3 R_{\star}$ ,  $0.3/0.5 R_{\star}$ , and  $0.4/0.5 R_{\star}$ . For  $T_{max}$  we find  $9780/9750$  K,  $9600/9850$  K, and  $10160/9840$  K. For  $i$  we find  $52.7/53.1^{\circ}$ ,  $53.7/54.5^{\circ}$ , and  $54.9/54.2^{\circ}$ .  $W_r$ ,  $T_{max}$ , and  $i$  are fairly consistent between each line, though they all tend to increase from H $\alpha$  to H $\gamma$ .  $R_{in}$  is



less consistent, with the highest values coming from H $\alpha$  like in the other targets.

Our H $\alpha$  observations of GM Aur show that there are consistent blue- and red-shifted wings that the flow model cannot recover. Low velocity red-shifted emission between about 0–150 km s $^{-1}$  is typically fit by the model, however. The blue wing in H $\beta$  is often fit among the best in our sample, though some observations in E2 exhibit very strong blue-shifted absorption that severely contaminates the model. The red wing is also generally fitted well, though there are cases of enhanced red-shifted emission not recovered by the flow model. GM Aur shows some red-shifted absorption that is recovered by the model. H $\gamma$  is especially noisy in GM Aur and is not fitted well by the model. It also appears to suffer from poor continuum subtraction, like BP Tau.

#### 4. DISCUSSION

Below we compare the flow model results for the three different Balmer lines to each other, compare these results to accretion rates estimated in Paper I using accretion shock modeling, and discuss the inner truncation radii ( $R_{in}$ ) and inclinations ( $i$ ) predicted by the flow model.

##### 4.1. H $\alpha$ vs H $\beta$ vs H $\gamma$

We have modeled three different Balmer lines using our accretion flow model and here we discuss the similarities and differences between those results. First, the top 500 models for each line tended to be equally well fitting. The median MAPEs for all objects and observations were 13.6, 12.4, and 18.0% for H $\alpha$ , H $\beta$ , and H $\gamma$  respectively, meaning the quality of the fits was consistent to within about 5.6%. This suggests that the typical quality of the fits does not vary significantly between the lines. We also see no notable trends in the uncertainties produced by each line, suggesting that each line is equally uncertain for all parameters. The results for each line do differ in their median output parameters, though.

For example, H $\beta$  and H $\gamma$ , in nearly all cases, yield the highest accretion rates. These high accretion rates are on average  $\sim 79\%$  higher than those predicted by H $\alpha$ , which already produces rates higher than predicted by our shock modeling (Paper I). They are also at or above the highest accretion rates estimated for these targets (see Paper I, Section 2). In many cases, especially in TW Hya and BP Tau, these rates are at or near the boundaries of our grid, so an even higher  $\dot{M}$  may be preferred by these lines. H $\beta$  and H $\gamma$  also produce, on average, the lowest truncation radii ( $R_{in}$ ) and the highest flow temperatures ( $T_{max}$ ).  $R_{in}$  is often between (or

even lower than) 2.0–2.5  $R_*$ , which is well below the typically assumed 5  $R_*$  or any observation estimates of  $R_{in}$  for these targets.

Considering their high transition energies, it may be that the upper lines (H $\beta$ , H $\gamma$ ) trace more compact, hotter flows that lay inside of larger, more diffuse flows more closely traced by H $\alpha$ . This more compact flow geometry may then produce higher accretion rates if a roughly constant energy flux in the flow is assumed. From Calvet & Gullbring (1998), the energy flux is  $F \propto 1/(1-1/R_{in})$ . Thus, for a constant energy flux in the accretion flow,  $\dot{M}$  and  $R_{in}$  are inversely proportional, reflective of our results. This layered flow structure was employed in the flow modeling of Thanathibodee et al. (2019) to explain the complex Balmer profiles seen in low accretors. Recent 3D MHD modeling by Zhu et al. (2024) shows precisely this onion-like structure, where multiple, layered flows result in multiple hotspots and “hidden” flows. It may thus be important to incorporate a self-attenuating, multi-layered flow structure in future accretion flow modeling.

Despite these differences, the correlation coefficient,  $r$ , between the accretion rates output by each line are very high:  $r_{\dot{M}, H\alpha-H\beta}=0.92$ ,  $r_{\dot{M}, H\alpha-H\gamma}=0.92$ , and  $r_{\dot{M}, H\beta-H\gamma}=0.95$ . This suggests that the same physical effects that induce variability are manifesting in each line, though our model appears to interpret them differently.

##### 4.2. Accretion Rates: Shock vs Flow

Because of the potential issues in applying the flow model to H $\beta$  and H $\gamma$  described above, and because H $\alpha$  produces  $\dot{M}$  and  $R_{in}$  most consistent with previous work, we consider results using only H $\alpha$  for the flow model for the following discussion. This is in contrast to other studies (e.g., Natta et al. 2004; Herczeg & Hillenbrand 2008; Alcalá et al. 2014; Herczeg et al. 2023), who recommend against using H $\alpha$  to estimate  $\dot{M}$  due to the large spread in the  $L_{acc}-L_{H\alpha}$  relationship and to the many processes that contribute to its emission profile. These previous studies have typically used either the total H $\alpha$  luminosity ( $L_{H\alpha}$ ) or the full width at 10% of the line peak ( $W_{H\alpha, 10\%}$ ) to compare against  $L_{acc}$  or  $\dot{M}$ . Both  $L_{H\alpha}$  and  $W_{H\alpha, 10\%}$  are subject to blue-shifted absorption from an ejected wind, which we show here can be quite strong and variable, which could produce the additional scatter observed. Our flow modeling mitigates the effect of wind absorption by masking the blue regions most susceptible to absorption, which should allow H $\alpha$  to be a more reliable tracer of accretion in CTTSs.

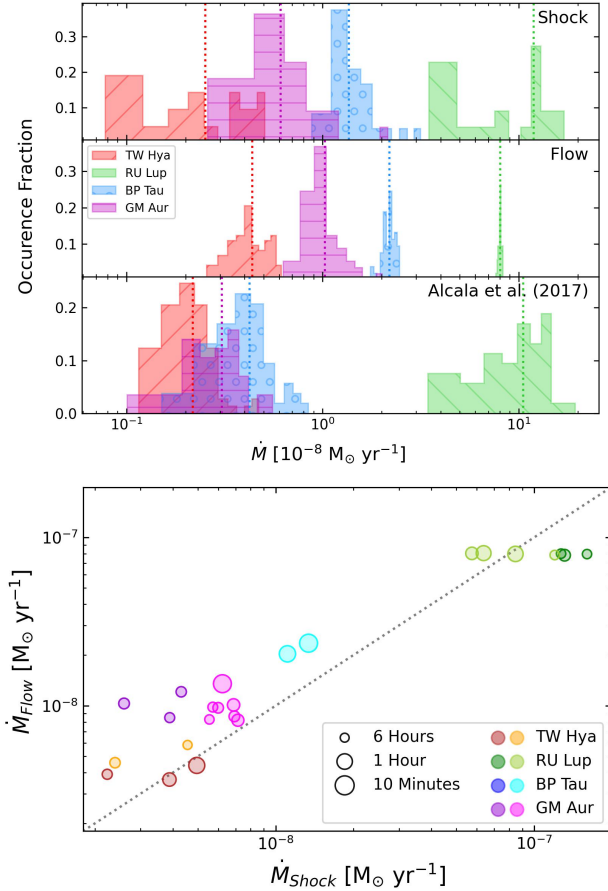


**Figure 7.** *Left:* Histograms of accretion rates from the shock model from Paper I (top row), flow model from  $H\alpha$  from this work (middle row), and using relationships from Alcalá et al. (2017). Colored dotted lines show the median of each distribution. *Right:* Accretion rates from the flow model ( $H\alpha$ ) vs the shock model, where data are contemporaneous to within 6 hours. Larger points represent observations obtained closer in time. For both plots, colors (yellow/red, green, blue, and pink/purple) denote the different targets (TW Hya, RU Lup, BP Tau, and GM Aur).

Figure 7 compares the accretion rates derived from our two models: an accretion shock model (Calvet & Gullbring 1998; Robinson & Espaillat 2019) from Paper I and an accretion flow model (Muzerolle et al. 1998a) used here. The top panel shows the distribution of accretion rates for each target, while the bottom panel directly compares contemporaneous accretion rate measurements.

With the exception of RU Lup, the flow model produces median accretion rates that are 51%, 47%, and 46% higher than the shock model for TW Hya, BP Tau, and GM Aur, respectively, showing that the flow model can recover accretion rates that generally describe the system (i.e., within a factor of 2). When looking at

the contemporaneous rates, though, these differences become 40%, 79%, and 103%, showing that changes in the accretion are not consistently recovered between the shock and flow models. The median rate predicted by the flow model for RU Lup is about 21% less than the shock model and 23% less for contemporaneous observations. Additionally, the flow model produces significantly less variability than the shock model, both in terms of variance and range.

Espaillat et al. (2021) use the same shock and flow (using only  $H\alpha$ ) models to estimate the accretion rate of GM Aur across  $\sim 1$  week of *HST* observations and  $\sim 3$  weeks of daily CHIRON observations. They also found that, on average, the flow model over-predicted the shock model by 42% and by 30% for contemporaneous data. Thanathibodee et al. (2018) also use the same flow model and a single-column version of our shock model to estimate accretion rates of low accretors, where  $\dot{M} \lesssim 10^{-9} M_{\odot} \text{yr}^{-1}$ . Here, the shock model generally produced higher accretion rates than the flow model ( $\sim 27\%$ ), though they note that their  $\dot{M}_{\text{Shock}}$  are likely upper limits.

Our findings, along with previous use of these models, suggest that the flow model is able to recover accretion rates in line with quiescent accretion in these systems (as predicted by our shock modeling in Paper I), but cannot accurately reproduce accretion variability, and in some cases it produces effectively no variability. Some of these results could be due to the built-in assumption of the flow model: that it is axisymmetric and that mass flows from the disk onto the star in both the upper and lower hemispheres. In the shock model, we only measure accretion luminosity from what we see on the visible side of the star. The flow model assumes that mass also flows in on the other “unseen” side. Additionally, the flow model assumes a ring of emission on the stellar surface, so by construction it cannot reproduce variability due to non-axisymmetry of the hotspots themselves.

The accretion rates derived here are also generally in line with previous studies. Using empirical relationships from Alcalá et al. (2017), Gangi et al. (2022) estimate the accretion rate of BP Tau at  $0.56 \times 10^{-8} M_{\odot} \text{yr}^{-1}$  in January 2020. This is consistent with our estimates using those same relationships, which underestimate the accretion rate as compared to our shock modeling in BP Tau specifically. Gangi et al. (2022) also find the accretion rate of GM Aur to be  $0.51 \times 10^{-8} M_{\odot} \text{yr}^{-1}$ , which is at the higher end of our estimates using those empirical relationships, suggesting that GM Aur may have been in an enhanced accretion state during their observations. Armeni et al. (in prep.) estimate the accretion rate of RU Lup also using the empirical relation-

ships from Alcalá et al. (2017) (though only using the He I<sub>5875</sub> line), finding average rates between  $7\text{--}40 \times 10^{-8} M_{\odot} \text{ yr}^{-1}$ . These accretion rates are roughly consistent with, though slightly higher than, our findings using any method. Armeni et al. (in prep.) also see that the accretion rate in RU Lup in 2022 is about half that of 2021.

The top panel of Figure 7 also shows a comparison of accretion rates calculated using the 11 emission lines from Section 3 and the empirical relationships of Alcalá et al. (2017) to those calculated using the shock model (Paper I) and the flow model. The empirical relationships produce similar accretion rates as compared to the shock model in TW Hya and RU Lup:  $\sim 23.8\%$  lower in TW Hya and  $4.7\%$  higher in RU Lup. Accretion rates in BP Tau and GM Aur are  $71.9\%$  and  $56.1\%$  lower using the Alcalá et al. (2017) relationships. This further reinforces that while these empirical relationships can provide accurate accretion rates in some cases, they fail in others and should be used sparingly in studies of variability.

#### 4.3. Truncation Radius and Stellar Inclination

The flow model appears capable of recovering inclinations and truncation radii that are consistent with current theory and previous studies. The flow model assumes aligned rotation and magnetic axes, which is often not the case (Donati et al. 2007, 2008, 2010, 2011), so there is additional uncertainty on our predicted inclinations. These axes tend to be misaligned by up to  $20^{\circ}$ , making the flow model’s predictions consistent with previous estimates.

Using high spatial resolution Br<sub>γ</sub> spectra, TW Hya’s inner truncation radius ( $R_{in}$ ) has been estimated between  $3.5\text{--}12.35 R_{\star}$  (Gravity Collaboration et al. 2020, 2023), depending on the treatment of the data and assumed stellar parameters. Our median estimate of  $3.7 \pm 0.5 R_{\star}$  is consistent with these studies and is only slightly smaller than the typically assumed  $5 R_{\star}$ . Those studies also fitted for inclination and found  $i = 14_{-14}^{+6} \text{ }^{\circ}$ , consistent both with our estimate of  $\sim 17^{\circ}$  and with the assumed value of  $7^{\circ}$ . RU Lup’s  $R_{in}$  was also estimated by Gravity Collaboration et al. (2023) using Br<sub>γ</sub>. They found  $R_{in} = 3.3\text{--}6.6 R_{\star}$  from two distinct observations, consistent with our finding of  $3.5 \pm 0.3 R_{\star}$ . They find  $i$  between  $12\text{--}24^{\circ}$ , also consistent with our findings ( $\sim 20.5^{\circ}$ ) and previous studies. Our estimate of  $R_{in}$  for BP Tau ( $R_{in} = 3.2 \pm 0.4 R_{\star}$ ) is consistent with 3D magnetospheric accretion models (Long et al. 2011), which place  $R_{in}$  between  $3.6\text{--}7 R_{\star}$ , depending on the assumed stellar parameters, especially the accretion rate. We estimate median  $i$  of  $43.7 \pm 1.3^{\circ}$ , higher and inconsis-

tent with our assumed value of  $38.2^{\circ}$ . And finally, our flow model places  $R_{in}$  between  $2.6\text{--}4.1 R_{\star}$  in GM Aur, though no other study can place this into further context. The flow model recovers inclinations ( $53 \pm 2.4^{\circ}$ ) consistent with previous work.

## 5. SUMMARY

We conducted a comprehensive multi-wavelength, multi-epoch monitoring campaign of 4 CTTSs (TW Hya, RU Lup, BP Tau, and GM Aur), including *HST* UV spectra (see Paper I), contemporaneous optical light curves (see Paper II), and contemporaneous optical spectra, which is the focus of this paper. Here we model the H $\alpha$ , H $\beta$ , and H $\gamma$  emission line profiles using a magnetospheric accretion flow model to estimate the accretion characteristics of these CTTSs over many stellar rotations in both 2021 and 2022. We also measure optical line luminosities and compare with empirical relationships. Our main findings are as follows:

1. Averaged across multiple observations, our accretion flow model reproduces accretion rates that are consistent to within a factor of 2 when compared to the shock modeling using *HST* UV spectra from Paper I. Additionally, it typically recovers inner truncation radii and stellar inclinations consistent with previous studies.
2. While the accretion rates from all three Balmer lines are highly correlated and show similar variability trends, H $\alpha$  produces accretion rates most similar to those obtained using accretion shock modeling from Paper I. H $\beta$  and H $\gamma$  systematically produce the highest accretion rates, the smallest truncation radii, and the highest flow temperatures when compared to H $\alpha$ . Thus, we suggest that when the variable absorption components are properly mitigated, H $\alpha$  (among the Balmer lines) is the most reliable tracer of the accretion rate in CTTSs, but still fails to recover variability.
3. Our results suggest that the magnetic truncation radius is typically between  $2.5\text{--}5 R_{\star}$ , and is between  $3\text{--}4 R_{\star}$  in most cases.
4. Like UV emission lines in Paper I and photometry in Paper II, optical emission lines are useful for estimating accretion rates in CTTSs but should be used with caution. Using empirical relationships, several lines yield consistent accretion luminosities as accretion shock modeling, but the variability trends differ, suggesting that optical emission lines are a poor direct tracer of accretion variability.

Our results here reinforce that UV spectra remain the best tool to understand the accretion rate in CTTSs, particularly variability. However, optical spectra can provide useful information about the accretion such as the average accretion rate and magnetospheric geometry. Further, this small sample shows the diversity in CTTSs, that variability characteristics and line morphologies can differ considerably between targets.

It is also important to emphasize that emission from CTTSs is highly variable at all wavelengths from the UV to the NIR and beyond. Future studies of individual CTTSs should incorporate simultaneous, multi-wavelength spectra from the UV to the NIR to obtain the most accurate picture of accretion.

This material is based upon work supported by the National Science Foundation under Grant Number AST-2108446. This work is supported by *HSTAR*-16129 from the Space Telescope Science Institute, which is operated by AURA, Inc. This work has been supported by Deutsche Forschungsgemeinschaft (DFG) in the framework of the YTTTHACA Project (469334657) under the project code EI 409/20-1. Funded by the European Union (ERC, WANDA, 101039452). Views and opinions expressed are however those of the author(s) only and do not necessarily reflect those of the European Union or the European Research Council Executive Agency. Neither the European Union nor the granting authority can be held responsible for them. This work was also supported by the NKFIH excellence grant TKP2021-NKTA-64.

We thank Todd Henry and the CHIRON team for their prompt scheduling of the CHIRON observations. This work benefited from discussions with the ODYSSEUS team (<https://sites.bu.edu/odysseus/>); see [Espaillat et al. \(2022\)](#) for an overview of the ODYSSEUS survey.

*Facilities:* HST (COS), CTIO:1.5m, VLT, TLS

*Software:* Python, specutils, astropy

## REFERENCES

- Alcalá, J. M., Natta, A., Manara, C. F., et al. 2014, *A&A*, 561, A2, doi: [10.1051/0004-6361/201322254](https://doi.org/10.1051/0004-6361/201322254)
- Alcalá, J. M., Manara, C. F., Natta, A., et al. 2017, *A&A*, 600, A20, doi: [10.1051/0004-6361/201629929](https://doi.org/10.1051/0004-6361/201629929)
- Alencar, S. H. P., Bouvier, J., Walter, F. M., et al. 2012, *A&A*, 541, A116, doi: [10.1051/0004-6361/201118395](https://doi.org/10.1051/0004-6361/201118395)
- Allard, F. 2014, in *Exploring the Formation and Evolution of Planetary Systems*, ed. M. Booth, B. C. Matthews, & J. R. Graham, Vol. 299, 271–272, doi: [10.1017/S1743921313008545](https://doi.org/10.1017/S1743921313008545)
- Armeni, A., Stelzer, B., Frasca, A., et al. in prep., *A&A*
- Blinova, A. A., Romanova, M. M., & Lovelace, R. V. E. 2016, *MNRAS*, 459, 2354, doi: [10.1093/mnras/stw786](https://doi.org/10.1093/mnras/stw786)
- Bouvier, J., Sousa, A., Pouilly, K., et al. 2023, *A&A*, 672, A5, doi: [10.1051/0004-6361/202245342](https://doi.org/10.1051/0004-6361/202245342)
- Calvet, N., & Gullbring, E. 1998, *ApJ*, 509, 802, doi: [10.1086/306527](https://doi.org/10.1086/306527)
- Dekker, H., D’Odorico, S., Kaufer, A., Delabre, B., & Kotzlowski, H. 2000, in *Society of Photo-Optical Instrumentation Engineers (SPIE) Conference Series*, Vol. 4008, *Optical and IR Telescope Instrumentation and Detectors*, ed. M. Iye & A. F. Moorwood, 534–545, doi: [10.1117/12.395512](https://doi.org/10.1117/12.395512)
- Donati, J. F., Jardine, M. M., Gregory, S. G., et al. 2007, *MNRAS*, 380, 1297, doi: [10.1111/j.1365-2966.2007.12194.x](https://doi.org/10.1111/j.1365-2966.2007.12194.x)
- . 2008, *MNRAS*, 386, 1234, doi: [10.1111/j.1365-2966.2008.13111.x](https://doi.org/10.1111/j.1365-2966.2008.13111.x)
- Donati, J. F., Skelly, M. B., Bouvier, J., et al. 2010, *MNRAS*, 409, 1347, doi: [10.1111/j.1365-2966.2010.17409.x](https://doi.org/10.1111/j.1365-2966.2010.17409.x)
- Donati, J. F., Gregory, S. G., Alencar, S. H. P., et al. 2011, *MNRAS*, 417, 472, doi: [10.1111/j.1365-2966.2011.19288.x](https://doi.org/10.1111/j.1365-2966.2011.19288.x)
- Dupree, A. K., Brickhouse, N. S., Cranmer, S. R., et al. 2014, *ApJ*, 789, 27, doi: [10.1088/0004-637X/789/1/27](https://doi.org/10.1088/0004-637X/789/1/27)
- Espaillat, C., Muzerolle, J., Hernández, J., et al. 2008, *ApJL*, 689, L145, doi: [10.1086/595869](https://doi.org/10.1086/595869)



- Espaillet, C. C., Robinson, C. E., Romanova, M. M., et al. 2021, *Nature*, 597, 41, doi: [10.1038/s41586-021-03751-5](https://doi.org/10.1038/s41586-021-03751-5)
- Espaillet, C. C., Herczeg, G. J., Thanathibodee, T., et al. 2022, *AJ*, 163, 114, doi: [10.3847/1538-3881/ac479d](https://doi.org/10.3847/1538-3881/ac479d)
- Fiorellino, E., Manara, C. F., Nisini, B., et al. 2021, *A&A*, 650, A43, doi: [10.1051/0004-6361/202039264](https://doi.org/10.1051/0004-6361/202039264)
- Fischer, W. J., Hillenbrand, L. A., Herczeg, G. J., et al. 2023, in *Astronomical Society of the Pacific Conference Series*, Vol. 534, *Protostars and Planets VII*, ed. S. Inutsuka, Y. Aikawa, T. Muto, K. Tomida, & M. Tamura, 355, doi: [10.48550/arXiv.2203.11257](https://doi.org/10.48550/arXiv.2203.11257)
- Frasca, A., Biazzo, K., Alcalá, J. M., et al. 2017, *A&A*, 602, A33, doi: [10.1051/0004-6361/201630108](https://doi.org/10.1051/0004-6361/201630108)
- Frasca, A., Molenda-Żakowicz, J., De Cat, P., et al. 2016, *A&A*, 594, A39, doi: [10.1051/0004-6361/201628337](https://doi.org/10.1051/0004-6361/201628337)
- Gangi, M., Antonucci, S., Biazzo, K., et al. 2022, *A&A*, 667, A124, doi: [10.1051/0004-6361/202244042](https://doi.org/10.1051/0004-6361/202244042)
- Gravity Collaboration, Garcia Lopez, R., Natta, A., et al. 2020, *Nature*, 584, 547, doi: [10.1038/s41586-020-2613-1](https://doi.org/10.1038/s41586-020-2613-1)
- Gravity Collaboration, Wojtczak, J. A., Labadie, L., et al. 2023, *A&A*, 669, A59, doi: [10.1051/0004-6361/202244675](https://doi.org/10.1051/0004-6361/202244675)
- Gullbring, E., Hartmann, L., Briceño, C., & Calvet, N. 1998, *ApJ*, 492, 323, doi: [10.1086/305032](https://doi.org/10.1086/305032)
- Hartigan, P., Hartmann, L., Kenyon, S., Hewett, R., & Stauffer, J. 1989, *ApJS*, 70, 899, doi: [10.1086/191361](https://doi.org/10.1086/191361)
- Hartmann, L., Herczeg, G., & Calvet, N. 2016, *ARA&A*, 54, 135, doi: [10.1146/annurev-astro-081915-023347](https://doi.org/10.1146/annurev-astro-081915-023347)
- Hartmann, L., Hewett, R., & Calvet, N. 1994, *ApJ*, 426, 669, doi: [10.1086/174104](https://doi.org/10.1086/174104)
- Herbert, C., Froebrich, D., & Scholz, A. 2023, *MNRAS*, 520, 5433, doi: [10.1093/mnras/stac3051](https://doi.org/10.1093/mnras/stac3051)
- Herczeg, G. J., & Hillenbrand, L. A. 2008, *ApJ*, 681, 594, doi: [10.1086/586728](https://doi.org/10.1086/586728)
- Herczeg, G. J., Chen, Y., Donati, J.-F., et al. 2023, *ApJ*, 956, 102, doi: [10.3847/1538-4357/acf468](https://doi.org/10.3847/1538-4357/acf468)
- Ingleby, L., Calvet, N., Herczeg, G., et al. 2013, *ApJ*, 767, 112, doi: [10.1088/0004-637X/767/2/112](https://doi.org/10.1088/0004-637X/767/2/112)
- Jönsson, H., Holtzman, J. A., Allende Prieto, C., et al. 2020, *AJ*, 160, 120, doi: [10.3847/1538-3881/aba592](https://doi.org/10.3847/1538-3881/aba592)
- Long, M., Romanova, M. M., Kulkarni, A. K., & Donati, J. F. 2011, *MNRAS*, 413, 1061, doi: [10.1111/j.1365-2966.2010.18193.x](https://doi.org/10.1111/j.1365-2966.2010.18193.x)
- Manara, C. F., Ansdell, M., Rosotti, G. P., et al. 2023, in *Astronomical Society of the Pacific Conference Series*, Vol. 534, *Protostars and Planets VII*, ed. S. Inutsuka, Y. Aikawa, T. Muto, K. Tomida, & M. Tamura, 539, doi: [10.48550/arXiv.2203.09930](https://doi.org/10.48550/arXiv.2203.09930)
- Manara, C. F., Beccari, G., Da Rio, N., et al. 2013, *A&A*, 558, A114, doi: [10.1051/0004-6361/201321866](https://doi.org/10.1051/0004-6361/201321866)
- Manara, C. F., Natta, A., Rosotti, G. P., et al. 2020, *A&A*, 639, A58, doi: [10.1051/0004-6361/202037949](https://doi.org/10.1051/0004-6361/202037949)
- Manara, C. F., Frasca, A., Venuti, L., et al. 2021, *A&A*, 650, A196, doi: [10.1051/0004-6361/202140639](https://doi.org/10.1051/0004-6361/202140639)
- Miotello, A., Kamp, I., Birnstiel, T., Cleeves, L. C., & Kataoka, A. 2023, in *Astronomical Society of the Pacific Conference Series*, Vol. 534, *Protostars and Planets VII*, ed. S. Inutsuka, Y. Aikawa, T. Muto, K. Tomida, & M. Tamura, 501, doi: [10.48550/arXiv.2203.09818](https://doi.org/10.48550/arXiv.2203.09818)
- Muzerolle, J., Calvet, N., & Hartmann, L. 1998a, *ApJ*, 492, 743, doi: [10.1086/305069](https://doi.org/10.1086/305069)
- . 2001, *ApJ*, 550, 944, doi: [10.1086/319779](https://doi.org/10.1086/319779)
- Muzerolle, J., Hartmann, L., & Calvet, N. 1998b, *AJ*, 116, 2965, doi: [10.1086/300636](https://doi.org/10.1086/300636)
- Natta, A., Testi, L., Muzerolle, J., et al. 2004, *A&A*, 424, 603, doi: [10.1051/0004-6361:20040356](https://doi.org/10.1051/0004-6361:20040356)
- Nelissen, M., Natta, A., McGinnis, P., et al. 2023, *A&A*, 677, A64, doi: [10.1051/0004-6361/202347231](https://doi.org/10.1051/0004-6361/202347231)
- Nguyen, D. C., Brandeker, A., van Kerkwijk, M. H., & Jayawardhana, R. 2012, *ApJ*, 745, 119, doi: [10.1088/0004-637X/745/2/119](https://doi.org/10.1088/0004-637X/745/2/119)
- Pepe, F., Cristiani, S., Rebolo, R., et al. 2021, *A&A*, 645, A96, doi: [10.1051/0004-6361/202038306](https://doi.org/10.1051/0004-6361/202038306)
- Pittman, C. V., Espaillet, C. C., Robinson, C. E., et al. 2022, *AJ*, 164, 201, doi: [10.3847/1538-3881/ac898d](https://doi.org/10.3847/1538-3881/ac898d)
- Robinson, C. E., & Espaillet, C. C. 2019, *ApJ*, 874, 129, doi: [10.3847/1538-4357/ab0d8d](https://doi.org/10.3847/1538-4357/ab0d8d)
- Roman-Duval, J., Proffitt, C. R., Taylor, J. M., et al. 2020, *Research Notes of the American Astronomical Society*, 4, 205, doi: [10.3847/2515-5172/abca2f](https://doi.org/10.3847/2515-5172/abca2f)
- Sabotta, S., Kabath, P., Korth, J., et al. 2019, *MNRAS*, 489, 2069, doi: [10.1093/mnras/stz2232](https://doi.org/10.1093/mnras/stz2232)
- Sicilia-Aguilar, A., Manara, C. F., de Boer, J., et al. 2020, *A&A*, 633, A37, doi: [10.1051/0004-6361/201936565](https://doi.org/10.1051/0004-6361/201936565)
- Siwak, M., Rucinski, S. M., Matthews, J. M., et al. 2014, *MNRAS*, 444, 327, doi: [10.1093/mnras/stu1304](https://doi.org/10.1093/mnras/stu1304)
- Siwak, M., Ogloza, W., Moffat, A. F. J., et al. 2018, *MNRAS*, 478, 758, doi: [10.1093/mnras/sty1220](https://doi.org/10.1093/mnras/sty1220)
- Soubiran, C., Jasniewicz, G., Chemin, L., et al. 2018, *A&A*, 616, A7, doi: [10.1051/0004-6361/201832795](https://doi.org/10.1051/0004-6361/201832795)
- Sousa, A. P., Bouvier, J., Alencar, S. H. P., et al. 2023, *A&A*, 670, A142, doi: [10.1051/0004-6361/202244720](https://doi.org/10.1051/0004-6361/202244720)
- Thanathibodee, T., Calvet, N., Muzerolle, J., et al. 2019, *ApJ*, 884, 86, doi: [10.3847/1538-4357/ab4127](https://doi.org/10.3847/1538-4357/ab4127)
- Thanathibodee, T., Molina, B., Serna, J., et al. 2023, *ApJ*, 944, 90, doi: [10.3847/1538-4357/acac84](https://doi.org/10.3847/1538-4357/acac84)
- Thanathibodee, T., Calvet, N., Herczeg, G., et al. 2018, *ApJ*, 861, 73, doi: [10.3847/1538-4357/aac5e9](https://doi.org/10.3847/1538-4357/aac5e9)
- Tokovinin, A., Fischer, D. A., Bonati, M., et al. 2013, *PASP*, 125, 1336, doi: [10.1086/674012](https://doi.org/10.1086/674012)



- van Dokkum, P. G. 2001, *PASP*, 113, 1420,  
doi: [10.1086/323894](https://doi.org/10.1086/323894)
- Venuti, L., Bouvier, J., Cody, A. M., et al. 2017, *A&A*, 599,  
A23, doi: [10.1051/0004-6361/201629537](https://doi.org/10.1051/0004-6361/201629537)
- Vernet, J., Dekker, H., D’Odorico, S., et al. 2011, *A&A*,  
536, A105, doi: [10.1051/0004-6361/201117752](https://doi.org/10.1051/0004-6361/201117752)
- Wendeborn, J., Espaillat, C. C., Lopez, S., et al. 2024a,  
arXiv e-prints, arXiv:2405.21038,  
doi: [10.48550/arXiv.2405.21038](https://doi.org/10.48550/arXiv.2405.21038)
- Wendeborn, J., Espaillat, C. C., Thanathibodee, T., et al.  
2024b, arXiv e-prints, arXiv:2405.21071,  
doi: [10.48550/arXiv.2405.21071](https://doi.org/10.48550/arXiv.2405.21071)
- Whittet, D. C. B., Shenoy, S. S., Clayton, G. C., &  
Gordon, K. D. 2004, *ApJ*, 602, 291, doi: [10.1086/380837](https://doi.org/10.1086/380837)
- Williams, J. P., & Cieza, L. A. 2011, *ARA&A*, 49, 67,  
doi: [10.1146/annurev-astro-081710-102548](https://doi.org/10.1146/annurev-astro-081710-102548)
- Zhu, Z., Stone, J. M., & Calvet, N. 2023, arXiv e-prints,  
arXiv:2309.15318, doi: [10.48550/arXiv.2309.15318](https://doi.org/10.48550/arXiv.2309.15318)
- . 2024, *MNRAS*, 528, 2883, doi: [10.1093/mnras/stad3712](https://doi.org/10.1093/mnras/stad3712)
- Zsidi, G., Manara, C. F., Kóspál, Á., et al. 2022, *A&A*, 660,  
A108, doi: [10.1051/0004-6361/202142203](https://doi.org/10.1051/0004-6361/202142203)

## APPENDIX

## A. FLOW MODEL RESULTS

Tables 5–8 present the results of our accretion flow modeling and optical veiling for TW Hya, RU Lup, BP Tau, and GM Aur.

**Table 5.** Accretion flow model results and veilings for TW Hya

Object	MJD	Instrument	$r_V$	$\dot{M}$ [ $10^8 M_{\odot} \text{yr}^{-1}$ ]	$R_{in}$ [ $R_{\star}$ ]	$W_r$ [ $R_{\star}$ ]	$T_{max}$ [K]	Incl. [ $^{\circ}$ ]	MAPE
TW Hya	59241.30	C	0.23±0.01	0.4±0.2	2.7±0.2	0.2±0.1	9195.1±902.1	15.7±6.0	0.11
TW Hya	59280.17	C	0.64±0.03	0.3±0.1	3.6±0.3	0.4±0.2	9606.3±820.1	16.7±5.9	0.14
TW Hya	59280.29	E	0.42±0.02	0.4±0.1	3.9±0.3	0.4±0.2	9216.2±864.9	16.6±5.8	0.12
TW Hya	59281.18	C	0.58±0.03	0.3±0.1	4.2±0.3	0.4±0.3	9352.1±876.4	17.4±5.7	0.14
TW Hya	59282.23	C	0.28±0.01	0.3±0.2	3.5±0.4	0.2±0.2	8666.6±778.4	16.7±5.9	0.11
TW Hya	59284.24	C	0.62±0.03	0.3±0.1	4.0±0.3	0.5±0.3	9567.3±844.5	17.3±5.8	0.10
TW Hya	59286.26	C	0.23±0.01	0.3±0.2	3.4±0.5	0.12±0.07	8596.7±894.3	15.6±6.0	0.13
TW Hya	59288.25	C	0.70±0.04	0.4±0.2	4.4±0.3	0.3±0.2	8793.6±718.3	16.9±5.8	0.10
TW Hya	59291.18	C	0.45±0.02	0.3±0.2	4.2±0.4	0.2±0.2	8605.1±771.2	16.8±5.8	0.11
TW Hya	59294.17	C	0.37±0.02	0.3±0.1	3.7±0.3	0.4±0.2	9382.7±857.5	16.1±5.9	0.10
TW Hya	59295.20	C	0.64±0.03	0.3±0.1	4.4±0.3	0.4±0.2	9017.4±798.3	17.2±5.7	0.09
TW Hya	59296.18	C	1.12±0.06	0.4±0.1	4.8±0.4	0.5±0.3	9085.1±687.2	18.6±5.1	0.12
TW Hya	59298.15	C	0.61±0.03	0.3±0.1	3.8±0.3	0.4±0.2	9477.4±848.3	16.1±6.0	0.12
TW Hya	59300.11	C	0.40±0.02	0.4±0.1	2.6±0.2	0.2±0.2	9395.9±781.8	16.6±5.8	0.23
TW Hya	59302.13	C	0.41±0.02	0.4±0.2	3.0±0.3	0.2±0.2	9015.0±845.9	17.1±5.7	0.15
TW Hya	59303.12	C	0.29±0.01	0.4±0.2	3.9±0.3	0.2±0.2	8660.8±710.7	16.6±5.9	0.15
TW Hya	59304.16	C	0.69±0.03	0.4±0.1	3.4±0.3	0.4±0.2	9679.0±759.0	16.1±6.0	0.18
TW Hya	59305.12	C	0.44±0.02	0.4±0.2	4.3±0.4	0.2±0.1	8660.1±749.9	16.3±6.0	0.13
TW Hya	59306.15	C	0.42±0.02	0.4±0.2	4.7±0.3	0.2±0.2	8582.3±729.0	16.6±6.0	0.13
TW Hya	59307.00	X	0.51±0.03	0.26±0.04	4.4±0.3	0.9±0.4	10109.9±544.8	13.2±5.8	0.14
TW Hya	59307.16	C	0.88±0.04	0.4±0.1	4.0±0.3	0.2±0.2	8867.1±674.1	17.2±5.7	0.14
TW Hya	59308.04	E	0.49±0.02	0.4±0.1	3.9±0.3	0.3±0.2	9218.4±747.2	16.6±5.9	0.13
TW Hya	59308.13	C	0.64±0.03	0.4±0.1	3.7±0.2	0.4±0.2	9433.1±774.4	16.0±6.0	0.13
TW Hya	59309.14	C	1.16±0.06	0.4±0.1	4.1±0.3	0.4±0.2	9223.7±660.3	17.4±5.7	0.13
TW Hya	59309.14	E	0.97±0.05	0.4±0.1	4.3±0.3	0.3±0.2	9052.6±579.9	16.8±5.9	0.13
TW Hya	59310.09	E	1.01±0.05	0.4±0.1	4.4±0.4	0.3±0.2	9045.6±625.5	17.4±5.7	0.17
TW Hya	59310.13	C	1.14±0.06	0.4±0.1	4.3±0.4	0.3±0.2	9049.8±651.7	17.7±5.7	0.17
TW Hya	59310.15	X	0.91±0.07	0.29±0.04	4.4±0.3	0.8±0.3	10197.8±490.2	13.3±5.6	0.18
TW Hya	59311.14	C	0.28±0.01	0.5±0.1	3.0±0.3	0.3±0.2	9344.9±759.8	15.7±5.9	0.23
TW Hya	59312.16	C	0.29±0.01	0.4±0.2	3.3±0.4	0.2±0.2	8818.2±773.3	17.5±5.7	0.18
TW Hya	59313.15	C	0.24±0.01	0.3±0.2	2.9±0.3	0.2±0.1	9090.8±918.8	16.9±5.6	0.13
TW Hya	59313.22	E	0.12±0.01	0.3±0.2	3.1±0.3	0.2±0.2	9184.6±933.3	16.6±5.7	0.13
TW Hya	59314.23	C	0.31±0.02	0.3±0.1	3.1±0.3	0.3±0.2	9310.3±883.3	16.8±5.7	0.14
TW Hya	59653.15	C	0.46±0.02	0.5±0.1	3.9±0.3	0.2±0.2	9194.1±665.5	16.6±5.9	0.16
TW Hya	59654.15	C	0.34±0.02	0.5±0.1	4.6±0.5	0.2±0.1	8918.2±412.8	16.0±6.0	0.16
TW Hya	59655.22	C	1.04±0.05	0.5±0.1	4.0±0.3	0.4±0.2	9203.6±657.1	18.1±5.4	0.13

Table 5 continued

Table 5 (continued)

Object	MJD	Instrument	$r_V$	$\dot{M}$ [ $10^8 M_{\odot} \text{yr}^{-1}$ ]	$R_{in}$ [ $R_{\star}$ ]	$W_r$ [ $R_{\star}$ ]	$T_{max}$ [K]	Incl. [ $^{\circ}$ ]	MAPE
TW Hya	59656.17	C	1.07±0.05	0.6±0.1	3.5±0.2	0.4±0.2	9515.0±750.6	16.6±5.8	0.14
TW Hya	59657.21	C	0.73±0.04	0.56±0.09	3.8±0.2	0.4±0.2	9367.1±693.1	17.5±5.7	0.16
TW Hya	59658.19	C	0.58±0.03	0.4±0.1	3.1±0.2	0.3±0.2	9503.4±766.7	16.0±6.0	0.11
TW Hya	59659.20	C	0.88±0.04	0.52±0.09	4.2±0.3	0.4±0.2	9290.4±653.3	19.1±4.9	0.15
TW Hya	59660.15	C	1.02±0.05	0.5±0.1	3.9±0.3	0.3±0.2	9088.7±607.6	17.6±5.7	0.14
TW Hya	59661.22	C	0.49±0.02	0.5±0.1	3.5±0.2	0.3±0.2	9276.8±694.3	16.4±6.0	0.15
TW Hya	59662.16	C	0.77±0.04	0.4±0.1	3.1±0.2	0.3±0.2	9513.3±756.8	16.8±5.8	0.13
TW Hya	59663.18	C	0.60±0.03	0.4±0.1	2.9±0.2	0.3±0.1	9591.7±764.5	16.4±5.8	0.14
TW Hya	59664.14	C	0.52±0.03	0.4±0.1	2.8±0.2	0.2±0.2	9429.6±762.2	16.3±5.9	0.15
TW Hya	59665.16	C	0.53±0.03	0.4±0.1	3.6±0.3	0.4±0.2	9296.4±714.5	16.4±5.9	0.12
TW Hya	59666.19	C	1.19±0.06	0.53±0.09	3.9±0.2	0.4±0.2	9479.2±661.4	17.9±5.3	0.13
TW Hya	59667.14	C	0.77±0.04	0.5±0.1	3.1±0.2	0.3±0.1	9556.4±747.5	17.9±5.5	0.20
TW Hya	59668.14	C	0.54±0.03	0.4±0.1	4.0±0.4	0.2±0.1	8979.4±654.9	17.5±5.8	0.21
TW Hya	59670.10	C	1.44±0.07	0.6±0.1	3.3±0.2	0.3±0.1	9637.4±717.0	17.4±5.8	0.17
TW Hya	59671.06	C	0.65±0.03	0.6±0.1	3.2±0.2	0.3±0.1	9628.3±719.1	16.8±5.9	0.18
TW Hya	59672.01	C	0.43±0.02	0.5±0.1	3.1±0.2	0.3±0.2	9476.3±719.7	16.8±6.0	0.16
TW Hya	59672.26	C	0.44±0.02	0.6±0.1	3.2±0.2	0.3±0.1	9619.7±711.1	16.9±6.0	0.16
TW Hya	59673.13	C	1.02±0.05	0.5±0.1	3.1±0.2	0.2±0.2	9319.3±702.7	16.1±6.1	0.15
TW Hya	59674.14	C	0.98±0.05	0.61±0.07	3.8±0.3	0.3±0.1	9609.0±658.4	18.0±5.3	0.17
TW Hya	59675.09	C	0.73±0.04	0.6±0.1	3.2±0.2	0.3±0.2	9605.5±725.2	16.4±6.1	0.14
TW Hya	59676.01	C	1.07±0.05	0.58±0.08	3.7±0.2	0.4±0.2	9728.1±681.0	17.5±5.5	0.16
TW Hya	59676.23	C	1.21±0.06	0.57±0.09	3.8±0.2	0.4±0.2	9563.5±742.5	17.9±5.3	0.16
TW Hya	59677.07	C	1.31±0.07	0.5±0.1	3.6±0.2	0.3±0.2	9428.3±723.9	17.2±5.6	0.17
TW Hya	59678.01	C	0.82±0.04	0.5±0.1	3.0±0.2	0.2±0.2	9360.5±760.0	15.9±5.9	0.15
TW Hya	59678.18	C	0.56±0.03	0.5±0.1	3.0±0.3	0.2±0.1	9355.3±762.9	16.2±6.0	0.14
TW Hya	59679.05	C	0.89±0.04	0.6±0.1	3.6±0.2	0.4±0.2	9664.7±719.7	16.4±5.9	0.18
TW Hya	59680.07	C	0.99±0.05	0.59±0.09	3.3±0.2	0.4±0.1	9980.8±633.8	16.4±6.0	0.18
TW Hya	59682.09	C	1.16±0.06	0.6±0.1	3.6±0.2	0.3±0.2	9693.3±724.6	16.1±5.8	0.19
TW Hya	59684.15	C	1.03±0.05	0.5±0.1	3.4±0.2	0.4±0.2	9691.6±702.9	15.9±6.0	0.19
TW Hya	59686.12	C	0.73±0.04	0.52±0.09	3.9±0.3	0.4±0.2	9609.6±729.2	17.0±5.8	0.16
TW Hya	59688.09	C	0.95±0.05	0.5±0.1	4.6±0.4	0.11±0.06	8936.7±533.5	16.2±6.1	0.14
TW Hya	59690.06	C	0.93±0.05	0.4±0.1	3.7±0.3	0.4±0.2	9564.6±785.0	16.1±6.0	0.15
TW Hya	59692.07	C	0.97±0.05	0.4±0.1	3.3±0.2	0.4±0.2	9724.5±735.1	16.2±6.0	0.15
TW Hya	59694.03	C	1.83±0.09	0.4±0.1	3.4±0.2	0.4±0.2	9707.3±733.7	16.0±6.0	0.14
TW Hya	59695.05	C	0.98±0.05	0.4±0.1	3.8±0.3	0.5±0.2	9662.6±830.9	15.0±6.0	0.13
TW Hya	59696.18	C	0.87±0.04	0.4±0.1	4.5±0.3	0.4±0.2	9108.0±787.3	16.7±5.9	0.08
TW Hya	59696.24	C	0.76±0.04	0.4±0.1	4.4±0.3	0.4±0.2	9064.6±814.4	16.2±6.0	0.08
TW Hya	59697.15	C	0.65±0.03	0.4±0.2	3.7±0.3	0.3±0.2	9263.3±910.5	15.6±5.8	0.09
TW Hya	59698.14	C	1.24±0.06	0.4±0.1	3.7±0.2	0.4±0.2	9594.0±787.8	15.9±5.9	0.09

NOTE—Instrument names are abbreviated as: C: CHIRON, E: ESPRESSO, X: XSHOOTER, S: SOPHIE, U: UVES, T: TCES

**Table 6.** Accretion flow model results for RU Lup

Object	MJD	Instrument	$\dot{M}$ [ $10^8 M_{\odot}\text{yr}^{-1}$ ]	$R_{in}$ [ $R_{\star}$ ]	$W_r$ [ $R_{\star}$ ]	$T_{max}$ [K]	Incl. [ $^{\circ}$ ]	MAPE
RU Lup	59264.37	C	8.3±4.0	3.4±0.3	0.6±0.3	7368.8±343.6	20.4±4.1	0.16
RU Lup	59318.26	C	8.2±4.1	3.3±0.3	0.6±0.3	7336.0±337.1	20.3±4.1	0.20
RU Lup	59395.05	C	8.2±4.0	3.7±0.3	0.7±0.4	7434.5±350.3	20.5±4.1	0.16
RU Lup	59434.99	C	7.8±4.1	3.5±0.3	0.8±0.4	7477.3±395.1	20.5±4.1	0.13
RU Lup	59435.98	C	7.9±4.1	3.5±0.3	0.8±0.4	7468.7±387.1	20.4±4.1	0.14
RU Lup	59436.10	X	7.6±4.1	3.7±0.3	0.8±0.5	7467.8±429.2	20.9±4.0	0.14
RU Lup	59437.00	C	7.8±4.0	3.4±0.3	0.8±0.4	7482.0±380.8	20.4±4.1	0.14
RU Lup	59437.97	C	8.1±4.0	3.5±0.3	0.7±0.4	7450.0±358.0	20.4±4.1	0.16
RU Lup	59439.02	C	8.0±4.0	3.2±0.3	0.7±0.4	7483.2±395.2	20.5±4.1	0.13
RU Lup	59439.99	C	7.7±4.1	3.5±0.3	0.9±0.5	7551.5±410.7	20.6±4.1	0.14
RU Lup	59442.03	C	8.1±4.1	3.6±0.3	0.7±0.4	7425.3±359.5	20.5±4.1	0.15
RU Lup	59443.02	C	8.0±4.0	3.3±0.3	0.7±0.4	7464.7±377.2	20.2±4.1	0.14
RU Lup	59443.14	C	8.1±4.1	3.1±0.3	0.7±0.4	7443.3±371.7	20.3±4.1	0.15
RU Lup	59444.02	C	8.1±4.0	3.4±0.3	0.7±0.4	7415.9±356.2	20.5±4.1	0.16
RU Lup	59444.03	C	8.1±4.0	3.4±0.3	0.7±0.4	7438.4±365.9	20.6±4.1	0.15
RU Lup	59447.02	C	8.0±4.1	2.7±0.2	0.6±0.3	7719.6±552.8	20.2±4.0	0.17
RU Lup	59447.05	C	7.9±4.0	3.2±0.2	0.8±0.4	7581.4±405.1	20.2±4.1	0.15
RU Lup	59448.00	C	8.0±4.0	3.8±0.2	0.7±0.3	7523.0±363.4	20.4±4.1	0.16
RU Lup	59448.07	X	7.8±4.0	3.7±0.3	0.7±0.4	7478.7±364.2	20.2±4.0	0.20
RU Lup	59449.00	E	8.2±4.1	3.9±0.3	0.6±0.3	7381.6±345.2	20.5±4.1	0.18
RU Lup	59449.04	C	8.2±4.0	3.8±0.3	0.7±0.3	7385.6±335.1	20.6±4.0	0.18
RU Lup	59449.98	C	8.3±4.1	3.7±0.3	0.6±0.3	7362.8±341.5	20.5±4.1	0.17
RU Lup	59453.01	C	8.0±4.1	3.2±0.3	0.7±0.4	7429.6±372.3	20.3±4.1	0.14
RU Lup	59458.02	E	7.9±4.0	3.2±0.3	0.7±0.4	7537.0±386.3	20.4±4.1	0.13
RU Lup	59458.06	E	8.0±4.0	3.1±0.3	0.7±0.4	7524.6±396.0	20.4±4.1	0.13
RU Lup	59676.20	C	8.0±4.1	3.6±0.3	0.7±0.4	7384.6±356.1	20.4±4.0	0.15
RU Lup	59683.17	C	8.1±4.0	3.4±0.3	0.8±0.4	7407.1±372.0	20.5±4.1	0.15
RU Lup	59690.25	C	8.0±4.1	3.4±0.3	0.7±0.4	7436.9±373.7	20.3±4.1	0.15
RU Lup	59699.19	C	8.2±4.0	3.3±0.3	0.7±0.4	7407.6±348.0	20.3±4.1	0.15
RU Lup	59715.17	C	8.1±4.1	3.5±0.3	0.7±0.4	7418.0±356.7	20.5±4.1	0.16
RU Lup	59723.14	C	8.0±4.0	3.1±0.2	0.7±0.4	7495.1±384.0	20.5±4.1	0.15
RU Lup	59736.11	C	7.8±4.0	3.7±0.2	0.8±0.4	7538.9±379.5	20.6±4.1	0.16
RU Lup	59790.11	C	7.9±4.0	3.6±0.3	0.9±0.4	7565.2±396.6	20.6±4.1	0.14
RU Lup	59799.03	C	7.9±4.0	3.5±0.2	0.8±0.4	7550.9±395.1	20.5±4.1	0.15
RU Lup	59800.03	C	8.2±4.0	3.7±0.3	0.7±0.4	7434.4±355.0	20.7±4.0	0.16
RU Lup	59801.00	C	7.9±4.0	3.7±0.2	0.8±0.4	7537.4±374.4	20.6±4.0	0.17
RU Lup	59801.05	E	7.8±4.0	3.6±0.2	0.8±0.4	7524.4±371.7	20.6±4.0	0.17
RU Lup	59801.98	C	8.0±4.0	3.8±0.3	0.7±0.4	7477.8±362.6	20.7±4.0	0.16
RU Lup	59802.07	E	8.0±4.0	3.8±0.3	0.8±0.4	7487.0±372.8	20.6±4.0	0.16
RU Lup	59802.97	C	8.1±4.1	3.4±0.3	0.7±0.4	7451.8±359.2	20.7±4.1	0.16
RU Lup	59804.00	C	8.1±4.1	3.8±0.3	0.6±0.3	7349.0±354.2	20.6±4.1	0.16
RU Lup	59804.10	E	8.0±4.0	3.8±0.3	0.6±0.3	7337.4±345.7	20.7±4.0	0.17
RU Lup	59805.06	C	8.0±4.0	3.6±0.3	0.7±0.4	7469.4±370.3	20.6±4.0	0.15
RU Lup	59806.00	C	8.0±4.0	3.8±0.3	0.7±0.4	7469.5±365.0	20.7±4.0	0.15
RU Lup	59807.00	C	8.2±4.1	3.6±0.3	0.6±0.3	7362.5±340.2	20.7±4.0	0.17

Table 6 continued

**Table 6** (*continued*)

Object	MJD	Instrument	$\dot{M}$	$R_{in}$	$W_r$	$T_{max}$	Incl.	MAPE
			[ $10^8 M_{\odot} \text{yr}^{-1}$ ]	[ $R_{\star}$ ]	[ $R_{\star}$ ]	[K]	[ $^{\circ}$ ]	
RU Lup	59807.10	E	8.2±4.1	3.6±0.3	0.6±0.3	7367.3±344.6	20.7±4.0	0.16
RU Lup	59808.05	C	8.2±4.1	3.7±0.3	0.7±0.4	7376.8±356.0	20.8±4.0	0.16
RU Lup	59809.07	C	8.2±4.0	3.4±0.3	0.7±0.3	7401.8±353.1	20.7±4.1	0.16
RU Lup	59810.03	C	8.1±4.1	3.3±0.3	0.7±0.4	7374.9±363.8	20.7±4.1	0.16
RU Lup	59811.05	C	8.1±4.1	3.4±0.3	0.7±0.4	7467.2±364.8	20.5±4.1	0.15
RU Lup	59812.02	C	8.0±3.9	3.3±0.3	0.7±0.4	7520.5±367.2	20.6±4.1	0.15
RU Lup	59813.05	C	8.2±4.0	3.8±0.3	0.7±0.3	7372.6±344.2	20.7±4.0	0.19
RU Lup	59814.00	C	8.0±4.1	3.5±0.3	0.7±0.4	7437.7±363.7	20.7±4.1	0.16
RU Lup	59814.04	E	8.1±4.1	3.5±0.3	0.7±0.4	7413.8±360.2	20.6±4.0	0.17
RU Lup	59815.05	C	7.9±4.0	3.4±0.3	0.8±0.4	7502.5±367.8	20.7±4.1	0.17
RU Lup	59816.02	C	8.2±4.0	3.8±0.3	0.7±0.4	7426.4±337.3	20.6±4.0	0.17
RU Lup	59817.04	C	8.1±4.0	3.9±0.3	0.7±0.3	7482.1±350.2	20.7±4.0	0.19

NOTE—Instrument names are abbreviated as: C: CHIRON, E: ESPRESSO, X: XSHOOTER, S: SOPHIE, U: UVES, T: TCES

**Table 7.** Accretion flow model results and veilings for BP Tau

Object	MJD	Instrument	$r_V$	$\dot{M}$	$R_{in}$	$W_r$	$T_{max}$	Incl.	MAPE
				[ $10^8 M_{\odot} \text{yr}^{-1}$ ]	[ $R_{\star}$ ]	[ $R_{\star}$ ]	[K]	[ $^{\circ}$ ]	
BP Tau	59448.39	X	0.81±0.04	2.1±1.6	3.6±0.4	0.7±0.4	8181.4±819.5	44.7±6.8	0.13
BP Tau	59452.35	X	1.27±0.06	1.8±1.6	3.7±0.4	0.8±0.5	8311.2±913.6	45.5±6.5	0.11
BP Tau	59459.38	E	1.30±0.06	2.2±1.7	3.6±0.4	0.6±0.4	8195.0±821.8	43.0±7.5	0.13
BP Tau	59460.37	X	1.87±0.22	1.8±1.4	3.8±0.4	1.3±0.5	8512.9±783.3	45.0±6.5	0.11
BP Tau	59464.36	E	0.69±0.03	2.1±1.7	3.4±0.4	0.5±0.4	8087.9±919.2	42.6±7.4	0.13
BP Tau	59467.38	C	0.75±0.04	2.1±1.8	3.3±0.4	0.4±0.3	8035.9±899.1	42.2±7.6	0.14
BP Tau	59470.38	C	0.57±0.03	2.0±1.7	3.4±0.4	0.5±0.4	8165.6±925.4	42.9±7.3	0.14
BP Tau	59845.35	C	0.92±0.05	2.0±1.7	3.2±0.4	0.7±0.5	8266.1±900.4	44.8±6.6	0.11
BP Tau	59859.33	C	0.73±0.04	2.2±1.8	3.4±0.4	0.7±0.5	8134.4±866.9	45.8±6.4	0.11
BP Tau	59863.31	C	0.64±0.03	2.3±1.8	4.1±0.6	1.1±0.6	8035.8±782.3	46.4±6.0	0.11
BP Tau	59868.29	C	0.66±0.03	2.2±1.8	3.1±0.4	0.4±0.3	7998.3±847.8	43.7±7.2	0.11
BP Tau	59882.25	C	0.71±0.04	2.4±1.9	2.8±0.3	0.3±0.3	7881.4±842.4	41.8±7.5	0.14
BP Tau	59893.21	C	0.81±0.04	2.3±1.8	2.4±0.3	0.3±0.3	7860.0±850.6	42.3±7.7	0.09
BP Tau	59898.19	C	0.75±0.04	2.4±1.8	3.0±0.3	0.6±0.4	8058.6±862.5	45.1±6.6	0.11
BP Tau	59907.19	C	1.20±0.06	2.2±1.8	2.9±0.3	0.5±0.4	8084.9±878.4	42.2±7.4	0.14
BP Tau	59909.17	C	0.91±0.05	2.4±1.8	2.8±0.3	0.4±0.3	7949.8±842.6	43.2±7.1	0.11
BP Tau	59910.17	C	1.01±0.05	2.4±1.7	2.7±0.3	0.5±0.3	8087.6±785.0	41.5±7.5	0.13
BP Tau	59911.18	C	1.04±0.05	2.1±1.7	3.1±0.3	0.7±0.5	8232.7±845.4	44.0±7.0	0.13
BP Tau	59912.15	C	1.00±0.05	2.2±1.8	3.1±0.3	0.6±0.4	8145.1±860.1	43.7±7.0	0.11
BP Tau	59913.17	C	1.05±0.05	2.2±1.6	3.4±0.4	1.0±0.5	8289.3±774.4	46.9±5.3	0.11
BP Tau	59914.18	C	0.70±0.04	2.2±1.7	3.3±0.4	0.8±0.5	8188.4±870.7	45.7±6.3	0.11
BP Tau	59915.18	C	0.80±0.04	2.1±1.8	3.1±0.3	0.6±0.4	8194.3±922.6	42.6±7.5	0.14

**Table 7** *continued*



**Table 7** (*continued*)

Object	MJD	Instrument	$r_V$	$\dot{M}$	$R_{in}$	$W_r$	$T_{max}$	Incl.	MAPE
				$[10^8 M_{\odot} \text{yr}^{-1}]$	$[R_{\star}]$	$[R_{\star}]$	$[K]$	$[\circ]$	
BP Tau	59916.19	C	0.61±0.03	2.4±1.8	2.7±0.3	0.5±0.4	8007.4±829.9	42.9±7.3	0.14
BP Tau	59917.16	C	0.94±0.05	2.5±1.8	2.8±0.3	0.4±0.3	7966.7±822.2	40.5±7.5	0.15
BP Tau	59918.16	C	0.94±0.05	2.2±1.8	2.9±0.3	0.5±0.4	8137.9±889.5	41.4±7.5	0.12
BP Tau	59919.15	C	1.33±0.07	2.2±1.5	3.0±0.3	1.0±0.6	8416.5±771.9	43.2±7.0	0.13
BP Tau	59922.14	C	1.04±0.05	2.4±1.8	2.8±0.3	0.5±0.4	8035.6±809.6	42.9±7.2	0.10
BP Tau	59925.16	C	0.75±0.04	2.3±1.8	2.7±0.3	0.4±0.3	7957.2±866.6	41.2±7.5	0.13
BP Tau	59926.14	C	0.78±0.04	2.4±1.8	3.0±0.3	0.5±0.3	8050.8±813.9	41.7±7.4	0.12
BP Tau	59927.15	C	1.13±0.06	2.3±1.6	3.1±0.3	0.6±0.4	8126.2±767.3	43.8±7.2	0.12
BP Tau	59928.11	E	0.59±0.03	2.1±1.6	3.2±0.3	1.1±0.6	8408.5±802.9	45.1±6.4	0.10
BP Tau	59928.13	C	0.76±0.04	2.1±1.6	3.1±0.3	1.0±0.6	8359.5±860.2	44.8±6.7	0.10
BP Tau	59929.14	C	0.67±0.03	2.1±1.7	3.2±0.5	1.0±0.6	8291.1±900.4	45.3±6.3	0.10
BP Tau	59930.07	E	0.42±0.02	2.1±1.7	3.2±0.4	1.0±0.6	8278.4±894.6	44.6±6.8	0.09
BP Tau	59930.13	C	0.61±0.03	2.0±1.7	3.1±0.4	0.8±0.5	8201.3±922.6	44.3±7.1	0.09
BP Tau	59931.13	C	0.67±0.03	2.3±1.8	3.0±0.4	0.5±0.4	8028.5±892.2	44.4±7.0	0.12
BP Tau	59932.13	C	0.66±0.03	2.1±1.6	2.9±0.3	0.9±0.6	8335.7±840.9	45.2±6.3	0.12
BP Tau	59933.13	C	0.55±0.03	2.2±1.8	2.9±0.3	0.7±0.5	8206.4±931.8	44.3±6.8	0.12
BP Tau	59933.17	E	0.40±0.02	2.2±1.8	3.0±0.3	0.7±0.6	8252.3±905.3	45.1±6.5	0.12
BP Tau	59934.07	E	0.42±0.02	2.4±1.9	3.0±0.3	0.4±0.3	7892.1±869.7	42.4±7.5	0.11
BP Tau	59934.12	C	0.55±0.03	2.4±1.9	2.9±0.3	0.3±0.2	7842.1±842.6	41.8±7.5	0.12
BP Tau	59935.11	C	0.51±0.03	2.4±1.8	2.9±0.3	0.3±0.3	7885.2±851.5	42.1±7.5	0.12
BP Tau	59936.08	E	0.76±0.04	2.1±1.6	3.2±0.3	0.7±0.5	8227.9±851.6	43.2±7.3	0.11
BP Tau	59936.11	C	0.93±0.05	2.1±1.8	3.1±0.3	0.6±0.4	8138.8±889.2	42.8±7.5	0.11
BP Tau	59937.12	C	0.97±0.05	2.0±1.7	3.0±0.4	0.7±0.5	8156.8±910.0	42.5±7.4	0.08
BP Tau	59938.12	C	0.76±0.04	2.1±1.7	3.0±0.4	0.6±0.4	8080.4±871.4	44.4±6.9	0.10
BP Tau	59939.11	C	0.68±0.03	2.2±1.7	2.7±0.3	0.5±0.4	8028.8±926.5	42.8±7.5	0.09
BP Tau	59940.11	C	0.68±0.03	1.9±1.6	2.8±0.3	0.9±0.6	8400.3±901.7	43.1±7.3	0.10
BP Tau	59941.13	C	0.69±0.03	2.2±1.7	2.7±0.3	0.7±0.5	8173.9±857.2	44.7±6.5	0.11
BP Tau	59949.08	C	0.86±0.04	2.1±1.6	3.1±0.4	0.7±0.5	8207.5±854.7	45.7±6.4	0.13
BP Tau	59950.08	C	1.12±0.06	2.3±1.7	3.1±0.3	0.6±0.4	8105.3±762.3	45.0±6.7	0.14
BP Tau	59951.08	C	1.11±0.06	2.3±1.8	3.0±0.3	0.6±0.4	8087.0±800.9	44.7±6.7	0.12
BP Tau	59952.08	C	1.10±0.06	2.2±1.7	3.1±0.4	0.7±0.5	8137.3±847.8	45.1±6.4	0.10
BP Tau	59953.07	C	1.38±0.07	2.2±1.7	3.2±0.4	0.8±0.4	8160.0±780.1	45.1±6.8	0.12

NOTE—Instrument names are abbreviated as: C: CHIRON, E: ESPRESSO, X: XSHOOTER, S: SOPHIE, U: UVES, T: TCES

**Table 8.** Accretion flow model results and veilings for GM Aur

Object	MJD	Instrument	$r_V$	$\dot{M}$	$R_{in}$	$W_r$	$T_{max}$	Incl.	MAPE
				$[10^8 M_{\odot} \text{yr}^{-1}]$	$[R_{\star}]$	$[R_{\star}]$	$[K]$	$[\circ]$	
GM Aur	59498.99	S	0.30±0.03	1.3±1.0	3.2±0.2	0.3±0.1	9891.0±1085.9	53.1±5.8	0.14
GM Aur	59499.98	S	0.17±0.02	1.3±0.9	3.1±0.2	0.2±0.1	9901.8±1057.6	51.8±6.0	0.13
GM Aur	59501.13	S	0.27±0.03	1.5±1.1	3.2±0.2	0.3±0.2	9674.5±1130.9	55.3±5.7	0.13

**Table 8** *continued*

Table 8 (continued)

Object	MJD	Instrument	$r_V$	$\dot{M}$ [ $10^8 M_{\odot} \text{yr}^{-1}$ ]	$R_{in}$ [ $R_{\star}$ ]	$W_r$ [ $R_{\star}$ ]	$T_{max}$ [K]	Incl. [ $^{\circ}$ ]	MAPE
GM Aur	59502.03	S	0.35±0.04	1.1±0.9	3.1±0.3	0.3±0.1	9784.0±1063.2	54.3±5.8	0.12
GM Aur	59502.96	T	0.50±0.05	0.9±0.8	3.2±0.4	0.4±0.1	9465.4±1088.5	55.5±4.8	0.13
GM Aur	59503.11	S	0.31±0.03	0.9±0.6	3.2±0.3	0.3±0.1	9896.9±1041.6	50.8±5.4	0.12
GM Aur	59504.08	S	0.18±0.02	1.0±0.8	3.5±0.3	0.4±0.1	9690.5±1045.8	55.4±5.1	0.11
GM Aur	59504.34	X	0.47±0.05	0.8±0.5	4.1±0.3	1.1±0.5	9913.5±913.6	54.5±4.3	0.09
GM Aur	59505.02	S	0.17±0.02	1.2±0.9	3.2±0.2	0.3±0.1	9940.1±1070.1	53.6±5.7	0.12
GM Aur	59505.11	T	0.29±0.03	1.2±1.0	2.9±0.2	0.3±0.2	9710.6±1092.8	54.8±5.5	0.13
GM Aur	59505.96	S	0.29±0.03	1.5±1.1	3.3±0.2	0.3±0.2	9746.0±1075.8	52.4±6.0	0.12
GM Aur	59507.09	T	0.63±0.06	2.0±1.4	2.7±0.3	0.7±0.4	9219.0±1089.1	58.9±4.0	0.12
GM Aur	59509.23	E	0.83±0.08	1.3±0.9	3.7±0.3	0.4±0.1	9850.0±1084.4	52.0±5.6	0.13
GM Aur	59510.04	S	0.41±0.04	1.1±0.7	3.6±0.3	0.4±0.1	9904.6±1030.3	52.6±5.8	0.13
GM Aur	59510.09	T	0.60±0.06	1.0±0.9	3.5±0.3	0.4±0.1	9575.9±1066.4	56.9±4.7	0.14
GM Aur	59510.14	T	0.60±0.06	1.0±0.8	3.5±0.3	0.4±0.1	9610.6±1042.8	56.9±4.7	0.14
GM Aur	59510.97	T	0.38±0.04	1.1±0.9	3.4±0.3	0.4±0.1	9642.8±1066.4	55.8±5.1	0.15
GM Aur	59511.00	S	0.25±0.02	1.2±0.9	3.5±0.3	0.3±0.1	9864.2±1063.5	52.6±5.7	0.13
GM Aur	59511.01	T	0.38±0.04	1.1±0.8	3.3±0.3	0.4±0.1	9708.8±1056.8	55.5±5.3	0.15
GM Aur	59511.97	T	0.32±0.03	0.9±0.7	2.9±0.2	0.2±0.1	9633.4±1034.7	52.5±6.0	0.12
GM Aur	59511.99	S	0.23±0.02	0.9±0.7	2.9±0.2	0.2±0.1	9908.1±995.4	51.7±5.8	0.10
GM Aur	59512.01	T	0.31±0.03	0.9±0.7	2.8±0.3	0.2±0.1	9684.6±1058.1	52.4±6.3	0.13
GM Aur	59513.03	T	0.44±0.04	1.1±0.9	2.9±0.2	0.2±0.1	9674.9±1038.3	54.3±6.0	0.14
GM Aur	59513.08	T	0.49±0.05	1.1±0.8	2.6±0.2	0.2±0.1	9836.4±1090.8	52.2±6.4	0.13
GM Aur	59513.10	S	0.31±0.03	1.2±0.9	3.2±0.2	0.2±0.1	9884.9±1031.3	53.7±6.1	0.13
GM Aur	59514.07	S	0.45±0.05	1.0±0.7	3.0±0.2	0.2±0.1	10071.8±990.7	51.1±5.6	0.13
GM Aur	59515.04	T	0.42±0.04	0.8±0.7	3.0±0.3	0.2±0.1	9714.5±1070.3	51.4±5.4	0.15
GM Aur	59515.08	T	0.39±0.04	0.7±0.7	2.9±0.3	0.2±0.1	9679.2±1068.5	51.3±5.4	0.15
GM Aur	59515.09	S	0.27±0.03	0.8±0.6	2.9±0.2	0.2±0.1	9938.5±1043.4	49.3±5.2	0.13
GM Aur	59516.01	S	0.21±0.02	0.8±0.6	2.8±0.2	0.2±0.1	9943.8±1021.7	49.5±5.2	0.14
GM Aur	59553.13	E	0.19±0.02	0.9±0.7	2.9±0.2	0.2±0.1	9828.5±1033.0	51.2±5.4	0.11
GM Aur	59554.17	E	0.24±0.02	1.0±0.7	3.0±0.2	0.16±0.09	10057.2±1004.7	51.5±5.7	0.11
GM Aur	59555.19	E	0.58±0.06	1.1±0.8	3.0±0.2	0.2±0.1	9935.9±1041.7	52.2±5.9	0.12
GM Aur	59556.15	X	0.84±0.08	0.6±0.2	3.7±0.4	0.4±0.2	10276.0±862.1	45.6±3.0	0.10
GM Aur	59556.19	E	0.55±0.05	1.0±0.7	3.2±0.3	0.2±0.1	9863.9±1061.7	51.6±5.8	0.11
GM Aur	59558.86	T	0.30±0.03	0.9±0.8	2.9±0.3	0.2±0.1	9603.7±1101.6	52.5±6.0	0.13
GM Aur	59558.90	T	0.30±0.03	0.8±0.8	2.8±0.3	0.2±0.1	9641.9±1112.8	51.0±6.0	0.13
GM Aur	59559.91	T	0.27±0.03	0.9±0.8	2.7±0.3	0.2±0.1	9621.8±1134.0	51.1±5.9	0.13
GM Aur	59559.95	T	0.31±0.03	0.9±0.8	2.7±0.3	0.2±0.1	9624.2±1129.2	50.5±5.7	0.13
GM Aur	59910.17	E	0.22±0.02	0.9±0.6	3.1±0.3	0.3±0.1	9833.3±1075.8	52.1±5.6	0.12
GM Aur	59910.21	C	0.21±0.02	0.8±0.6	3.0±0.3	0.3±0.1	9887.2±1039.5	52.0±5.5	0.13
GM Aur	59911.19	C	0.16±0.02	0.8±0.6	2.9±0.3	0.3±0.1	9683.6±1069.2	51.5±5.6	0.12
GM Aur	59912.20	C	0.43±0.04	1.0±0.8	3.2±0.3	0.4±0.1	9548.8±1074.9	54.8±5.1	0.12
GM Aur	59913.18	C	0.29±0.03	1.0±0.7	3.1±0.3	0.4±0.1	9806.9±1067.1	55.8±5.0	0.13
GM Aur	59914.19	C	0.23±0.02	1.0±0.7	3.0±0.3	0.3±0.1	9964.5±1053.8	51.2±5.5	0.11
GM Aur	59915.13	E	0.31±0.03	1.0±0.7	3.0±0.2	0.3±0.1	9980.7±1050.0	51.4±5.6	0.11
GM Aur	59915.20	C	0.29±0.03	0.9±0.7	2.9±0.2	0.3±0.1	9859.6±1022.0	51.2±5.2	0.11
GM Aur	59916.16	E	0.26±0.03	1.0±0.7	3.1±0.3	0.3±0.1	9755.1±1049.1	54.3±5.5	0.11

Table 8 continued

**Table 8** (*continued*)

Object	MJD	Instrument	$r_V$	$\dot{M}$	$R_{in}$	$W_r$	$T_{max}$	Incl.	MAPE
				[ $10^8 M_{\odot} \text{yr}^{-1}$ ]	[ $R_{\star}$ ]	[ $R_{\star}$ ]	[K]	[ $^{\circ}$ ]	
GM Aur	59916.21	C	0.24±0.02	1.0±0.8	3.0±0.3	0.3±0.1	9581.3±1059.2	54.8±5.8	0.12
GM Aur	59917.19	C	0.24±0.02	0.8±0.6	2.9±0.2	0.2±0.1	9929.7±1009.8	49.8±4.9	0.13
GM Aur	59918.19	C	0.28±0.03	1.0±0.8	3.1±0.3	0.4±0.2	9539.3±1078.0	57.0±4.7	0.12
GM Aur	59919.18	C	0.25±0.03	1.0±0.8	3.0±0.3	0.3±0.2	9568.2±1072.8	56.7±5.1	0.12
GM Aur	59920.18	C	0.35±0.04	1.0±0.7	2.7±0.2	0.2±0.1	9844.8±1057.3	50.5±5.9	0.12
GM Aur	59922.18	C	0.44±0.04	0.9±0.9	2.6±0.2	0.2±0.1	9468.9±1131.0	49.9±5.4	0.11
GM Aur	59925.18	C	0.26±0.03	1.4±1.1	3.1±0.3	0.5±0.2	9591.9±1133.6	57.5±4.6	0.13
GM Aur	59926.17	C	0.28±0.03	1.2±1.0	3.0±0.2	0.2±0.1	9811.3±1060.7	51.7±5.9	0.13
GM Aur	59927.18	C	0.30±0.03	1.4±1.1	2.9±0.3	0.4±0.2	9627.2±1129.8	55.2±5.9	0.12
GM Aur	59928.15	C	0.27±0.03	0.9±0.6	2.9±0.2	0.2±0.1	9997.8±993.4	50.4±5.1	0.13
GM Aur	59929.16	C	0.39±0.04	1.2±0.9	3.2±0.2	0.3±0.1	9890.0±1054.8	51.0±5.3	0.14
GM Aur	59931.14	C	0.42±0.04	1.0±0.7	3.1±0.3	0.3±0.1	9906.9±1048.1	53.6±5.7	0.14

NOTE—Instrument names are abbreviated as: C: CHIRON, E: ESPRESSO, X: XSHOOTER, S: SOPHIE, U: UVES, T: TCES

## B. OPTICAL LINE LUMINOSITIES

Tables 9–12 present the measured lines luminosities for all 14 lines we focus on. Figure 9 and 10 shows the line luminosities for the remaining 7 lines over time for TW Hya/RU Lup and BP Tau/GM Aur, respectively.  $H\alpha$ ,  $H\beta$ , and  $H\gamma$  are shown in Figure 2 in Section 3.1.1.

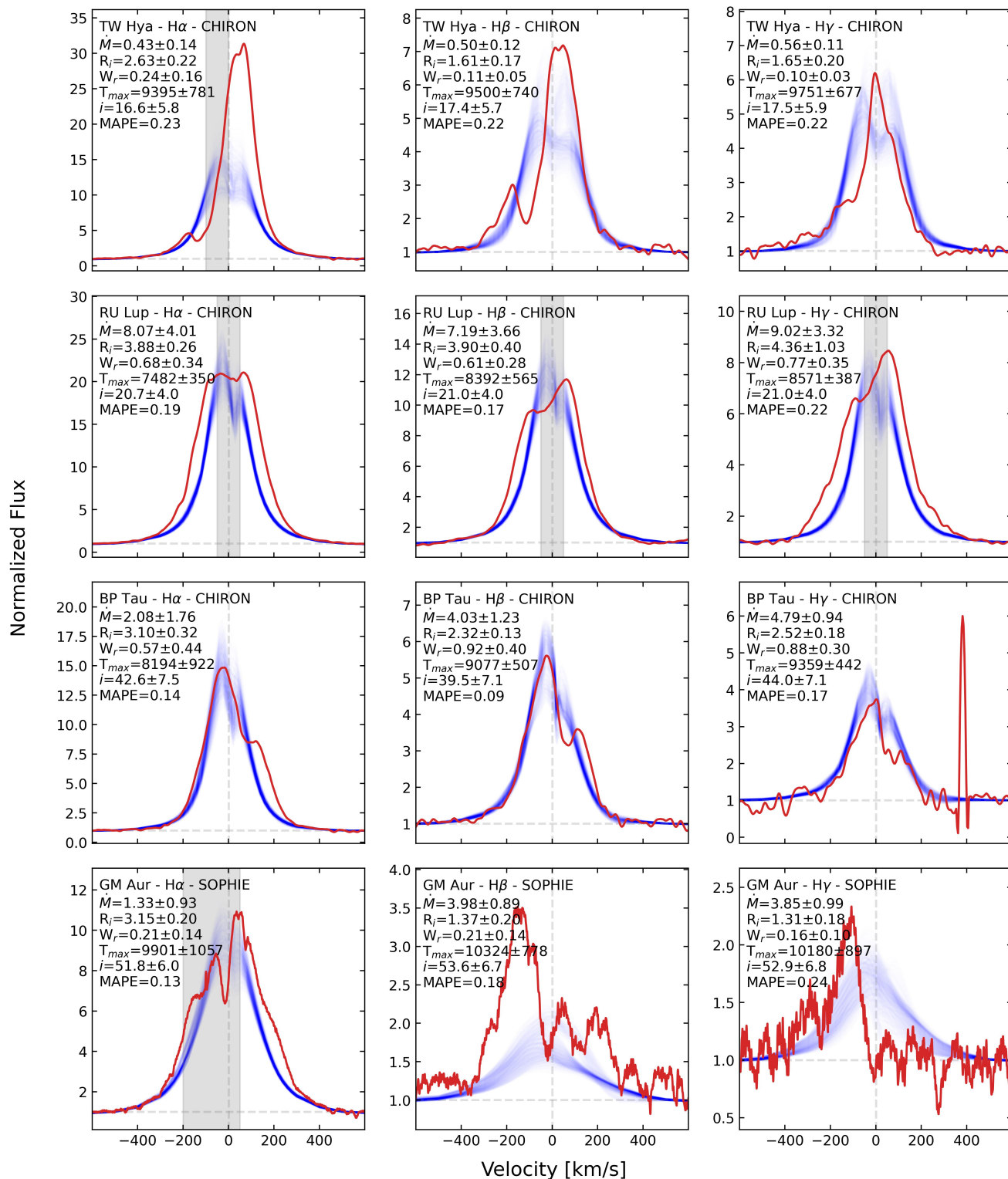


**Figure 8.** Examples of flow model fits for the worst-fit observation for each target. Top to bottom: TW Hya, RU Lup, BP Tau, GM Aur. Left to right: H $\alpha$ , H $\beta$ , H $\gamma$ . Solid red line is observed spectrum. Blue lines are 500 best-fit models. Grey regions denote regions not fit by the flow model. Examples of best-fit observations can be found in Figure 5.

Table 9. Line luminosities for TW Hya

Object	MJD	Inst.	H $\alpha$	H $\beta$	H $\gamma$	H $\delta$	He 14387	He 14471	He 14713	He 15015	He 15875	He 16678	He 17065
TW Hya	59241.30	C	283.0 $\pm$ 1.0	27.5 $\pm$ 3.0	23.4 $\pm$ 2.7	13.7 $\pm$ 1.6	-1.7 $\pm$ 0.5	2.9 $\pm$ 0.5	1.4 $\pm$ 0.4	-0.5 $\pm$ 0.3	2.0 $\pm$ 0.3	0.2 $\pm$ 0.2	0.3 $\pm$ 0.2
TW Hya	59280.17	C	477.0 $\pm$ 0.7	47.9 $\pm$ 4.9	28.1 $\pm$ 2.9	17.9 $\pm$ 1.9	-0.9 $\pm$ 0.3	3.2 $\pm$ 0.4	0.8 $\pm$ 0.3	0.1 $\pm$ 0.2	2.7 $\pm$ 0.3	0.5 $\pm$ 0.1	0.6 $\pm$ 0.2
TW Hya	59280.29	E	489.0 $\pm$ 1.2	51.2 $\pm$ 5.3	30.1 $\pm$ 3.6	19.4 $\pm$ 2.4	-0.5 $\pm$ 0.6	2.5 $\pm$ 0.6	0.4 $\pm$ 0.3	0.2 $\pm$ 0.3	3.1 $\pm$ 0.4	0.5 $\pm$ 0.2	1.0 $\pm$ 0.2
TW Hya	59281.18	C	497.0 $\pm$ 0.6	62.6 $\pm$ 6.3	35.2 $\pm$ 3.6	22.3 $\pm$ 2.3	-0.8 $\pm$ 0.3	3.2 $\pm$ 0.4	0.8 $\pm$ 0.2	0.2 $\pm$ 0.2	3.6 $\pm$ 0.4	0.5 $\pm$ 0.1	0.9 $\pm$ 0.2
TW Hya	59284.24	C	438.0 $\pm$ 0.7	54.5 $\pm$ 5.5	31.6 $\pm$ 3.3	21.4 $\pm$ 2.2	-0.7 $\pm$ 0.3	3.2 $\pm$ 0.4	1.0 $\pm$ 0.3	0.1 $\pm$ 0.2	3.2 $\pm$ 0.3	0.8 $\pm$ 0.1	0.9 $\pm$ 0.2
TW Hya	59286.26	C	310.0 $\pm$ 0.7	24.5 $\pm$ 2.6	17.4 $\pm$ 1.9	10.6 $\pm$ 1.1	-0.9 $\pm$ 0.3	2.1 $\pm$ 0.3	0.6 $\pm$ 0.3	-0.4 $\pm$ 0.2	1.1 $\pm$ 0.2	0.1 $\pm$ 0.1	0.1 $\pm$ 0.2
TW Hya	59288.25	C	592.0 $\pm$ 0.8	67.1 $\pm$ 6.8	36.4 $\pm$ 3.8	23.1 $\pm$ 2.4	-0.9 $\pm$ 0.3	3.8 $\pm$ 0.5	0.9 $\pm$ 0.3	0.2 $\pm$ 0.2	3.6 $\pm$ 0.4	0.7 $\pm$ 0.2	1.1 $\pm$ 0.2
TW Hya	59291.18	C	401.0 $\pm$ 0.6	44.7 $\pm$ 4.5	24.8 $\pm$ 2.6	14.8 $\pm$ 1.5	-0.4 $\pm$ 0.2	1.7 $\pm$ 0.3	0.5 $\pm$ 0.2	0.1 $\pm$ 0.2	2.9 $\pm$ 0.3	0.4 $\pm$ 0.1	0.6 $\pm$ 0.2
TW Hya	59294.17	C	411.0 $\pm$ 0.8	36.0 $\pm$ 3.7	21.2 $\pm$ 2.4	13.3 $\pm$ 1.5	-0.4 $\pm$ 0.3	1.7 $\pm$ 0.4	0.5 $\pm$ 0.3	0.2 $\pm$ 0.2	2.6 $\pm$ 0.3	0.3 $\pm$ 0.1	0.2 $\pm$ 0.2
TW Hya	59295.20	C	487.0 $\pm$ 0.7	59.1 $\pm$ 6.0	33.0 $\pm$ 3.4	21.2 $\pm$ 2.2	-0.2 $\pm$ 0.3	2.7 $\pm$ 0.4	0.6 $\pm$ 0.2	0.6 $\pm$ 0.2	4.1 $\pm$ 0.4	0.9 $\pm$ 0.1	1.0 $\pm$ 0.2
TW Hya	59296.18	C	649.0 $\pm$ 0.7	95.6 $\pm$ 9.6	50.7 $\pm$ 5.1	32.8 $\pm$ 3.3	-0.0 $\pm$ 0.3	4.5 $\pm$ 0.5	1.1 $\pm$ 0.3	1.2 $\pm$ 0.2	8.2 $\pm$ 0.8	2.0 $\pm$ 0.2	2.4 $\pm$ 0.3
TW Hya	59298.15	C	446.0 $\pm$ 0.6	50.4 $\pm$ 5.1	28.8 $\pm$ 3.0	18.7 $\pm$ 1.9	-0.3 $\pm$ 0.2	2.5 $\pm$ 0.3	0.4 $\pm$ 0.2	0.3 $\pm$ 0.2	3.2 $\pm$ 0.3	0.7 $\pm$ 0.1	0.7 $\pm$ 0.2
TW Hya	59300.11	C	324.0 $\pm$ 0.7	29.1 $\pm$ 3.0	18.7 $\pm$ 2.0	12.2 $\pm$ 1.3	-0.4 $\pm$ 0.2	1.8 $\pm$ 0.3	0.4 $\pm$ 0.2	0.0 $\pm$ 0.2	2.2 $\pm$ 0.2	0.3 $\pm$ 0.1	0.4 $\pm$ 0.2
TW Hya	59302.13	C	282.0 $\pm$ 0.6	31.6 $\pm$ 3.2	21.8 $\pm$ 2.3	14.7 $\pm$ 1.5	-0.4 $\pm$ 0.2	1.9 $\pm$ 0.3	0.4 $\pm$ 0.2	0.2 $\pm$ 0.2	2.2 $\pm$ 0.2	0.5 $\pm$ 0.1	0.4 $\pm$ 0.2
TW Hya	59303.12	C	395.0 $\pm$ 0.7	45.5 $\pm$ 4.6	23.8 $\pm$ 2.5	14.0 $\pm$ 1.5	-0.5 $\pm$ 0.2	1.8 $\pm$ 0.3	0.3 $\pm$ 0.2	0.1 $\pm$ 0.2	2.7 $\pm$ 0.3	0.4 $\pm$ 0.1	0.5 $\pm$ 0.2
TW Hya	59304.16	C	471.0 $\pm$ 0.6	59.7 $\pm$ 6.0	32.8 $\pm$ 3.4	21.9 $\pm$ 2.2	-0.7 $\pm$ 0.3	2.7 $\pm$ 0.4	0.7 $\pm$ 0.2	0.2 $\pm$ 0.2	3.3 $\pm$ 0.3	0.6 $\pm$ 0.1	0.7 $\pm$ 0.2
TW Hya	59305.12	C	482.0 $\pm$ 0.7	56.2 $\pm$ 5.7	28.6 $\pm$ 3.0	18.4 $\pm$ 1.9	-0.7 $\pm$ 0.3	2.9 $\pm$ 0.4	0.6 $\pm$ 0.2	0.2 $\pm$ 0.2	3.8 $\pm$ 0.4	0.7 $\pm$ 0.1	1.0 $\pm$ 0.2
TW Hya	59306.15	C	516.0 $\pm$ 0.6	62.0 $\pm$ 6.3	31.7 $\pm$ 3.2	20.6 $\pm$ 2.1	-0.4 $\pm$ 0.2	2.4 $\pm$ 0.3	0.5 $\pm$ 0.2	0.1 $\pm$ 0.2	3.1 $\pm$ 0.3	0.3 $\pm$ 0.1	0.6 $\pm$ 0.2
TW Hya	59307.00	X	440.0 $\pm$ 2.8	60.3 $\pm$ 6.2	31.9 $\pm$ 3.3	21.0 $\pm$ 2.1	-0.1 $\pm$ 0.3	3.5 $\pm$ 0.5	0.8 $\pm$ 0.4	0.8 $\pm$ 0.4	7.1 $\pm$ 0.8	1.8 $\pm$ 0.5	2.1 $\pm$ 0.6
TW Hya	59307.16	C	466.0 $\pm$ 0.8	64.5 $\pm$ 6.5	30.7 $\pm$ 3.3	21.0 $\pm$ 2.3	-0.9 $\pm$ 0.4	3.9 $\pm$ 0.5	0.8 $\pm$ 0.3	0.3 $\pm$ 0.2	4.5 $\pm$ 0.5	0.9 $\pm$ 0.2	1.1 $\pm$ 0.2
TW Hya	59308.04	E	489.0 $\pm$ 1.8	54.5 $\pm$ 5.8	31.7 $\pm$ 4.2	20.3 $\pm$ 3.0	-0.4 $\pm$ 0.8	2.6 $\pm$ 0.8	0.1 $\pm$ 0.5	0.3 $\pm$ 0.5	3.7 $\pm$ 0.5	0.5 $\pm$ 0.3	1.0 $\pm$ 0.3
TW Hya	59308.13	C	471.0 $\pm$ 0.8	59.2 $\pm$ 6.0	33.7 $\pm$ 3.5	23.8 $\pm$ 2.5	-0.4 $\pm$ 0.3	3.6 $\pm$ 0.5	1.1 $\pm$ 0.3	0.4 $\pm$ 0.2	4.3 $\pm$ 0.5	1.3 $\pm$ 0.2	0.9 $\pm$ 0.2
TW Hya	59309.14	C	608.0 $\pm$ 0.7	84.7 $\pm$ 8.5	43.9 $\pm$ 4.5	31.0 $\pm$ 3.2	-0.6 $\pm$ 0.3	4.4 $\pm$ 0.5	0.8 $\pm$ 0.3	1.3 $\pm$ 0.2	8.3 $\pm$ 0.8	2.2 $\pm$ 0.3	2.5 $\pm$ 0.3
TW Hya	59309.14	E	579.0 $\pm$ 1.1	79.5 $\pm$ 8.0	44.3 $\pm$ 4.6	28.9 $\pm$ 3.1	0.0 $\pm$ 0.4	3.9 $\pm$ 0.5	0.6 $\pm$ 0.3	1.0 $\pm$ 0.3	7.5 $\pm$ 0.8	1.6 $\pm$ 0.3	2.4 $\pm$ 0.3
TW Hya	59310.09	E	561.0 $\pm$ 1.0	71.8 $\pm$ 7.3	37.9 $\pm$ 4.0	23.4 $\pm$ 2.6	-0.0 $\pm$ 0.4	3.1 $\pm$ 0.5	0.7 $\pm$ 0.3	0.6 $\pm$ 0.3	4.7 $\pm$ 0.5	0.9 $\pm$ 0.2	1.6 $\pm$ 0.2
TW Hya	59310.13	C	576.0 $\pm$ 0.7	75.3 $\pm$ 7.6	38.4 $\pm$ 3.9	23.9 $\pm$ 2.4	-0.4 $\pm$ 0.3	3.1 $\pm$ 0.4	0.7 $\pm$ 0.2	0.5 $\pm$ 0.2	3.8 $\pm$ 0.4	0.8 $\pm$ 0.1	1.1 $\pm$ 0.2
TW Hya	59310.15	X	554.0 $\pm$ 1.7	68.5 $\pm$ 7.0	32.5 $\pm$ 3.3	20.1 $\pm$ 2.0	-0.2 $\pm$ 0.3	2.9 $\pm$ 0.4	0.6 $\pm$ 0.3	0.5 $\pm$ 0.3	4.0 $\pm$ 0.5	0.6 $\pm$ 0.3	1.1 $\pm$ 0.5
TW Hya	59311.14	C	440.0 $\pm$ 0.6	42.4 $\pm$ 4.3	23.5 $\pm$ 2.5	14.4 $\pm$ 1.5	-0.6 $\pm$ 0.3	1.7 $\pm$ 0.3	0.5 $\pm$ 0.2	-0.1 $\pm$ 0.2	2.2 $\pm$ 0.2	0.2 $\pm$ 0.1	0.6 $\pm$ 0.2
TW Hya	59312.16	C	345.0 $\pm$ 0.6	31.1 $\pm$ 3.2	17.6 $\pm$ 1.9	11.7 $\pm$ 1.2	-0.5 $\pm$ 0.2	1.7 $\pm$ 0.3	0.4 $\pm$ 0.2	0.0 $\pm$ 0.2	1.6 $\pm$ 0.2	0.1 $\pm$ 0.1	0.4 $\pm$ 0.2
TW Hya	59313.15	C	279.0 $\pm$ 0.7	26.2 $\pm$ 2.8	18.0 $\pm$ 2.0	11.1 $\pm$ 1.2	-0.4 $\pm$ 0.3	1.5 $\pm$ 0.3	0.3 $\pm$ 0.2	-0.0 $\pm$ 0.2	1.8 $\pm$ 0.2	0.4 $\pm$ 0.1	0.2 $\pm$ 0.2
TW Hya	59313.22	E	287.0 $\pm$ 1.1	27.3 $\pm$ 2.9	19.2 $\pm$ 2.6	12.5 $\pm$ 1.8	-0.6 $\pm$ 0.5	1.7 $\pm$ 0.5	0.3 $\pm$ 0.3	-0.2 $\pm$ 0.3	1.2 $\pm$ 0.2	0.2 $\pm$ 0.2	0.4 $\pm$ 0.2
TW Hya	59314.23	C	311.0 $\pm$ 0.7	32.0 $\pm$ 3.3	19.1 $\pm$ 2.1	11.7 $\pm$ 1.3	-0.5 $\pm$ 0.3	1.5 $\pm$ 0.3	0.3 $\pm$ 0.3	-0.1 $\pm$ 0.2	2.1 $\pm$ 0.2	0.4 $\pm$ 0.1	0.1 $\pm$ 0.2
TW Hya	59653.15	C	450.0 $\pm$ 0.6	30.7 $\pm$ 3.1	17.5 $\pm$ 1.9	10.8 $\pm$ 1.1	-0.3 $\pm$ 0.2	1.5 $\pm$ 0.3	0.3 $\pm$ 0.2	-0.1 $\pm$ 0.2	2.2 $\pm$ 0.2	0.2 $\pm$ 0.1	0.2 $\pm$ 0.2
TW Hya	59654.15	C	623.0 $\pm$ 0.8	51.9 $\pm$ 5.3	29.6 $\pm$ 3.0	19.7 $\pm$ 2.0	-0.5 $\pm$ 0.3	2.9 $\pm$ 0.4	0.6 $\pm$ 0.3	-0.1 $\pm$ 0.2	5.7 $\pm$ 0.6	0.9 $\pm$ 0.2	1.0 $\pm$ 0.2
TW Hya	59656.17	C	484.0 $\pm$ 0.7	37.6 $\pm$ 3.8	21.0 $\pm$ 2.2	14.9 $\pm$ 1.6	-0.5 $\pm$ 0.3	2.5 $\pm$ 0.3	0.4 $\pm$ 0.2	0.2 $\pm$ 0.2	3.7 $\pm$ 0.4	0.6 $\pm$ 0.1	0.6 $\pm$ 0.2
TW Hya	59657.21	C	566.0 $\pm$ 0.7	52.8 $\pm$ 5.4	28.5 $\pm$ 3.0	18.9 $\pm$ 1.9	-0.5 $\pm$ 0.3	3.0 $\pm$ 0.4	0.6 $\pm$ 0.2	0.3 $\pm$ 0.2	5.1 $\pm$ 0.5	1.1 $\pm$ 0.2	1.1 $\pm$ 0.2
TW Hya	59658.19	C	351.0 $\pm$ 0.7	32.2 $\pm$ 3.3	23.1 $\pm$ 2.4	17.3 $\pm$ 1.8	-0.6 $\pm$ 0.2	2.5 $\pm$ 0.3	0.6 $\pm$ 0.2	0.1 $\pm$ 0.2	3.5 $\pm$ 0.4	1.0 $\pm$ 0.2	0.5 $\pm$ 0.2
TW Hya	59659.20	C	497.0 $\pm$ 0.6	53.5 $\pm$ 5.4	27.2 $\pm$ 2.8	18.1 $\pm$ 1.9	-0.3 $\pm$ 0.2	3.0 $\pm$ 0.4	0.6 $\pm$ 0.2	0.4 $\pm$ 0.2	4.5 $\pm$ 0.5	0.9 $\pm$ 0.1	0.8 $\pm$ 0.2

Table 9 continued

Table 9 (continued)

Object	MJD	Inst.	H $\alpha$	H $\beta$	H $\gamma$	H $\delta$	He 14387	He 14471	He 14713	He 15015	He 15875	He 16678	He 17065
TW Hya	59660.15	C	459.0 $\pm$ 0.6	49.5 $\pm$ 5.0	28.2 $\pm$ 2.9	19.2 $\pm$ 2.0	-0.3 $\pm$ 0.2	2.9 $\pm$ 0.4	0.6 $\pm$ 0.2	0.3 $\pm$ 0.2	4.3 $\pm$ 0.4	1.1 $\pm$ 0.1	0.9 $\pm$ 0.2
TW Hya	59661.22	C	381.0 $\pm$ 0.5	40.7 $\pm$ 4.1	25.2 $\pm$ 2.6	16.7 $\pm$ 1.7	-0.3 $\pm$ 0.2	1.9 $\pm$ 0.3	0.4 $\pm$ 0.2	0.2 $\pm$ 0.2	3.4 $\pm$ 0.4	0.7 $\pm$ 0.1	0.5 $\pm$ 0.1
TW Hya	59662.16	C	332.0 $\pm$ 0.6	35.6 $\pm$ 3.6	24.3 $\pm$ 2.5	17.0 $\pm$ 1.7	-0.4 $\pm$ 0.2	2.4 $\pm$ 0.3	0.5 $\pm$ 0.2	0.4 $\pm$ 0.2	3.3 $\pm$ 0.3	0.7 $\pm$ 0.1	0.4 $\pm$ 0.2
TW Hya	59663.18	C	278.0 $\pm$ 0.6	26.4 $\pm$ 2.7	17.8 $\pm$ 1.9	12.0 $\pm$ 1.2	-0.6 $\pm$ 0.2	1.6 $\pm$ 0.3	0.2 $\pm$ 0.2	0.1 $\pm$ 0.2	1.9 $\pm$ 0.2	0.5 $\pm$ 0.1	0.1 $\pm$ 0.1
TW Hya	59664.14	C	258.0 $\pm$ 0.5	23.1 $\pm$ 2.4	14.8 $\pm$ 1.6	9.9 $\pm$ 1.0	-0.6 $\pm$ 0.2	1.4 $\pm$ 0.2	0.3 $\pm$ 0.2	-0.2 $\pm$ 0.2	1.7 $\pm$ 0.2	0.3 $\pm$ 0.1	-0.0 $\pm$ 0.1
TW Hya	59665.16	C	379.0 $\pm$ 0.6	44.7 $\pm$ 4.5	27.5 $\pm$ 2.8	18.5 $\pm$ 1.9	-0.6 $\pm$ 0.2	2.4 $\pm$ 0.3	0.5 $\pm$ 0.2	0.2 $\pm$ 0.2	3.2 $\pm$ 0.3	0.7 $\pm$ 0.1	0.4 $\pm$ 0.2
TW Hya	59666.19	C	448.0 $\pm$ 0.6	70.9 $\pm$ 7.1	38.8 $\pm$ 3.9	25.4 $\pm$ 2.6	-0.5 $\pm$ 0.2	3.1 $\pm$ 0.4	0.6 $\pm$ 0.2	0.3 $\pm$ 0.2	5.4 $\pm$ 0.6	1.1 $\pm$ 0.2	1.2 $\pm$ 0.2
TW Hya	59667.14	C	364.0 $\pm$ 0.6	40.2 $\pm$ 4.1	24.2 $\pm$ 2.5	16.9 $\pm$ 1.7	-0.6 $\pm$ 0.2	2.8 $\pm$ 0.3	0.7 $\pm$ 0.2	0.1 $\pm$ 0.2	3.5 $\pm$ 0.4	0.5 $\pm$ 0.1	0.7 $\pm$ 0.2
TW Hya	59668.14	C	392.0 $\pm$ 0.6	45.3 $\pm$ 4.6	27.2 $\pm$ 2.8	18.6 $\pm$ 1.9	-0.7 $\pm$ 0.2	2.1 $\pm$ 0.3	0.5 $\pm$ 0.2	-0.0 $\pm$ 0.2	3.3 $\pm$ 0.3	0.6 $\pm$ 0.1	0.4 $\pm$ 0.1
TW Hya	59670.10	C	374.0 $\pm$ 0.6	48.2 $\pm$ 4.9	28.5 $\pm$ 2.9	18.6 $\pm$ 1.9	-0.2 $\pm$ 0.2	2.8 $\pm$ 0.3	0.6 $\pm$ 0.2	0.5 $\pm$ 0.2	3.8 $\pm$ 0.4	1.2 $\pm$ 0.2	0.9 $\pm$ 0.2
TW Hya	59671.06	C	360.0 $\pm$ 0.6	36.2 $\pm$ 3.7	21.8 $\pm$ 2.3	14.6 $\pm$ 1.5	-0.3 $\pm$ 0.2	2.1 $\pm$ 0.3	0.5 $\pm$ 0.2	0.0 $\pm$ 0.2	2.9 $\pm$ 0.3	0.6 $\pm$ 0.1	0.5 $\pm$ 0.2
TW Hya	59672.01	C	304.0 $\pm$ 0.5	26.0 $\pm$ 2.7	17.4 $\pm$ 1.8	11.0 $\pm$ 1.1	-0.4 $\pm$ 0.2	1.6 $\pm$ 0.3	0.4 $\pm$ 0.2	-0.1 $\pm$ 0.2	2.3 $\pm$ 0.2	0.3 $\pm$ 0.1	0.2 $\pm$ 0.1
TW Hya	59672.26	C	315.0 $\pm$ 0.6	29.9 $\pm$ 3.1	18.6 $\pm$ 1.9	11.3 $\pm$ 1.2	-0.2 $\pm$ 0.2	1.7 $\pm$ 0.3	0.3 $\pm$ 0.2	0.0 $\pm$ 0.2	2.6 $\pm$ 0.3	0.4 $\pm$ 0.1	0.2 $\pm$ 0.1
TW Hya	59673.13	C	325.0 $\pm$ 0.5	39.2 $\pm$ 4.0	25.8 $\pm$ 2.6	17.1 $\pm$ 1.7	-0.3 $\pm$ 0.2	2.2 $\pm$ 0.3	0.5 $\pm$ 0.2	0.3 $\pm$ 0.2	3.5 $\pm$ 0.4	1.1 $\pm$ 0.1	0.5 $\pm$ 0.1
TW Hya	59674.14	C	431.0 $\pm$ 0.6	53.1 $\pm$ 5.4	33.3 $\pm$ 3.4	23.1 $\pm$ 2.3	-0.0 $\pm$ 0.2	3.1 $\pm$ 0.4	0.7 $\pm$ 0.2	0.6 $\pm$ 0.2	5.4 $\pm$ 0.5	1.5 $\pm$ 0.2	1.2 $\pm$ 0.2
TW Hya	59675.09	C	345.0 $\pm$ 0.6	31.8 $\pm$ 3.3	22.2 $\pm$ 2.3	15.7 $\pm$ 1.6	-0.2 $\pm$ 0.2	2.3 $\pm$ 0.3	0.4 $\pm$ 0.2	0.2 $\pm$ 0.2	3.2 $\pm$ 0.3	0.9 $\pm$ 0.1	0.4 $\pm$ 0.1
TW Hya	59676.01	C	479.0 $\pm$ 0.6	55.9 $\pm$ 5.6	32.6 $\pm$ 3.3	22.7 $\pm$ 2.3	-0.2 $\pm$ 0.2	3.0 $\pm$ 0.4	0.6 $\pm$ 0.2	0.4 $\pm$ 0.2	4.3 $\pm$ 0.4	0.9 $\pm$ 0.1	0.7 $\pm$ 0.2
TW Hya	59676.23	C	456.0 $\pm$ 0.6	49.2 $\pm$ 5.0	26.8 $\pm$ 2.8	17.0 $\pm$ 1.7	-0.3 $\pm$ 0.2	2.5 $\pm$ 0.3	0.5 $\pm$ 0.2	0.4 $\pm$ 0.2	4.3 $\pm$ 0.4	1.2 $\pm$ 0.2	0.9 $\pm$ 0.2
TW Hya	59677.07	C	485.0 $\pm$ 0.6	57.8 $\pm$ 5.8	30.2 $\pm$ 3.1	18.9 $\pm$ 1.9	-0.3 $\pm$ 0.2	2.4 $\pm$ 0.3	0.4 $\pm$ 0.2	0.2 $\pm$ 0.2	3.3 $\pm$ 0.3	0.8 $\pm$ 0.1	0.5 $\pm$ 0.2
TW Hya	59678.01	C	343.0 $\pm$ 0.6	34.4 $\pm$ 3.5	23.0 $\pm$ 2.4	15.6 $\pm$ 1.6	-0.4 $\pm$ 0.2	1.9 $\pm$ 0.3	0.3 $\pm$ 0.2	0.1 $\pm$ 0.2	3.2 $\pm$ 0.3	0.3 $\pm$ 0.1	0.5 $\pm$ 0.2
TW Hya	59678.18	C	354.0 $\pm$ 0.6	33.2 $\pm$ 3.4	23.2 $\pm$ 2.4	15.5 $\pm$ 1.6	-0.4 $\pm$ 0.2	2.1 $\pm$ 0.3	0.4 $\pm$ 0.2	0.0 $\pm$ 0.2	2.9 $\pm$ 0.3	0.2 $\pm$ 0.1	0.2 $\pm$ 0.2
TW Hya	59679.05	C	458.0 $\pm$ 0.6	53.0 $\pm$ 5.3	30.5 $\pm$ 3.1	19.8 $\pm$ 2.0	-0.2 $\pm$ 0.2	2.4 $\pm$ 0.3	0.5 $\pm$ 0.2	0.2 $\pm$ 0.2	3.7 $\pm$ 0.4	0.5 $\pm$ 0.1	0.7 $\pm$ 0.2
TW Hya	59680.07	C	482.0 $\pm$ 0.6	49.5 $\pm$ 5.0	26.9 $\pm$ 2.8	16.8 $\pm$ 1.7	-0.4 $\pm$ 0.2	1.9 $\pm$ 0.3	0.3 $\pm$ 0.2	0.1 $\pm$ 0.2	3.3 $\pm$ 0.3	0.3 $\pm$ 0.1	0.5 $\pm$ 0.2
TW Hya	59682.09	C	491.0 $\pm$ 0.6	57.5 $\pm$ 5.8	31.6 $\pm$ 3.2	19.7 $\pm$ 2.0	-0.3 $\pm$ 0.2	2.6 $\pm$ 0.3	0.6 $\pm$ 0.2	0.5 $\pm$ 0.2	4.6 $\pm$ 0.5	1.1 $\pm$ 0.2	1.1 $\pm$ 0.2
TW Hya	59684.15	C	461.0 $\pm$ 0.6	53.2 $\pm$ 5.4	32.1 $\pm$ 3.3	21.8 $\pm$ 2.2	-0.1 $\pm$ 0.2	3.0 $\pm$ 0.4	0.7 $\pm$ 0.2	0.6 $\pm$ 0.2	5.9 $\pm$ 0.6	1.7 $\pm$ 0.2	1.6 $\pm$ 0.2
TW Hya	59686.12	C	482.0 $\pm$ 0.6	56.5 $\pm$ 5.7	30.2 $\pm$ 3.1	18.8 $\pm$ 1.9	-0.3 $\pm$ 0.2	2.4 $\pm$ 0.3	0.5 $\pm$ 0.2	0.4 $\pm$ 0.2	4.4 $\pm$ 0.5	1.0 $\pm$ 0.1	0.9 $\pm$ 0.2
TW Hya	59688.09	C	471.0 $\pm$ 0.6	56.1 $\pm$ 5.6	33.4 $\pm$ 3.4	23.1 $\pm$ 2.3	-0.2 $\pm$ 0.2	2.8 $\pm$ 0.3	0.6 $\pm$ 0.2	0.4 $\pm$ 0.2	4.9 $\pm$ 0.5	1.2 $\pm$ 0.2	1.0 $\pm$ 0.2
TW Hya	59690.06	C	482.0 $\pm$ 0.8	56.0 $\pm$ 5.7	32.3 $\pm$ 3.5	18.8 $\pm$ 2.1	-0.1 $\pm$ 0.4	2.4 $\pm$ 0.4	0.3 $\pm$ 0.3	0.5 $\pm$ 0.3	3.5 $\pm$ 0.4	1.0 $\pm$ 0.2	0.2 $\pm$ 0.2
TW Hya	59692.07	C	426.0 $\pm$ 0.6	49.1 $\pm$ 5.0	32.0 $\pm$ 3.3	21.4 $\pm$ 2.2	-0.3 $\pm$ 0.2	3.0 $\pm$ 0.4	0.6 $\pm$ 0.2	0.6 $\pm$ 0.2	4.4 $\pm$ 0.5	1.4 $\pm$ 0.2	1.0 $\pm$ 0.2
TW Hya	59694.03	C	558.0 $\pm$ 0.7	63.8 $\pm$ 6.4	35.9 $\pm$ 3.7	22.8 $\pm$ 2.3	-0.1 $\pm$ 0.3	3.0 $\pm$ 0.4	0.5 $\pm$ 0.2	0.5 $\pm$ 0.2	4.1 $\pm$ 0.4	1.2 $\pm$ 0.2	0.8 $\pm$ 0.2
TW Hya	59695.05	C	495.0 $\pm$ 0.6	42.5 $\pm$ 4.3	24.3 $\pm$ 2.5	15.5 $\pm$ 1.6	-0.2 $\pm$ 0.2	2.2 $\pm$ 0.3	0.5 $\pm$ 0.2	0.2 $\pm$ 0.2	3.0 $\pm$ 0.3	0.5 $\pm$ 0.1	0.5 $\pm$ 0.2
TW Hya	59696.18	C	536.0 $\pm$ 0.6	50.3 $\pm$ 5.1	27.1 $\pm$ 2.8	17.1 $\pm$ 1.8	-0.1 $\pm$ 0.3	2.2 $\pm$ 0.3	0.3 $\pm$ 0.2	0.3 $\pm$ 0.2	4.0 $\pm$ 0.4	0.9 $\pm$ 0.1	0.7 $\pm$ 0.2
TW Hya	59696.24	C	519.0 $\pm$ 0.7	51.7 $\pm$ 5.2	26.2 $\pm$ 2.8	14.8 $\pm$ 1.6	-0.3 $\pm$ 0.3	2.5 $\pm$ 0.4	0.2 $\pm$ 0.2	0.2 $\pm$ 0.2	3.8 $\pm$ 0.4	0.8 $\pm$ 0.1	0.5 $\pm$ 0.2
TW Hya	59697.15	C	383.0 $\pm$ 0.6	37.4 $\pm$ 3.8	26.2 $\pm$ 2.7	17.5 $\pm$ 1.8	-0.1 $\pm$ 0.2	2.2 $\pm$ 0.3	0.3 $\pm$ 0.2	0.1 $\pm$ 0.2	2.9 $\pm$ 0.3	0.7 $\pm$ 0.1	0.4 $\pm$ 0.1
TW Hya	59698.14	C	462.0 $\pm$ 0.6	50.5 $\pm$ 5.1	31.8 $\pm$ 3.2	21.2 $\pm$ 2.2	-0.1 $\pm$ 0.2	2.9 $\pm$ 0.4	0.6 $\pm$ 0.2	0.6 $\pm$ 0.2	3.8 $\pm$ 0.4	1.1 $\pm$ 0.1	0.7 $\pm$ 0.2

NOTE.—Fluxes are in units of  $10^{13}$  erg s $^{-1}$  cm $^{-2}$ . Additional 10% uncertainty due to continuum subtraction has been included in all uncertainties except H $\alpha$  and H $\beta$ . Instrument names are abbreviated as: C: CHIRON, E: ESPRESSO, X: XSHOOTER, S: SOPHIE, U: UVES, T: TCES

Table 10. Line luminosities for RU Lup

Object	MJD	Inst.	H $\alpha$	H $\beta$	H $\gamma$	H $\delta$	He I4387	He I4471	He I4713	He I5015	He I5875	He I6678	He I7065
RU Lup	59264.37	C	288.0 $\pm$ 0.6	69.7 $\pm$ 7.0	30.2 $\pm$ 3.2	18.5 $\pm$ 2.0	3.8 $\pm$ 0.5	4.2 $\pm$ 0.5	0.0 $\pm$ 0.2	18.1 $\pm$ 1.8	8.6 $\pm$ 0.9	3.2 $\pm$ 0.3	2.6 $\pm$ 0.3
RU Lup	59318.26	C	248.0 $\pm$ 0.5	67.8 $\pm$ 6.8	30.7 $\pm$ 3.3	19.1 $\pm$ 2.0	4.4 $\pm$ 0.6	5.3 $\pm$ 0.6	0.3 $\pm$ 0.2	18.2 $\pm$ 1.8	8.9 $\pm$ 0.9	3.1 $\pm$ 0.3	2.7 $\pm$ 0.3
RU Lup	59395.05	C	327.0 $\pm$ 0.5	83.5 $\pm$ 8.4	42.9 $\pm$ 4.4	25.6 $\pm$ 2.6	5.0 $\pm$ 0.6	5.4 $\pm$ 0.6	0.3 $\pm$ 0.2	20.9 $\pm$ 2.1	10.4 $\pm$ 1.0	3.9 $\pm$ 0.4	2.7 $\pm$ 0.3
RU Lup	59434.99	C	260.0 $\pm$ 1.0	70.2 $\pm$ 7.2	35.3 $\pm$ 4.2	13.6 $\pm$ 2.1	3.4 $\pm$ 0.8	4.1 $\pm$ 0.7	0.1 $\pm$ 0.5	15.7 $\pm$ 1.6	6.7 $\pm$ 0.7	2.4 $\pm$ 0.3	2.2 $\pm$ 0.3
RU Lup	59435.98	C	261.0 $\pm$ 0.5	71.1 $\pm$ 7.1	34.6 $\pm$ 3.6	21.4 $\pm$ 2.2	4.2 $\pm$ 0.5	4.4 $\pm$ 0.5	0.2 $\pm$ 0.2	16.9 $\pm$ 1.7	7.5 $\pm$ 0.8	2.7 $\pm$ 0.3	2.1 $\pm$ 0.2
RU Lup	59436.10	X	256.0 $\pm$ 1.8	70.1 $\pm$ 7.1	31.6 $\pm$ 3.6	17.0 $\pm$ 1.9	4.5 $\pm$ 0.8	4.5 $\pm$ 0.7	0.1 $\pm$ 0.3	18.2 $\pm$ 1.8	8.5 $\pm$ 0.9	3.0 $\pm$ 0.4	2.4 $\pm$ 0.3
RU Lup	59437.00	C	265.0 $\pm$ 0.5	79.6 $\pm$ 8.0	38.5 $\pm$ 4.0	24.0 $\pm$ 2.5	5.4 $\pm$ 0.7	5.7 $\pm$ 0.7	0.5 $\pm$ 0.2	19.6 $\pm$ 2.0	8.4 $\pm$ 0.8	3.6 $\pm$ 0.4	2.4 $\pm$ 0.2
RU Lup	59437.97	C	298.0 $\pm$ 0.5	91.1 $\pm$ 9.1	46.2 $\pm$ 4.8	28.3 $\pm$ 2.9	6.5 $\pm$ 0.8	6.7 $\pm$ 0.8	0.2 $\pm$ 0.2	22.9 $\pm$ 2.3	10.5 $\pm$ 1.1	4.0 $\pm$ 0.4	2.9 $\pm$ 0.3
RU Lup	59439.02	C	231.0 $\pm$ 0.5	72.1 $\pm$ 7.2	36.4 $\pm$ 3.8	23.6 $\pm$ 2.4	4.7 $\pm$ 0.6	4.6 $\pm$ 0.6	0.3 $\pm$ 0.2	17.4 $\pm$ 1.7	7.9 $\pm$ 0.8	3.1 $\pm$ 0.3	2.1 $\pm$ 0.2
RU Lup	59439.99	C	271.0 $\pm$ 0.5	78.9 $\pm$ 7.9	41.6 $\pm$ 4.3	25.4 $\pm$ 2.6	4.9 $\pm$ 0.6	5.8 $\pm$ 0.7	0.3 $\pm$ 0.2	18.0 $\pm$ 1.8	9.3 $\pm$ 0.9	3.5 $\pm$ 0.4	2.5 $\pm$ 0.3
RU Lup	59442.03	C	303.0 $\pm$ 0.7	89.8 $\pm$ 9.0	46.1 $\pm$ 4.9	28.7 $\pm$ 3.1	6.1 $\pm$ 0.8	6.3 $\pm$ 0.8	0.2 $\pm$ 0.3	23.3 $\pm$ 2.3	10.8 $\pm$ 1.1	4.0 $\pm$ 0.4	3.0 $\pm$ 0.3
RU Lup	59443.02	C	263.0 $\pm$ 0.5	85.3 $\pm$ 8.6	40.3 $\pm$ 4.2	26.2 $\pm$ 2.7	6.4 $\pm$ 0.8	5.7 $\pm$ 0.7	0.5 $\pm$ 0.2	22.0 $\pm$ 2.2	8.6 $\pm$ 0.9	3.8 $\pm$ 0.4	2.3 $\pm$ 0.2
RU Lup	59443.14	C	233.0 $\pm$ 0.5	92.2 $\pm$ 9.3	40.6 $\pm$ 4.3	22.5 $\pm$ 2.4	7.1 $\pm$ 0.8	6.5 $\pm$ 0.8	0.7 $\pm$ 0.3	24.0 $\pm$ 2.4	8.4 $\pm$ 0.8	3.3 $\pm$ 0.3	1.8 $\pm$ 0.2
RU Lup	59444.02	C	294.0 $\pm$ 0.5	91.4 $\pm$ 9.2	44.9 $\pm$ 4.7	27.2 $\pm$ 2.8	7.3 $\pm$ 0.8	6.4 $\pm$ 0.7	0.3 $\pm$ 0.2	24.3 $\pm$ 2.4	8.8 $\pm$ 0.9	3.8 $\pm$ 0.4	2.4 $\pm$ 0.3
RU Lup	59444.03	C	291.0 $\pm$ 0.8	94.4 $\pm$ 9.5	47.9 $\pm$ 5.1	20.7 $\pm$ 2.5	6.8 $\pm$ 0.9	6.5 $\pm$ 0.8	0.6 $\pm$ 0.4	23.1 $\pm$ 2.3	8.3 $\pm$ 0.8	4.0 $\pm$ 0.4	2.5 $\pm$ 0.3
RU Lup	59447.02	C	289.0 $\pm$ 0.9	113.0 $\pm$ 11.4	51.1 $\pm$ 5.5	19.0 $\pm$ 2.5	6.9 $\pm$ 1.0	7.9 $\pm$ 1.0	-0.3 $\pm$ 0.4	26.1 $\pm$ 2.6	13.3 $\pm$ 1.3	5.3 $\pm$ 0.5	3.3 $\pm$ 0.4
RU Lup	59447.05	C	359.0 $\pm$ 0.6	113.0 $\pm$ 11.3	48.5 $\pm$ 5.0	27.5 $\pm$ 2.9	7.8 $\pm$ 0.9	7.5 $\pm$ 0.8	0.1 $\pm$ 0.3	28.2 $\pm$ 2.8	13.7 $\pm$ 1.4	5.0 $\pm$ 0.5	3.5 $\pm$ 0.4
RU Lup	59448.00	C	359.0 $\pm$ 0.6	94.1 $\pm$ 9.4	43.5 $\pm$ 4.5	26.4 $\pm$ 2.8	6.2 $\pm$ 0.8	6.1 $\pm$ 0.7	0.1 $\pm$ 0.2	22.0 $\pm$ 2.2	12.9 $\pm$ 1.3	4.5 $\pm$ 0.5	3.6 $\pm$ 0.4
RU Lup	59448.07	X	325.0 $\pm$ 1.1	86.2 $\pm$ 8.6	35.7 $\pm$ 4.0	19.1 $\pm$ 2.1	5.4 $\pm$ 0.9	5.8 $\pm$ 0.8	0.2 $\pm$ 0.3	21.4 $\pm$ 2.2	11.4 $\pm$ 1.2	4.1 $\pm$ 0.4	3.2 $\pm$ 0.4
RU Lup	59449.00	E	319.0 $\pm$ 0.8	91.3 $\pm$ 9.2	47.6 $\pm$ 5.0	23.4 $\pm$ 2.6	7.5 $\pm$ 0.9	7.8 $\pm$ 0.9	0.2 $\pm$ 0.3	26.7 $\pm$ 2.7	9.6 $\pm$ 1.0	3.5 $\pm$ 0.4	3.2 $\pm$ 0.3
RU Lup	59449.04	C	342.0 $\pm$ 0.5	89.8 $\pm$ 9.0	40.8 $\pm$ 4.2	23.0 $\pm$ 2.4	6.1 $\pm$ 0.7	5.8 $\pm$ 0.7	0.0 $\pm$ 0.2	25.3 $\pm$ 2.5	11.1 $\pm$ 1.1	4.2 $\pm$ 0.4	3.1 $\pm$ 0.3
RU Lup	59449.98	C	336.0 $\pm$ 0.6	96.8 $\pm$ 9.7	46.8 $\pm$ 4.9	28.2 $\pm$ 3.0	6.9 $\pm$ 0.8	6.2 $\pm$ 0.7	0.1 $\pm$ 0.3	24.7 $\pm$ 2.5	10.4 $\pm$ 1.0	3.4 $\pm$ 0.4	2.9 $\pm$ 0.3
RU Lup	59453.01	C	270.0 $\pm$ 0.6	100.0 $\pm$ 10.0	55.2 $\pm$ 5.8	33.8 $\pm$ 3.5	8.2 $\pm$ 1.0	7.7 $\pm$ 0.9	0.1 $\pm$ 0.3	28.3 $\pm$ 2.8	11.8 $\pm$ 1.2	4.4 $\pm$ 0.5	2.7 $\pm$ 0.3
RU Lup	59458.02	E	253.0 $\pm$ 1.3	72.9 $\pm$ 7.5	36.1 $\pm$ 4.9	19.2 $\pm$ 3.2	5.9 $\pm$ 1.1	5.9 $\pm$ 1.0	0.1 $\pm$ 0.5	20.3 $\pm$ 2.1	10.2 $\pm$ 1.0	4.0 $\pm$ 0.5	3.3 $\pm$ 0.4
RU Lup	59458.06	E	233.0 $\pm$ 1.5	68.4 $\pm$ 7.2	33.5 $\pm$ 6.1	17.8 $\pm$ 4.6	5.4 $\pm$ 1.5	5.3 $\pm$ 1.3	0.1 $\pm$ 0.6	18.9 $\pm$ 2.0	9.1 $\pm$ 1.0	3.5 $\pm$ 0.5	2.9 $\pm$ 0.4
RU Lup	59676.20	C	333.0 $\pm$ 0.6	80.4 $\pm$ 8.1	37.8 $\pm$ 3.9	21.7 $\pm$ 2.3	5.7 $\pm$ 0.7	5.8 $\pm$ 0.7	0.2 $\pm$ 0.2	22.6 $\pm$ 2.3	9.4 $\pm$ 0.9	4.0 $\pm$ 0.4	2.7 $\pm$ 0.3
RU Lup	59723.14	C	204.0 $\pm$ 0.5	54.9 $\pm$ 5.5	27.0 $\pm$ 2.9	16.7 $\pm$ 1.8	3.7 $\pm$ 0.5	3.8 $\pm$ 0.5	0.2 $\pm$ 0.2	14.7 $\pm$ 1.5	7.1 $\pm$ 0.7	2.7 $\pm$ 0.3	2.1 $\pm$ 0.2
RU Lup	59736.11	C	328.0 $\pm$ 0.5	80.3 $\pm$ 8.1	38.5 $\pm$ 4.0	22.5 $\pm$ 2.3	4.8 $\pm$ 0.6	4.9 $\pm$ 0.6	-0.1 $\pm$ 0.2	20.4 $\pm$ 2.0	10.6 $\pm$ 1.1	3.8 $\pm$ 0.4	3.2 $\pm$ 0.3
RU Lup	59790.11	C	301.0 $\pm$ 0.5	85.8 $\pm$ 8.6	44.3 $\pm$ 4.6	27.2 $\pm$ 2.8	4.9 $\pm$ 0.6	5.5 $\pm$ 0.6	-0.0 $\pm$ 0.2	20.5 $\pm$ 2.1	11.4 $\pm$ 1.1	3.9 $\pm$ 0.4	3.5 $\pm$ 0.4
RU Lup	59799.03	C	257.0 $\pm$ 0.5	60.8 $\pm$ 6.1	31.9 $\pm$ 3.3	18.0 $\pm$ 1.9	2.7 $\pm$ 0.4	4.1 $\pm$ 0.5	0.1 $\pm$ 0.2	13.2 $\pm$ 1.3	6.4 $\pm$ 0.6	2.3 $\pm$ 0.2	2.0 $\pm$ 0.2
RU Lup	59800.03	C	288.0 $\pm$ 0.5	76.6 $\pm$ 7.7	39.7 $\pm$ 4.1	23.6 $\pm$ 2.4	4.6 $\pm$ 0.6	5.1 $\pm$ 0.6	0.1 $\pm$ 0.2	17.6 $\pm$ 1.8	8.6 $\pm$ 0.9	3.0 $\pm$ 0.3	2.5 $\pm$ 0.3
RU Lup	59801.00	C	330.0 $\pm$ 0.5	92.7 $\pm$ 9.3	48.5 $\pm$ 5.0	28.6 $\pm$ 2.9	5.7 $\pm$ 0.7	6.2 $\pm$ 0.7	-0.1 $\pm$ 0.2	22.5 $\pm$ 2.3	11.1 $\pm$ 1.1	3.4 $\pm$ 0.3	3.3 $\pm$ 0.3
RU Lup	59801.05	E	305.0 $\pm$ 1.5	82.0 $\pm$ 8.5	41.0 $\pm$ 5.0	21.1 $\pm$ 3.0	4.7 $\pm$ 1.0	6.0 $\pm$ 1.0	0.0 $\pm$ 0.6	21.1 $\pm$ 2.2	9.2 $\pm$ 1.0	3.1 $\pm$ 0.4	3.1 $\pm$ 0.4
RU Lup	59801.98	C	304.0 $\pm$ 0.5	73.9 $\pm$ 7.4	38.3 $\pm$ 4.0	21.1 $\pm$ 2.2	3.7 $\pm$ 0.5	4.5 $\pm$ 0.5	-0.1 $\pm$ 0.2	15.8 $\pm$ 1.6	8.8 $\pm$ 0.9	2.5 $\pm$ 0.3	2.7 $\pm$ 0.3
RU Lup	59802.07	E	287.0 $\pm$ 1.3	72.0 $\pm$ 7.5	36.3 $\pm$ 4.4	19.5 $\pm$ 2.7	3.0 $\pm$ 0.8	4.9 $\pm$ 0.9	0.1 $\pm$ 0.6	15.6 $\pm$ 1.6	7.6 $\pm$ 0.8	2.2 $\pm$ 0.3	2.5 $\pm$ 0.3
RU Lup	59802.97	C	250.0 $\pm$ 0.6	64.0 $\pm$ 6.5	31.6 $\pm$ 3.4	18.1 $\pm$ 2.0	4.0 $\pm$ 0.6	4.0 $\pm$ 0.6	0.1 $\pm$ 0.3	14.5 $\pm$ 1.5	6.7 $\pm$ 0.7	2.2 $\pm$ 0.2	1.8 $\pm$ 0.2
RU Lup	59804.00	C	244.0 $\pm$ 0.4	59.6 $\pm$ 6.0	30.4 $\pm$ 3.1	17.4 $\pm$ 1.8	2.7 $\pm$ 0.4	3.1 $\pm$ 0.4	0.1 $\pm$ 0.2	11.7 $\pm$ 1.2	5.3 $\pm$ 0.5	1.5 $\pm$ 0.2	1.6 $\pm$ 0.2
RU Lup	59804.10	E	236.0 $\pm$ 0.7	61.0 $\pm$ 6.2	31.4 $\pm$ 3.5	17.4 $\pm$ 2.1	2.5 $\pm$ 0.5	4.2 $\pm$ 0.6	0.1 $\pm$ 0.3	13.0 $\pm$ 1.3	5.8 $\pm$ 0.6	1.9 $\pm$ 0.2	1.8 $\pm$ 0.2

Table 10 continued

Table 10 (continued)

Object	MJD	Inst.	H $\alpha$	H $\beta$	H $\gamma$	H $\delta$	He I4387	He I4471	He I4713	He I5015	He I5875	He I6678	He I7065
RU Lup	59805.06	C	250.0 $\pm$ 0.4	72.6 $\pm$ 7.3	39.0 $\pm$ 4.0	23.6 $\pm$ 2.4	3.5 $\pm$ 0.4	4.6 $\pm$ 0.5	0.1 $\pm$ 0.2	15.3 $\pm$ 1.5	8.4 $\pm$ 0.8	2.5 $\pm$ 0.3	2.5 $\pm$ 0.3
RU Lup	59806.00	C	252.0 $\pm$ 0.5	53.3 $\pm$ 5.4	26.1 $\pm$ 2.8	15.1 $\pm$ 1.6	1.7 $\pm$ 0.4	2.5 $\pm$ 0.4	-0.2 $\pm$ 0.2	10.0 $\pm$ 1.0	5.5 $\pm$ 0.6	1.6 $\pm$ 0.2	1.7 $\pm$ 0.2
RU Lup	59807.00	C	189.0 $\pm$ 0.4	42.1 $\pm$ 4.2	21.9 $\pm$ 2.3	12.9 $\pm$ 1.3	1.0 $\pm$ 0.2	2.3 $\pm$ 0.3	0.1 $\pm$ 0.1	7.3 $\pm$ 0.7	4.4 $\pm$ 0.4	1.2 $\pm$ 0.1	1.3 $\pm$ 0.1
RU Lup	59807.10	E	184.0 $\pm$ 1.3	40.3 $\pm$ 4.5	20.4 $\pm$ 3.6	11.8 $\pm$ 2.6	1.1 $\pm$ 0.9	2.3 $\pm$ 0.8	0.0 $\pm$ 0.6	7.7 $\pm$ 0.9	4.5 $\pm$ 0.5	1.3 $\pm$ 0.3	1.6 $\pm$ 0.3
RU Lup	59808.05	C	168.0 $\pm$ 0.3	42.3 $\pm$ 4.2	21.8 $\pm$ 2.2	12.8 $\pm$ 1.3	0.8 $\pm$ 0.2	2.1 $\pm$ 0.3	0.1 $\pm$ 0.1	6.4 $\pm$ 0.6	3.9 $\pm$ 0.4	1.1 $\pm$ 0.1	1.1 $\pm$ 0.1
RU Lup	59809.07	C	166.0 $\pm$ 0.3	46.3 $\pm$ 4.7	24.5 $\pm$ 2.5	13.6 $\pm$ 1.4	0.9 $\pm$ 0.2	2.1 $\pm$ 0.3	0.0 $\pm$ 0.1	7.4 $\pm$ 0.7	4.4 $\pm$ 0.4	0.9 $\pm$ 0.1	1.2 $\pm$ 0.1
RU Lup	59810.03	C	147.0 $\pm$ 0.4	37.0 $\pm$ 3.7	19.6 $\pm$ 2.0	11.1 $\pm$ 1.2	0.5 $\pm$ 0.2	1.4 $\pm$ 0.2	0.1 $\pm$ 0.1	5.9 $\pm$ 0.6	2.8 $\pm$ 0.3	0.7 $\pm$ 0.1	0.8 $\pm$ 0.1
RU Lup	59811.05	C	224.0 $\pm$ 0.4	72.4 $\pm$ 7.3	37.4 $\pm$ 3.9	21.0 $\pm$ 2.2	5.4 $\pm$ 0.6	5.5 $\pm$ 0.6	0.1 $\pm$ 0.2	17.4 $\pm$ 1.7	7.5 $\pm$ 0.8	2.9 $\pm$ 0.3	2.2 $\pm$ 0.2
RU Lup	59812.02	C	222.0 $\pm$ 0.4	69.2 $\pm$ 6.9	32.0 $\pm$ 3.3	19.3 $\pm$ 2.0	4.9 $\pm$ 0.6	4.7 $\pm$ 0.5	0.2 $\pm$ 0.2	16.7 $\pm$ 1.7	7.5 $\pm$ 0.8	3.0 $\pm$ 0.3	2.3 $\pm$ 0.2
RU Lup	59813.05	C	287.0 $\pm$ 0.4	71.8 $\pm$ 7.2	34.9 $\pm$ 3.6	19.6 $\pm$ 2.0	2.0 $\pm$ 0.3	3.5 $\pm$ 0.4	0.0 $\pm$ 0.2	13.1 $\pm$ 1.3	5.7 $\pm$ 0.6	1.5 $\pm$ 0.2	1.7 $\pm$ 0.2
RU Lup	59814.00	C	194.0 $\pm$ 0.4	51.6 $\pm$ 5.2	26.4 $\pm$ 2.8	15.5 $\pm$ 1.6	1.1 $\pm$ 0.3	2.4 $\pm$ 0.3	0.0 $\pm$ 0.2	7.9 $\pm$ 0.8	4.5 $\pm$ 0.5	1.1 $\pm$ 0.1	1.2 $\pm$ 0.1
RU Lup	59814.04	E	199.0 $\pm$ 1.0	49.6 $\pm$ 5.1	25.6 $\pm$ 3.0	14.4 $\pm$ 1.9	1.2 $\pm$ 0.5	2.6 $\pm$ 0.5	0.0 $\pm$ 0.4	8.4 $\pm$ 0.9	4.7 $\pm$ 0.5	1.3 $\pm$ 0.2	1.5 $\pm$ 0.2
RU Lup	59815.05	C	268.0 $\pm$ 0.4	84.3 $\pm$ 8.4	42.3 $\pm$ 4.3	24.8 $\pm$ 2.5	4.8 $\pm$ 0.6	5.4 $\pm$ 0.6	-0.1 $\pm$ 0.2	19.9 $\pm$ 2.0	9.2 $\pm$ 0.9	2.9 $\pm$ 0.3	2.4 $\pm$ 0.3
RU Lup	59816.02	C	282.0 $\pm$ 0.4	93.4 $\pm$ 9.4	48.6 $\pm$ 5.0	29.0 $\pm$ 3.0	7.4 $\pm$ 0.8	7.3 $\pm$ 0.8	0.2 $\pm$ 0.2	23.2 $\pm$ 2.3	10.5 $\pm$ 1.1	3.4 $\pm$ 0.3	2.9 $\pm$ 0.3
RU Lup	59817.04	C	300.0 $\pm$ 0.4	93.1 $\pm$ 9.3	48.6 $\pm$ 4.9	28.8 $\pm$ 2.9	5.1 $\pm$ 0.6	5.9 $\pm$ 0.7	0.0 $\pm$ 0.2	20.8 $\pm$ 2.1	10.0 $\pm$ 1.0	2.9 $\pm$ 0.3	2.7 $\pm$ 0.3

NOTE—Fluxes are in units of  $10^{13}$  erg s $^{-1}$  cm $^{-2}$ . Additional 10% uncertainty due to continuum subtraction has been included in all uncertainties except H $\alpha$  and H $\beta$ . Instrument names are abbreviated as: C: CHIRON; E: ESPRESSO; X: XSHOOTER; S: SOPHIE; U: UVES; T: TCES



Table 11. Line luminosities for BP Tau

Object	MJD	Inst.	H $\alpha$	H $\beta$	H $\gamma$	H $\delta$	He I4387	He I4471	He I4713	He I5015	He I5875	He I6678	He I7065
BP Tau	59448.39	X	99.3 $\pm$ 0.8	14.4 $\pm$ 1.5	8.0 $\pm$ 0.8	4.9 $\pm$ 0.5	-0.2 $\pm$ 0.1	0.7 $\pm$ 0.1	0.2 $\pm$ 0.1	0.2 $\pm$ 0.1	0.8 $\pm$ 0.2	0.2 $\pm$ 0.1	0.2 $\pm$ 0.2
BP Tau	59452.35	X	71.3 $\pm$ 0.6	9.7 $\pm$ 1.0	5.5 $\pm$ 0.6	3.6 $\pm$ 0.4	-0.1 $\pm$ 0.1	0.6 $\pm$ 0.1	0.2 $\pm$ 0.1	0.2 $\pm$ 0.1	0.9 $\pm$ 0.1	0.2 $\pm$ 0.1	0.2 $\pm$ 0.1
BP Tau	59459.38	E	109.0 $\pm$ 0.5	16.3 $\pm$ 1.7	9.0 $\pm$ 1.3	5.8 $\pm$ 1.0	-0.0 $\pm$ 0.3	0.8 $\pm$ 0.3	0.2 $\pm$ 0.2	0.5 $\pm$ 0.2	1.4 $\pm$ 0.2	0.5 $\pm$ 0.1	0.5 $\pm$ 0.1
BP Tau	59460.37	X	82.4 $\pm$ 0.5	12.7 $\pm$ 1.3	7.0 $\pm$ 0.7	4.5 $\pm$ 0.5	-0.1 $\pm$ 0.1	0.7 $\pm$ 0.1	0.1 $\pm$ 0.1	0.3 $\pm$ 0.1	0.9 $\pm$ 0.1	0.3 $\pm$ 0.1	0.2 $\pm$ 0.1
BP Tau	59464.36	E	72.6 $\pm$ 0.9	9.5 $\pm$ 1.6	5.9 $\pm$ 2.7	3.8 $\pm$ 2.0	0.0 $\pm$ 0.8	0.6 $\pm$ 0.7	0.2 $\pm$ 0.4	0.0 $\pm$ 0.3	0.7 $\pm$ 0.2	0.2 $\pm$ 0.2	0.2 $\pm$ 0.2
BP Tau	59467.38	C	58.1 $\pm$ 0.3	15.0 $\pm$ 1.7	8.5 $\pm$ 1.4	2.7 $\pm$ 0.7	0.9 $\pm$ 0.3	0.4 $\pm$ 0.3	0.0 $\pm$ 0.2	0.3 $\pm$ 0.2	0.6 $\pm$ 0.1	0.2 $\pm$ 0.1	0.1 $\pm$ 0.1
BP Tau	59470.38	C	74.1 $\pm$ 0.3	13.1 $\pm$ 1.5	4.8 $\pm$ 1.0	2.1 $\pm$ 0.7	-0.2 $\pm$ 0.3	0.5 $\pm$ 0.2	-0.0 $\pm$ 0.2	0.2 $\pm$ 0.1	0.6 $\pm$ 0.1	0.2 $\pm$ 0.1	-0.1 $\pm$ 0.1
BP Tau	59845.35	C	83.2 $\pm$ 0.3	12.9 $\pm$ 1.3	5.5 $\pm$ 0.6	1.9 $\pm$ 0.3	-0.1 $\pm$ 0.1	0.5 $\pm$ 0.1	0.2 $\pm$ 0.1	0.2 $\pm$ 0.1	1.0 $\pm$ 0.1	0.3 $\pm$ 0.1	0.1 $\pm$ 0.1
BP Tau	59863.31	C	65.1 $\pm$ 0.2	7.3 $\pm$ 0.8	3.1 $\pm$ 0.4	1.0 $\pm$ 0.2	-0.2 $\pm$ 0.1	0.2 $\pm$ 0.1	0.1 $\pm$ 0.1	0.2 $\pm$ 0.1	0.5 $\pm$ 0.1	0.1 $\pm$ 0.0	0.0 $\pm$ 0.1
BP Tau	59868.29	C	62.1 $\pm$ 0.2	8.1 $\pm$ 0.9	3.1 $\pm$ 0.5	0.8 $\pm$ 0.2	-0.2 $\pm$ 0.1	0.2 $\pm$ 0.1	0.1 $\pm$ 0.1	0.1 $\pm$ 0.1	0.6 $\pm$ 0.1	0.1 $\pm$ 0.0	0.0 $\pm$ 0.1
BP Tau	59882.25	C	53.7 $\pm$ 0.2	8.0 $\pm$ 0.9	3.0 $\pm$ 0.5	1.0 $\pm$ 0.3	-0.2 $\pm$ 0.1	0.2 $\pm$ 0.1	0.0 $\pm$ 0.1	0.1 $\pm$ 0.1	0.6 $\pm$ 0.1	0.1 $\pm$ 0.0	0.0 $\pm$ 0.0
BP Tau	59893.21	C	28.6 $\pm$ 0.2	3.2 $\pm$ 0.5	1.4 $\pm$ 0.5	0.3 $\pm$ 0.3	-0.6 $\pm$ 0.2	0.1 $\pm$ 0.1	-0.1 $\pm$ 0.1	-0.2 $\pm$ 0.1	0.5 $\pm$ 0.1	0.1 $\pm$ 0.0	0.0 $\pm$ 0.0
BP Tau	59898.19	C	62.9 $\pm$ 0.3	9.6 $\pm$ 1.0	4.0 $\pm$ 0.5	1.2 $\pm$ 0.3	-0.0 $\pm$ 0.1	0.4 $\pm$ 0.1	0.1 $\pm$ 0.1	0.2 $\pm$ 0.1	0.8 $\pm$ 0.1	0.2 $\pm$ 0.0	0.0 $\pm$ 0.1
BP Tau	59907.19	C	66.6 $\pm$ 0.2	11.8 $\pm$ 1.2	3.6 $\pm$ 0.5	1.2 $\pm$ 0.3	-0.3 $\pm$ 0.1	0.7 $\pm$ 0.1	0.2 $\pm$ 0.1	0.3 $\pm$ 0.1	0.9 $\pm$ 0.1	0.2 $\pm$ 0.0	0.2 $\pm$ 0.1
BP Tau	59909.17	C	54.5 $\pm$ 0.2	9.2 $\pm$ 1.0	3.1 $\pm$ 0.5	1.3 $\pm$ 0.3	-0.3 $\pm$ 0.1	0.7 $\pm$ 0.1	0.2 $\pm$ 0.1	0.1 $\pm$ 0.1	0.8 $\pm$ 0.1	0.2 $\pm$ 0.0	0.1 $\pm$ 0.1
BP Tau	59910.17	C	67.5 $\pm$ 0.3	12.4 $\pm$ 1.3	4.9 $\pm$ 0.6	2.1 $\pm$ 0.3	-0.3 $\pm$ 0.1	0.8 $\pm$ 0.1	0.3 $\pm$ 0.1	0.4 $\pm$ 0.1	1.3 $\pm$ 0.1	0.4 $\pm$ 0.1	0.2 $\pm$ 0.1
BP Tau	59911.18	C	81.0 $\pm$ 0.2	13.9 $\pm$ 1.4	5.7 $\pm$ 0.6	2.3 $\pm$ 0.3	-0.4 $\pm$ 0.1	0.9 $\pm$ 0.1	0.3 $\pm$ 0.1	0.4 $\pm$ 0.1	1.2 $\pm$ 0.1	0.3 $\pm$ 0.0	0.2 $\pm$ 0.1
BP Tau	59912.15	C	65.1 $\pm$ 0.2	10.4 $\pm$ 1.1	4.4 $\pm$ 0.5	1.6 $\pm$ 0.2	-0.4 $\pm$ 0.1	0.8 $\pm$ 0.1	0.2 $\pm$ 0.1	0.2 $\pm$ 0.1	0.8 $\pm$ 0.1	0.1 $\pm$ 0.0	0.1 $\pm$ 0.1
BP Tau	59913.17	C	81.1 $\pm$ 0.3	13.3 $\pm$ 1.4	4.7 $\pm$ 0.6	1.9 $\pm$ 0.3	-0.4 $\pm$ 0.1	0.9 $\pm$ 0.1	0.3 $\pm$ 0.1	0.5 $\pm$ 0.1	1.2 $\pm$ 0.1	0.3 $\pm$ 0.1	0.2 $\pm$ 0.1
BP Tau	59914.18	C	72.7 $\pm$ 0.3	11.5 $\pm$ 1.2	3.9 $\pm$ 0.6	1.7 $\pm$ 0.3	-0.5 $\pm$ 0.1	1.0 $\pm$ 0.1	0.4 $\pm$ 0.1	0.2 $\pm$ 0.1	1.0 $\pm$ 0.1	0.1 $\pm$ 0.0	0.1 $\pm$ 0.1
BP Tau	59915.18	C	65.9 $\pm$ 0.3	10.5 $\pm$ 1.1	4.4 $\pm$ 0.6	1.2 $\pm$ 0.3	-0.1 $\pm$ 0.1	0.2 $\pm$ 0.1	0.0 $\pm$ 0.1	0.4 $\pm$ 0.1	0.8 $\pm$ 0.1	0.2 $\pm$ 0.1	0.1 $\pm$ 0.1
BP Tau	59916.19	C	55.2 $\pm$ 0.3	8.7 $\pm$ 0.9	3.2 $\pm$ 0.5	1.0 $\pm$ 0.3	-0.2 $\pm$ 0.1	0.1 $\pm$ 0.1	-0.0 $\pm$ 0.1	0.2 $\pm$ 0.1	0.6 $\pm$ 0.1	0.1 $\pm$ 0.0	0.0 $\pm$ 0.1
BP Tau	59917.16	C	65.0 $\pm$ 0.3	11.7 $\pm$ 1.2	4.6 $\pm$ 0.6	1.5 $\pm$ 0.3	-0.1 $\pm$ 0.1	0.3 $\pm$ 0.1	0.2 $\pm$ 0.1	0.2 $\pm$ 0.1	1.1 $\pm$ 0.1	0.2 $\pm$ 0.0	0.1 $\pm$ 0.1
BP Tau	59918.16	C	67.4 $\pm$ 0.3	11.5 $\pm$ 1.2	4.8 $\pm$ 0.6	1.8 $\pm$ 0.3	-0.1 $\pm$ 0.1	0.5 $\pm$ 0.1	0.2 $\pm$ 0.1	0.4 $\pm$ 0.1	1.0 $\pm$ 0.1	0.3 $\pm$ 0.1	0.1 $\pm$ 0.1
BP Tau	59919.15	C	77.8 $\pm$ 0.2	14.3 $\pm$ 1.5	5.2 $\pm$ 0.6	1.8 $\pm$ 0.3	-0.1 $\pm$ 0.1	0.6 $\pm$ 0.1	0.1 $\pm$ 0.1	0.7 $\pm$ 0.1	1.6 $\pm$ 0.2	0.4 $\pm$ 0.1	0.3 $\pm$ 0.1
BP Tau	59922.14	C	49.0 $\pm$ 0.3	7.8 $\pm$ 0.9	2.6 $\pm$ 0.8	1.8 $\pm$ 0.5	-0.9 $\pm$ 0.2	1.1 $\pm$ 0.2	0.5 $\pm$ 0.1	-0.1 $\pm$ 0.1	0.8 $\pm$ 0.1	0.0 $\pm$ 0.0	0.2 $\pm$ 0.1
BP Tau	59925.16	C	56.7 $\pm$ 0.3	9.3 $\pm$ 1.0	3.9 $\pm$ 0.7	2.0 $\pm$ 0.4	-0.8 $\pm$ 0.2	0.9 $\pm$ 0.2	0.4 $\pm$ 0.1	0.2 $\pm$ 0.1	0.7 $\pm$ 0.1	0.1 $\pm$ 0.1	0.1 $\pm$ 0.1
BP Tau	59926.14	C	71.8 $\pm$ 0.3	11.8 $\pm$ 1.2	4.8 $\pm$ 0.6	2.5 $\pm$ 0.4	-0.6 $\pm$ 0.1	0.8 $\pm$ 0.1	0.3 $\pm$ 0.1	0.2 $\pm$ 0.1	1.0 $\pm$ 0.1	0.3 $\pm$ 0.1	0.1 $\pm$ 0.1
BP Tau	59927.15	C	77.1 $\pm$ 0.3	14.9 $\pm$ 1.5	5.2 $\pm$ 0.6	2.6 $\pm$ 0.3	-0.4 $\pm$ 0.1	0.9 $\pm$ 0.1	0.3 $\pm$ 0.1	0.5 $\pm$ 0.1	1.4 $\pm$ 0.1	0.3 $\pm$ 0.1	0.3 $\pm$ 0.1
BP Tau	59928.11	E	60.4 $\pm$ 0.9	8.8 $\pm$ 1.8	5.4 $\pm$ 2.6	3.4 $\pm$ 2.0	-0.1 $\pm$ 0.8	0.5 $\pm$ 0.7	0.1 $\pm$ 0.5	0.3 $\pm$ 0.4	0.7 $\pm$ 0.2	0.2 $\pm$ 0.2	0.2 $\pm$ 0.2
BP Tau	59928.13	C	63.3 $\pm$ 0.3	9.3 $\pm$ 1.0	3.2 $\pm$ 0.5	1.3 $\pm$ 0.3	-0.5 $\pm$ 0.1	0.8 $\pm$ 0.2	0.4 $\pm$ 0.1	0.2 $\pm$ 0.1	0.7 $\pm$ 0.1	0.1 $\pm$ 0.0	0.1 $\pm$ 0.1
BP Tau	59929.14	C	50.0 $\pm$ 0.2	7.9 $\pm$ 0.9	3.7 $\pm$ 0.5	1.6 $\pm$ 0.3	-0.6 $\pm$ 0.1	0.7 $\pm$ 0.1	0.3 $\pm$ 0.1	0.0 $\pm$ 0.1	0.5 $\pm$ 0.1	0.0 $\pm$ 0.0	0.0 $\pm$ 0.1
BP Tau	59930.07	E	49.6 $\pm$ 0.5	7.3 $\pm$ 1.1	5.3 $\pm$ 1.3	3.3 $\pm$ 1.0	-0.2 $\pm$ 0.4	0.5 $\pm$ 0.3	0.1 $\pm$ 0.2	0.1 $\pm$ 0.2	0.4 $\pm$ 0.1	0.1 $\pm$ 0.1	0.1 $\pm$ 0.1
BP Tau	59930.13	C	53.2 $\pm$ 0.3	7.7 $\pm$ 0.9	3.2 $\pm$ 0.6	2.0 $\pm$ 0.4	-0.5 $\pm$ 0.2	1.0 $\pm$ 0.2	0.4 $\pm$ 0.1	-0.0 $\pm$ 0.1	0.6 $\pm$ 0.1	0.0 $\pm$ 0.0	0.1 $\pm$ 0.1
BP Tau	59931.13	C	65.9 $\pm$ 0.3	9.8 $\pm$ 1.1	3.7 $\pm$ 0.5	1.7 $\pm$ 0.3	-0.5 $\pm$ 0.1	0.6 $\pm$ 0.1	0.2 $\pm$ 0.1	0.1 $\pm$ 0.1	0.6 $\pm$ 0.1	0.0 $\pm$ 0.0	0.0 $\pm$ 0.1
BP Tau	59932.13	C	54.8 $\pm$ 0.3	8.3 $\pm$ 0.9	2.7 $\pm$ 0.5	1.0 $\pm$ 0.3	-0.3 $\pm$ 0.1	0.6 $\pm$ 0.1	0.2 $\pm$ 0.1	0.1 $\pm$ 0.1	0.5 $\pm$ 0.1	0.1 $\pm$ 0.0	0.1 $\pm$ 0.1
BP Tau	59933.13	C	63.6 $\pm$ 0.3	10.4 $\pm$ 1.1	3.2 $\pm$ 0.5	1.2 $\pm$ 0.3	0.0 $\pm$ 0.1	0.4 $\pm$ 0.1	0.1 $\pm$ 0.1	0.2 $\pm$ 0.1	0.8 $\pm$ 0.1	0.7 $\pm$ 0.1	0.0 $\pm$ 0.1
BP Tau	59933.17	E	59.7 $\pm$ 0.7	9.0 $\pm$ 1.4	5.8 $\pm$ 1.8	3.6 $\pm$ 1.4	-0.2 $\pm$ 0.5	0.4 $\pm$ 0.4	0.0 $\pm$ 0.3	0.2 $\pm$ 0.2	0.5 $\pm$ 0.2	0.1 $\pm$ 0.1	0.2 $\pm$ 0.1

Table 11 continued

Table 11 (continued)

Object	MJD	Inst.	H $\alpha$	H $\beta$	H $\gamma$	H $\delta$	He I4387	He I4471	He I4713	He I5015	He I5875	He I6678	He I7065
BP Tau	59934.07	E	57.7 $\pm$ 0.4	8.8 $\pm$ 1.1	6.2 $\pm$ 1.1	3.8 $\pm$ 0.8	-0.2 $\pm$ 0.3	0.5 $\pm$ 0.2	0.1 $\pm$ 0.2	0.1 $\pm$ 0.2	0.6 $\pm$ 0.1	0.2 $\pm$ 0.1	0.2 $\pm$ 0.1
BP Tau	59934.12	C	64.0 $\pm$ 0.3	10.9 $\pm$ 1.2	3.6 $\pm$ 0.5	1.4 $\pm$ 0.3	-0.4 $\pm$ 0.1	0.7 $\pm$ 0.1	0.1 $\pm$ 0.1	0.1 $\pm$ 0.1	0.8 $\pm$ 0.1	0.2 $\pm$ 0.0	0.1 $\pm$ 0.1
BP Tau	59935.11	C	63.8 $\pm$ 0.3	10.3 $\pm$ 1.1	3.3 $\pm$ 0.5	1.3 $\pm$ 0.3	-0.4 $\pm$ 0.1	0.7 $\pm$ 0.1	0.8 $\pm$ 0.1	0.1 $\pm$ 0.1	0.8 $\pm$ 0.1	0.0 $\pm$ 0.0	0.1 $\pm$ 0.1
BP Tau	59936.08	E	62.1 $\pm$ 0.6	9.4 $\pm$ 1.3	6.2 $\pm$ 1.5	3.9 $\pm$ 1.2	-0.1 $\pm$ 0.4	0.6 $\pm$ 0.4	0.1 $\pm$ 0.2	0.2 $\pm$ 0.2	0.7 $\pm$ 0.1	0.2 $\pm$ 0.1	0.2 $\pm$ 0.1
BP Tau	59936.11	C	68.3 $\pm$ 0.2	11.4 $\pm$ 1.2	4.2 $\pm$ 0.5	1.5 $\pm$ 0.3	-0.3 $\pm$ 0.1	0.7 $\pm$ 0.1	0.3 $\pm$ 0.1	0.2 $\pm$ 0.1	0.9 $\pm$ 0.1	0.2 $\pm$ 0.0	0.1 $\pm$ 0.0
BP Tau	59937.12	C	57.9 $\pm$ 0.2	10.8 $\pm$ 1.1	4.8 $\pm$ 0.6	1.9 $\pm$ 0.3	-0.2 $\pm$ 0.1	0.8 $\pm$ 0.1	0.1 $\pm$ 0.1	0.1 $\pm$ 0.1	0.9 $\pm$ 0.1	0.2 $\pm$ 0.0	0.1 $\pm$ 0.1
BP Tau	59938.12	C	52.7 $\pm$ 0.2	9.9 $\pm$ 1.1	3.7 $\pm$ 0.5	1.7 $\pm$ 0.3	-0.5 $\pm$ 0.1	0.7 $\pm$ 0.1	0.2 $\pm$ 0.1	0.2 $\pm$ 0.1	0.7 $\pm$ 0.1	0.2 $\pm$ 0.0	0.1 $\pm$ 0.1
BP Tau	59939.11	C	44.1 $\pm$ 0.3	7.3 $\pm$ 0.9	2.8 $\pm$ 0.6	1.6 $\pm$ 0.4	-0.4 $\pm$ 0.2	0.8 $\pm$ 0.2	0.3 $\pm$ 0.1	-0.0 $\pm$ 0.1	0.7 $\pm$ 0.1	0.3 $\pm$ 0.1	0.0 $\pm$ 0.1
BP Tau	59940.11	C	43.8 $\pm$ 0.2	7.5 $\pm$ 0.8	3.1 $\pm$ 0.4	1.2 $\pm$ 0.2	0.1 $\pm$ 0.1	0.1 $\pm$ 0.1	0.0 $\pm$ 0.1	0.1 $\pm$ 0.1	0.6 $\pm$ 0.1	0.2 $\pm$ 0.0	-0.0 $\pm$ 0.1
BP Tau	59941.13	C	41.1 $\pm$ 0.2	6.6 $\pm$ 0.7	3.2 $\pm$ 0.4	0.8 $\pm$ 0.2	-0.0 $\pm$ 0.1	0.3 $\pm$ 0.1	-0.0 $\pm$ 0.1	0.1 $\pm$ 0.1	0.5 $\pm$ 0.1	0.1 $\pm$ 0.0	-0.0 $\pm$ 0.1
BP Tau	59949.08	C	56.7 $\pm$ 0.2	9.0 $\pm$ 1.0	3.8 $\pm$ 0.5	1.4 $\pm$ 0.3	-0.2 $\pm$ 0.1	0.3 $\pm$ 0.1	0.1 $\pm$ 0.1	0.2 $\pm$ 0.1	0.5 $\pm$ 0.1	0.1 $\pm$ 0.0	0.0 $\pm$ 0.1
BP Tau	59950.08	C	70.5 $\pm$ 0.3	11.7 $\pm$ 1.2	4.7 $\pm$ 0.6	1.8 $\pm$ 0.3	-0.2 $\pm$ 0.1	0.3 $\pm$ 0.1	-0.0 $\pm$ 0.1	0.6 $\pm$ 0.1	1.1 $\pm$ 0.1	0.3 $\pm$ 0.1	0.1 $\pm$ 0.1
BP Tau	59951.08	C	57.1 $\pm$ 0.2	10.7 $\pm$ 1.1	5.0 $\pm$ 0.6	1.9 $\pm$ 0.3	-0.0 $\pm$ 0.1	0.4 $\pm$ 0.1	0.0 $\pm$ 0.1	0.2 $\pm$ 0.1	0.9 $\pm$ 0.1	0.3 $\pm$ 0.0	0.1 $\pm$ 0.1
BP Tau	59952.08	C	55.3 $\pm$ 0.2	11.1 $\pm$ 1.2	5.2 $\pm$ 0.7	2.1 $\pm$ 0.3	-0.1 $\pm$ 0.1	0.4 $\pm$ 0.1	-0.0 $\pm$ 0.1	0.3 $\pm$ 0.1	1.0 $\pm$ 0.1	0.2 $\pm$ 0.0	0.1 $\pm$ 0.1
BP Tau	59953.07	C	72.1 $\pm$ 0.2	14.5 $\pm$ 1.5	5.8 $\pm$ 0.7	2.1 $\pm$ 0.3	-0.1 $\pm$ 0.1	0.5 $\pm$ 0.1	0.1 $\pm$ 0.1	0.6 $\pm$ 0.1	1.0 $\pm$ 0.1	0.3 $\pm$ 0.0	0.2 $\pm$ 0.1

NOTE—Fluxes are in units of  $10^{13}$  erg s $^{-1}$  cm $^{-2}$ . Additional 10% uncertainty due to continuum subtraction has been included in all uncertainties except H $\alpha$  and H $\beta$ . Instrument names are abbreviated as: C: CHIRON; E: ESPRESSO; X: XSHOOTER; S: SOPHIE; U: UVES; T: TCES

Table 12. Line luminosities for GM Aur

Object	MJD	Inst.	H $\alpha$	H $\beta$	H $\gamma$	H $\delta$	He I4387	He I4471	He I4713	He I5015	He I5875	He I6678	He I7065
GM Aur	59498.99	S	72.4±0.3	4.8±0.6	3.2±0.7	1.0±0.6	-0.1±0.2	0.1±0.2	-0.1±0.1	0.1±0.1	0.9±0.1	0.1±0.0	-
GM Aur	59499.98	S	70.5±0.4	3.8±0.6	2.8±0.8	1.3±0.7	-0.4±0.2	0.3±0.2	0.0±0.2	-0.1±0.1	0.8±0.1	0.1±0.1	-
GM Aur	59501.13	S	71.7±0.4	5.4±0.8	4.3±0.8	2.4±0.7	-0.3±0.2	0.4±0.2	-0.0±0.2	0.0±0.1	1.0±0.1	0.1±0.1	-
GM Aur	59502.03	S	61.4±0.2	4.0±0.5	3.5±0.5	2.1±0.4	-0.4±0.1	0.3±0.1	-0.0±0.1	-0.1±0.1	0.7±0.1	0.0±0.0	-
GM Aur	59502.96	T	52.2±0.6	3.5±1.0	-	-	-	-	-0.1±0.3	-0.1±0.2	0.2±0.1	-0.0±0.1	-0.0±0.1
GM Aur	59503.11	S	64.3±0.3	4.8±0.6	3.9±0.6	2.0±0.5	-0.4±0.2	0.2±0.1	-0.0±0.1	-0.1±0.1	0.5±0.1	-0.0±0.0	-
GM Aur	59504.08	S	69.6±0.2	5.1±0.6	3.9±0.5	2.2±0.4	-0.4±0.1	0.2±0.1	-0.0±0.1	-0.1±0.1	0.6±0.1	-0.0±0.0	-
GM Aur	59504.34	X	77.4±0.7	5.9±0.7	3.4±0.5	1.6±0.2	-0.3±0.1	0.3±0.1	0.0±0.1	-0.1±0.1	0.5±0.1	-0.0±0.1	0.1±0.1
GM Aur	59505.02	S	67.5±0.2	5.1±0.6	3.8±0.6	2.0±0.4	-0.4±0.1	0.3±0.1	-0.0±0.1	-0.1±0.1	0.8±0.1	0.0±0.0	-
GM Aur	59505.11	T	59.4±0.5	5.2±1.1	-	-	-	-	-0.1±0.3	-0.2±0.2	0.1±0.1	0.0±0.1	0.0±0.1
GM Aur	59505.96	S	74.6±0.3	4.6±0.6	2.6±0.5	0.6±0.4	-0.2±0.1	0.1±0.1	-0.1±0.1	0.0±0.1	0.8±0.1	0.1±0.0	-
GM Aur	59507.09	T	38.3±0.8	1.8±1.4	-	-	-	-	-0.1±0.4	-0.1±0.3	0.3±0.2	0.1±0.1	0.0±0.2
GM Aur	59509.23	E	111.0±0.6	13.0±1.5	7.1±1.4	4.0±1.1	-0.3±0.4	0.8±0.3	0.0±0.2	0.1±0.2	0.7±0.1	0.1±0.1	0.4±0.1
GM Aur	59510.04	S	94.6±0.3	9.5±1.0	6.7±0.8	4.2±0.6	-0.4±0.1	0.5±0.1	-0.0±0.1	0.0±0.1	1.0±0.1	0.1±0.0	-
GM Aur	59510.09	T	78.0±0.6	7.8±1.2	-	-	-	-	-0.0±0.3	0.0±0.2	0.4±0.1	0.1±0.1	0.1±0.1
GM Aur	59510.14	T	80.4±0.6	8.2±1.3	-	-	-	-	-0.0±0.3	0.0±0.2	0.5±0.1	0.1±0.1	0.0±0.1
GM Aur	59511.97	T	47.5±0.6	1.7±1.1	-	-	-	-	-0.1±0.3	-0.1±0.2	0.1±0.1	-0.1±0.1	0.0±0.1
GM Aur	59511.99	S	47.0±0.3	1.5±0.4	1.4±0.4	0.3±0.4	-0.5±0.1	0.0±0.1	-0.1±0.1	-0.2±0.1	0.5±0.1	-0.0±0.0	-
GM Aur	59512.01	T	46.5±0.5	1.9±0.9	-	-	-	-	-0.1±0.2	-0.1±0.2	0.1±0.1	-0.0±0.1	-0.0±0.1
GM Aur	59513.03	T	54.5±0.6	4.4±1.1	-	-	-	-	-0.1±0.3	0.0±0.2	0.4±0.1	0.0±0.1	0.1±0.1
GM Aur	59513.08	T	46.7±0.7	3.1±1.3	-	-	-	-	-0.2±0.3	-0.1±0.3	0.2±0.1	0.0±0.1	0.1±0.1
GM Aur	59513.10	S	64.9±0.3	5.5±0.7	4.2±0.7	2.4±0.6	-0.4±0.2	0.3±0.2	-0.0±0.1	-0.0±0.1	1.0±0.1	0.1±0.0	-
GM Aur	59514.07	S	64.8±0.3	5.5±0.6	4.2±0.6	2.6±0.4	-0.3±0.1	0.4±0.1	0.1±0.1	-0.0±0.1	0.9±0.1	0.1±0.0	-
GM Aur	59515.04	T	56.8±0.4	4.9±0.9	-	-	-	-	-0.0±0.2	-0.1±0.2	0.3±0.1	0.0±0.1	0.0±0.1
GM Aur	59515.08	T	55.5±0.4	5.0±0.9	-	-	-	-	-0.0±0.2	-0.1±0.2	0.3±0.1	0.0±0.1	0.1±0.1
GM Aur	59515.09	S	58.4±0.4	4.5±0.6	4.0±0.7	2.1±0.6	-0.4±0.2	0.3±0.2	-0.0±0.1	-0.1±0.1	0.7±0.1	0.0±0.1	-
GM Aur	59516.01	S	60.1±0.3	5.1±0.7	4.2±0.7	2.3±0.6	-0.4±0.2	0.3±0.2	-0.0±0.1	-0.1±0.1	0.7±0.1	0.0±0.1	-
GM Aur	59553.13	E	57.6±0.5	3.9±0.8	2.6±1.6	1.3±1.1	-0.2±0.5	0.3±0.4	0.1±0.2	-0.2±0.2	0.1±0.1	-0.0±0.1	0.1±0.1
GM Aur	59554.17	E	56.2±0.8	4.2±1.4	3.3±2.5	1.8±1.7	0.6±0.8	0.3±0.7	0.1±0.4	-0.1±0.3	0.2±0.2	0.0±0.1	0.2±0.1
GM Aur	59555.19	E	59.8±0.4	6.4±0.8	4.2±1.1	2.2±0.9	-0.2±0.3	0.6±0.3	0.1±0.2	0.0±0.1	0.9±0.1	0.3±0.1	0.4±0.1
GM Aur	59556.15	X	65.6±0.4	7.6±0.8	4.8±0.5	2.9±0.3	-0.2±0.1	0.5±0.1	0.1±0.1	0.0±0.1	1.0±0.1	0.2±0.1	0.2±0.1
GM Aur	59556.19	E	66.3±0.5	7.1±1.1	4.9±1.8	2.9±1.4	-0.2±0.5	0.5±0.4	0.1±0.3	0.0±0.2	0.7±0.1	0.2±0.1	0.3±0.1
GM Aur	59558.86	T	50.7±0.5	4.8±1.1	-	-	-	-	-0.0±0.3	-0.1±0.2	0.4±0.1	0.1±0.1	0.1±0.1
GM Aur	59558.90	T	48.3±0.6	4.5±1.1	-	-	-	-	-0.1±0.3	-0.0±0.2	0.3±0.1	0.0±0.1	0.0±0.1
GM Aur	59559.91	T	36.4±0.5	2.4±0.9	-	-	-	-	-0.1±0.2	-0.1±0.2	0.2±0.1	0.0±0.1	0.0±0.1
GM Aur	59559.95	T	35.9±0.5	2.5±1.0	-	-	-	-	-0.1±0.2	-0.1±0.2	0.2±0.1	0.0±0.1	0.0±0.1
GM Aur	59910.17	E	71.6±0.5	7.6±1.0	4.7±1.1	2.3±0.8	-0.4±0.3	0.4±0.3	0.0±0.2	-0.1±0.2	0.5±0.1	0.1±0.1	0.2±0.1
GM Aur	59910.21	C	75.5±0.2	8.3±0.9	2.9±0.4	1.0±0.2	-0.5±0.1	0.6±0.1	0.1±0.1	-0.2±0.1	0.6±0.1	0.1±0.0	0.1±0.0

Table 12 continued

Table 12 (continued)

Object	MJD	Inst.	H $\alpha$	H $\beta$	H $\gamma$	H $\delta$	He I4387	He I4471	He I4713	He I5015	He I5875	He I6678	He I7065
GM Aur 59911.19		C	67.1 $\pm$ 0.2	5.5 $\pm$ 0.7	2.0 $\pm$ 0.4	0.6 $\pm$ 0.2	-0.5 $\pm$ 0.1	0.5 $\pm$ 0.1	0.2 $\pm$ 0.1	-0.2 $\pm$ 0.1	0.4 $\pm$ 0.1	-0.0 $\pm$ 0.0	0.1 $\pm$ 0.0
GM Aur 59912.20		C	71.1 $\pm$ 0.2	7.1 $\pm$ 0.8	2.6 $\pm$ 0.4	0.8 $\pm$ 0.2	-0.5 $\pm$ 0.1	0.4 $\pm$ 0.1	0.1 $\pm$ 0.1	-0.2 $\pm$ 0.1	0.5 $\pm$ 0.1	-0.1 $\pm$ 0.0	0.1 $\pm$ 0.0
GM Aur 59913.18		C	93.9 $\pm$ 0.3	9.2 $\pm$ 1.0	2.4 $\pm$ 0.5	0.5 $\pm$ 0.3	-0.5 $\pm$ 0.1	0.7 $\pm$ 0.1	0.3 $\pm$ 0.1	-0.2 $\pm$ 0.1	0.7 $\pm$ 0.1	0.0 $\pm$ 0.0	0.1 $\pm$ 0.1
GM Aur 59914.19		C	77.2 $\pm$ 0.2	7.1 $\pm$ 0.8	0.8 $\pm$ 0.4	0.3 $\pm$ 0.3	-0.4 $\pm$ 0.1	0.5 $\pm$ 0.1	0.3 $\pm$ 0.1	-0.1 $\pm$ 0.1	0.7 $\pm$ 0.1	-0.1 $\pm$ 0.0	0.1 $\pm$ 0.0
GM Aur 59915.13		E	68.3 $\pm$ 1.2	6.9 $\pm$ 2.3	4.4 $\pm$ 3.0	2.5 $\pm$ 2.1	-0.3 $\pm$ 0.9	0.4 $\pm$ 0.9	0.1 $\pm$ 0.6	-0.1 $\pm$ 0.5	0.5 $\pm$ 0.3	0.0 $\pm$ 0.2	0.2 $\pm$ 0.2
GM Aur 59915.20		C	69.9 $\pm$ 0.3	7.5 $\pm$ 0.9	2.0 $\pm$ 0.5	0.6 $\pm$ 0.3	1.0 $\pm$ 0.2	0.0 $\pm$ 0.1	-0.1 $\pm$ 0.1	-0.2 $\pm$ 0.1	0.7 $\pm$ 0.1	0.2 $\pm$ 0.0	0.1 $\pm$ 0.0
GM Aur 59916.16		E	65.2 $\pm$ 0.9	7.3 $\pm$ 1.8	4.7 $\pm$ 2.4	2.4 $\pm$ 1.6	-0.3 $\pm$ 0.7	0.4 $\pm$ 0.6	0.1 $\pm$ 0.5	-0.1 $\pm$ 0.4	0.5 $\pm$ 0.2	-0.0 $\pm$ 0.2	0.2 $\pm$ 0.2
GM Aur 59916.21		C	70.3 $\pm$ 0.3	8.0 $\pm$ 0.9	3.0 $\pm$ 0.5	0.3 $\pm$ 0.2	-0.2 $\pm$ 0.1	0.1 $\pm$ 0.1	-0.0 $\pm$ 0.1	-0.1 $\pm$ 0.1	0.7 $\pm$ 0.1	0.0 $\pm$ 0.0	0.1 $\pm$ 0.1
GM Aur 59917.19		C	76.1 $\pm$ 0.2	8.8 $\pm$ 1.0	3.3 $\pm$ 0.5	0.8 $\pm$ 0.3	-0.3 $\pm$ 0.1	0.1 $\pm$ 0.1	-0.0 $\pm$ 0.1	-0.1 $\pm$ 0.1	0.7 $\pm$ 0.1	-0.0 $\pm$ 0.0	0.1 $\pm$ 0.1
GM Aur 59918.19		C	70.8 $\pm$ 0.2	7.4 $\pm$ 0.8	2.9 $\pm$ 0.5	0.7 $\pm$ 0.3	-0.2 $\pm$ 0.1	0.0 $\pm$ 0.1	-0.1 $\pm$ 0.1	-0.1 $\pm$ 0.1	0.7 $\pm$ 0.1	0.0 $\pm$ 0.0	0.1 $\pm$ 0.0
GM Aur 59919.18		C	69.8 $\pm$ 0.2	6.9 $\pm$ 0.8	2.2 $\pm$ 0.4	0.4 $\pm$ 0.2	-0.2 $\pm$ 0.1	0.2 $\pm$ 0.1	-0.0 $\pm$ 0.1	-0.1 $\pm$ 0.1	0.6 $\pm$ 0.1	0.1 $\pm$ 0.0	0.1 $\pm$ 0.0
GM Aur 59920.18		C	52.9 $\pm$ 0.2	5.2 $\pm$ 0.6	1.5 $\pm$ 0.4	0.4 $\pm$ 0.3	-0.4 $\pm$ 0.1	0.2 $\pm$ 0.1	-0.1 $\pm$ 0.1	-0.2 $\pm$ 0.1	0.5 $\pm$ 0.1	0.0 $\pm$ 0.0	0.1 $\pm$ 0.0
GM Aur 59922.18		C	41.3 $\pm$ 0.3	3.8 $\pm$ 0.6	0.0 $\pm$ 0.7	0.5 $\pm$ 0.5	-1.4 $\pm$ 0.3	0.7 $\pm$ 0.2	0.2 $\pm$ 0.1	-0.7 $\pm$ 0.1	0.4 $\pm$ 0.1	-0.2 $\pm$ 0.0	0.1 $\pm$ 0.0
GM Aur 59925.18		C	65.9 $\pm$ 0.3	6.4 $\pm$ 0.8	2.5 $\pm$ 0.5	0.6 $\pm$ 0.3	-0.7 $\pm$ 0.1	1.0 $\pm$ 0.2	0.3 $\pm$ 0.1	-0.2 $\pm$ 0.1	0.7 $\pm$ 0.1	0.1 $\pm$ 0.0	0.1 $\pm$ 0.1
GM Aur 59926.17		C	75.6 $\pm$ 0.3	7.0 $\pm$ 0.8	2.2 $\pm$ 0.6	0.7 $\pm$ 0.4	-0.5 $\pm$ 0.2	0.8 $\pm$ 0.2	0.2 $\pm$ 0.1	-0.2 $\pm$ 0.1	0.8 $\pm$ 0.1	0.1 $\pm$ 0.0	0.2 $\pm$ 0.1
GM Aur 59927.18		C	65.4 $\pm$ 0.2	5.5 $\pm$ 0.7	1.8 $\pm$ 0.4	0.4 $\pm$ 0.2	-0.5 $\pm$ 0.1	0.7 $\pm$ 0.1	0.1 $\pm$ 0.1	-0.2 $\pm$ 0.1	0.9 $\pm$ 0.1	0.0 $\pm$ 0.0	0.2 $\pm$ 0.1
GM Aur 59928.15		C	73.2 $\pm$ 0.3	6.3 $\pm$ 0.7	1.6 $\pm$ 0.5	0.2 $\pm$ 0.3	-0.5 $\pm$ 0.1	0.6 $\pm$ 0.2	0.4 $\pm$ 0.1	-0.3 $\pm$ 0.1	0.7 $\pm$ 0.1	0.1 $\pm$ 0.0	0.2 $\pm$ 0.1
GM Aur 59929.16		C	93.4 $\pm$ 0.3	10.1 $\pm$ 1.1	3.8 $\pm$ 0.5	1.2 $\pm$ 0.3	-0.6 $\pm$ 0.1	0.8 $\pm$ 0.1	0.3 $\pm$ 0.1	-0.1 $\pm$ 0.1	1.0 $\pm$ 0.1	0.1 $\pm$ 0.0	0.2 $\pm$ 0.1
GM Aur 59931.14		C	91.2 $\pm$ 0.3	9.6 $\pm$ 1.0	3.1 $\pm$ 0.5	1.5 $\pm$ 0.3	-0.6 $\pm$ 0.1	0.8 $\pm$ 0.2	0.3 $\pm$ 0.1	-0.1 $\pm$ 0.1	1.0 $\pm$ 0.1	0.1 $\pm$ 0.0	0.2 $\pm$ 0.1

NOTE—Fluxes are in units of  $10^{13}$  erg s $^{-1}$  cm $^{-2}$ . Additional 10% uncertainty due to continuum subtraction has been included in all uncertainties except H $\alpha$  and H $\beta$ . Instrument names are abbreviated as: C: CHIRON, E: ESPRESSO, X: XSHOOTER, S: SOPHIE, U: UVES, T: TCES







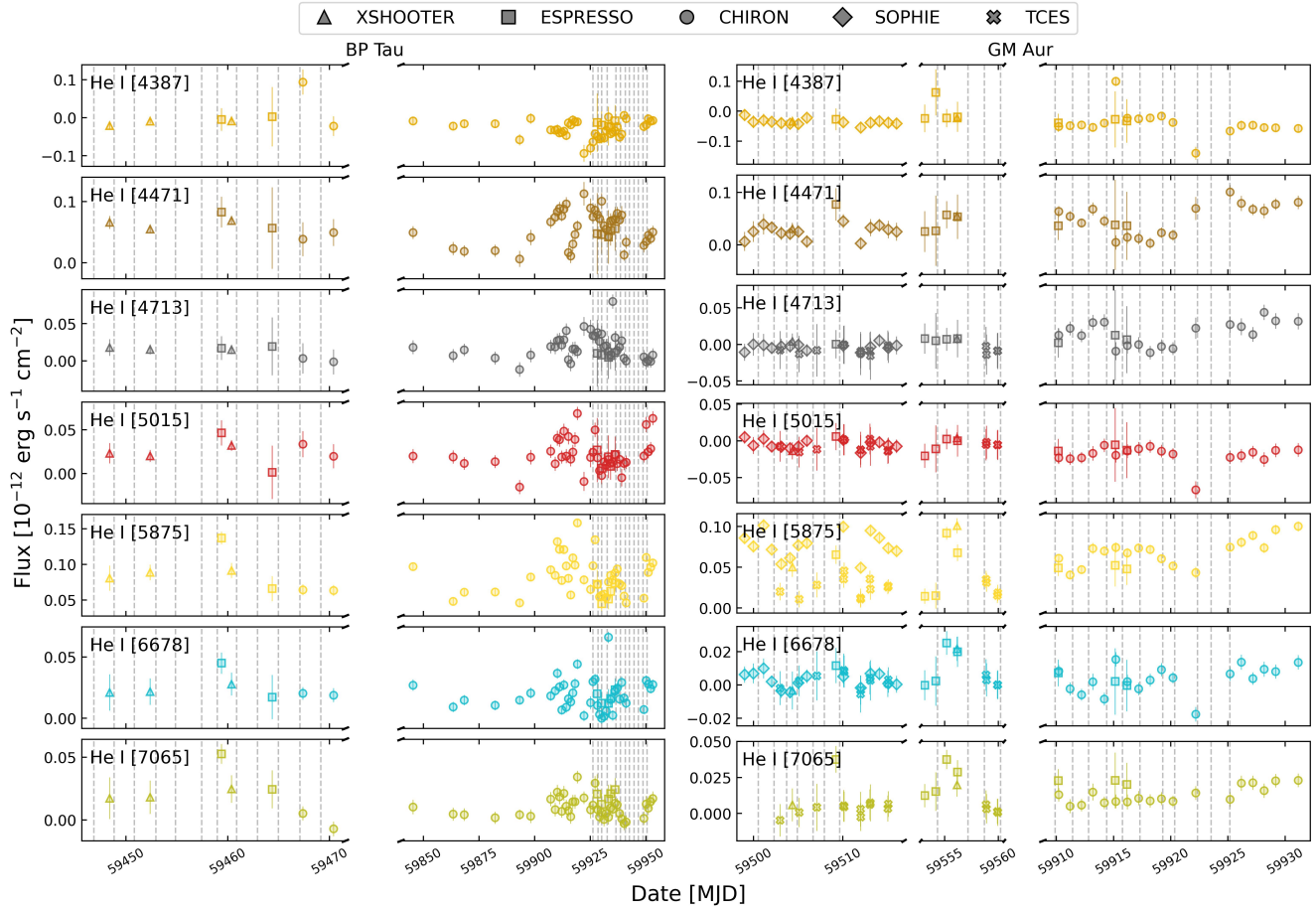


Figure 10. Same as Figure 9 but for BP Tau and GM Aur.